The Interactions of Small Molecules on Astrochemically Relevant Surfaces

A thesis submitted for the degree of Doctor of Philosophy

Catherine Higgins

Department of Chemistry

University College London

2020

I, Catherine Higgins, confirm that the work presented in this thesis is my own. Where information has been derived from other sources, I confirm that this has been indicated in the thesis.

Signed,

Abstract

The known Universe is composed of 99.9% hydrogen and helium. The remaining 0.1 % constitutes the abundance of the rest of the elements. Despite their low abundance relative to the lighter elements, the reactions of these heavier elements account for the complexity of species found in space. In particular, more than 200 complex organic species have been detected in the interstellar medium. They, along with carbonaceous and silicate dust grains, accumulate together in interstellar clouds. This thesis focusses on the reactions taking place within dense interstellar dust clouds, where the inner core is shielded from radiation emitted by nearby stellar objects by a dense, opaque outer layer of gas and dust. Within the cores of these dense clouds, molecular lifetimes are extended which allows for the formation of complex molecules through further reactions. The species observed within the interstellar medium can be formed *via* ion-neutral reactions in the gas-phase. However, for many molecules, the observed abundance cannot be accounted for by gas-phase chemistry alone. Therefore, reactions must also be occurring on the cold surfaces of the interstellar dust grains. This thesis will focus on the reactions taking place on these grains, presenting investigations into the interactions with, and reactions of, various species upon astrochemically relevant surfaces.

The investigation into the reaction of acrolein with atomic oxygen on a graphitic surface is discussed in Chapter 4. Multilayer doses of both species were co-dosed onto a graphite substrate held at temperatures ranging from 20 K to 140 K. A product with *m/z* 72 is observed for this reaction, suggesting the addition of oxygen across the double bond of the organic molecule: $C_3H_4O_2$. The kinetics of this reaction were modelled to gain a deeper understanding of the mechanisms occurring on the cold surface. Specifically, the contribution of the two prototypical surface mechanisms, Langmuir-Hinshelwood and Eley-Rideal mechanisms, was assessed at each surface temperature.

Additionally, the desorption characteristics of various astrochemically relevant molecules are outlined in Chapter 5. The behaviour of each species on a graphite surface was investigated and compared to the desorption characteristics previously investigated in the literature. The behaviour of the species observed in our desorption experiments is in good agreement with the behaviour observed in previous studies. The cohesion between our data and interactions observed previously, validates our experimental technique as a method to model the interactions of molecules under conditions similar to those in the ISM.

In Chapter 6 the desorption characteristics of molecular oxygen, acrolein and carbon dioxide from an amorphous carbonaceous surface are investigated. The amorphous surface is composed of porous, broken fullerene-like cage structures. Through analysis of the desorption spectra of the gases, it was found that each molecule had significantly larger binding energies to this amorphous surface than previously observed on graphite. This is consistent with previous studies into the desorption characteristics of various gases from the surface of single walled carbon nanotubes (SWCNTs) by Ulbricht *et al.* where the gas molecules showed enhanced binding to the SWCNTs compared to graphite surfaces. The implications of the discovery of these higher energy binding sites to astrochemistry is discussed.

Finally, in Chapter 7, results concerning the reaction of atomic oxygen with propene on a different amorphous carbonaceous surface are presented. The new surface is hydrogenated and consists of a large proportion of sp^3 hybridised carbon. Interestingly, the expected product, showing the addition of oxygen across the double bond of the propene was not observed for the reaction on this surface. On the other hand, a product with *m/z* 90 was detected, suggesting the addition of ozone across the double bond to form a product with the general formula $C_3H_6O_3$. The ozonolysis of an alkene is a well-known reaction in gas-phase chemistry but has not yet been observed under astrochemically relevant conditions. Additionally, in the gas phase, the $C_3H_6O_3$ product is known to undergo a rearrangement via the Criegee mechanism before breaking down into various oxygen-containing molecules, such as aldehydes, ketones, carboxylic acids and alcohols. If this mechanism can occur on the surfaces of interstellar dust grains it could help to account for the rich variety of complex organic molecules observed in the ISM.

Impact Statement

The aim of this research was to investigate the interactions of small molecules on astrochemically relevant surfaces. From these studies we gained information about the surface mechanisms taking place on a graphitic surface, the desorption characteristics of several molecules from an amorphous fullerene-like substrate and the reaction of propene with oxygen on an amorphous carbonaceous surface.

Through the modelling of the reaction of acrolein and atomic oxygen on a graphitic dust grain analogue under interstellar conditions, information about how the surface mechanisms proceed under different temperature conditions was obtained. This is important for the academic communities because it can provide more insight into how reactions occur in the interstellar medium under the same conditions. Incorporation of data about the surface mechanisms can provide more accurate modelling of the interstellar medium.

Desorption characteristics of small molecules from an amorphous carbonaceous surface were investigated. The dust grain analogue was composed of broken fullerene like structures and was more porous than the standard dust grain analogue (graphite). Analysis of the desorption profiles of the molecules from this surface revealed the presence of higher energy binding sites that are not observed on graphite. The higher energy sites result in longer residence times of molecules at higher temperatures than previously observed. This is also important for the academic community as it indicates that for dust grains with more amorphous structures, graphite might not be the best suited carbonaceous analogue (as desorption may occur at much higher temperatures than previously anticipated).

The insights described above and detailed in this thesis are extremely valuable to the academic community they provide a better understanding of the processes occurring in star forming regions of the interstellar medium. They can help to shed light on how the molecules that are detected might have formed under interstellar conditions and how they might go on to react upon the surfaces of the interstellar grains.

Acknowledgements

Firstly, I would like to express my deepest gratitude to my supervisor, Professor Stephen Price. Thank you for your expertise, your support and your patience, I really appreciate everything you have done for me.

I would also like to thank both past and present members of the Price group. Thank you all for being an amazing support group, I couldn't have done it without you. Special thanks to Dr Helen Kimber for teaching me the ropes, to Dr Felicity Gossan for always being there to lend a hand, to Dr Michael Parkes for always knowing what to do in a crisis and finally to Sam Armenta Butt and Dr Lily Ellis-Gibbings, who both encouraged me to come out of my basement sometimes.

I am also grateful to my family and friends, who have been cheering for me from the beginning. In particular, I want to thank my dad, Paul Higgins, and my mum, Claire Higgins as well as my sister, Naomi and my brother, Matthew.

A special thank you goes to my fiancé Damiano Cattaneo. It has been a bit of rollercoaster ride, so thanks for being there to hold my hand every time I cried over a graph.

And finally, thank you to the STFC for funding this research.

Dedication

This thesis is dedicated in loving memory of Dave Higgins.

I finally finished that book, Granda and there's not a dragon in sight.

I'm sorry you didn't get to see it, I miss you.

List of Publications

Listed below are expected future publications for the work presented in this thesis.

Addition of oxygen atoms to acrolein on surfaces at low temperatures

In preparation

Desorption characteristics of small astrochemically relevant molecules from Amorphous Carbonaceous Surfaces

In preparation

Ozonolysis of propene at low temperatures on an amorphous dust grain analogue

In preparation

List of Abbreviations

ACS	Amorphous Carbonaceous Surface
AGB	Asymptotic Giant Branch
BB	Big Bang
COM	Complex organic molecule
DMC	Dwarf Molecular Cloud
ER	Eley – Rideal
FESEM	Field Emission Scanning Electron Microscopy
FUV	Far UltraViolet
GMA	Giant Molecular Association
GMC	Giant Molecular Cloud
HACS	Hybrid Amorphous Carbonaceous Surface
HOPG	Highly Oriented Pyrolytic Graphite
HRTEM	High Resolution Transmission Electron Microscopy
HV	High Vacuum
IR	Infrared
ISM	Interstellar Medium
LH	Langmuir – Hinshelwood
ML	Monolayer
m/z	mass-to-charge ratio
PTFE	Polytetrafluoroethylene
QMS	Quadrupole Mass Spectrometry
SEM	Scanning Electron Microscopy
TOF	Time of Flight
TMP	Turbomolecular Pump
TPD	Temperature Programmed Desorption
TSP	Titanium Sublimation Pump
UHV	Ultra-High Vacuum

Table of Contents

Chapter 1. Introduction

1.1 Aim and Overview

The known matter in the Universe consists of approximately 99.9% hydrogen and helium.[1] The remaining 0.1% comprises the rest of the elements, termed "metals" by astronomers.[2] While the abundance of the heavier elements is low compared to that of hydrogen, rich and interesting chemistry involving these "metals" can still occur throughout the Universe. However, the matter in the Universe is not evenly distributed. There are regions where matter is dense (e.g. stars and planets) and regions where matter is diffuse (e.g. the space between the stars). The space between stars is referred to as the InterStellar Medium (ISM). The ISM is the star forming region and it contains clouds of dust and gas, called interstellar clouds.[1–4] The distribution of matter in the ISM is not uniform and so there are areas within the ISM that contain diffuse clouds and areas that contain dense clouds. The diffuse interstellar clouds have gas temperatures of approximately 100 K, dust grain temperatures of approximately 10 K and atomic number densities of 10^{7}-10^{9} species m^{-3}. Dense clouds are colder than the diffuse clouds, due to the extinction of the background UV radiation by the dust particles and gas, which shield the inner regions of the cloud. Typical atomic number densities of dense clouds range from 10^{9}-10^{10} species m^{-3} with gas and grain temperatures of approximately 10 K.[4–6]

This thesis will focus on the chemistry taking place in the cold dense interstellar clouds; in particular, the chemistry upon the cold surfaces of the dust grains. Specifically, the aim is to investigate the desorption of astrochemically relevant species (atoms or molecules found in the ISM) from laboratory dust grain analogues. Through these investigations, a better understanding of the gas-grain chemistry that takes place within the ISM can be achieved.

1.2 History of the Universe

The heliocentric model of our solar system, where the planets orbit around the sun, was published in the 15th century by Copernicus. The publication of the model completely changed our understanding of the cosmos and the solar system. Copernicus' work was of great interest to other well-known scientists who further questioned the conventional beliefs of the time, for example Kepler (who described planetary motion), Galileo (who introduced the theory of inertia) and Newton (who explained the concept of gravity) to name but a few.[7] However, it wasn't until the 20th century that astronomers started to question the structure of the wider universe. In 1929,

through his observations of the Doppler Effect in space, Edwin Hubble discovered that entire galaxies existed outside our own and he announced what he called the "red-shift distance law".[8] Hubble deduced that the galaxies were moving away from each other and that the furthest galaxies were moving away from us at a faster rate than the galaxies that were closer. Hubble's work enabled astronomers to conclude that the entire universe was expanding from a single point: a singularity. A singularity is a hypothetical point in space-time at which matter is infinitely compressed to an infinitesimal volume.[9] The Big Bang (BB) theory, which explains how our universe was born, begins with the explosion of such a singularity. The main stages of the universe after the BB are outlined below.

After the BB, in the early stages of the universe, the residual energy of the BB dissipated enough to allow the local environment to cool. The cooler conditions allowed for the generation of atomic nuclei from protons and neutrons meaning the early universe consisted of only ionised hydrogen and free electrons.[10] Nucleosynthesis of the protons and neutrons formed small atomic nuclei up to masses as large as lithium. The first molecular chemistry took place after this nucleosynthesis, and it was thought to have been catalysed by helium atoms as outlined below.[10]

$$He + H^+ \longrightarrow HeH^+ + h\nu$$

$$He + He^+ \longrightarrow He_2^+ + h\nu$$

The first hydrogen molecule was subsequently formed from reactions involving these helium and hydrogen atoms.

$$HeH^+ + H \longrightarrow H_2^+ + He$$

$$H_2^+ + H \longrightarrow H^+ + H_2$$

The background radiation from the BB was still intense during these early formation steps, so it is likely that the hydrogen molecules were short-lived.[10] Further reactions began to take place as the universe cooled, allowing stable molecular hydrogen to be formed, primarily through electron and proton catalysed reactions, as shown below. [10]

$$H + e^- \longrightarrow H^- + h\nu$$

$$H^- + H \longrightarrow H_2 + e^-$$

$$H + H^+ \longrightarrow H_2^+$$

$$H_2^+ + H \longrightarrow H_2 + H^+$$

As the density of the universe increased with the formation of these new molecules, the first star was formed when a dense region collapsed under its own gravity. At a critical density, nuclear fusion began to occur, and the star was formed. Heavier elements, as heavy as iron, were first generated from nucleosynthesis at the centre of such a star. Nucleosynthesis is an exothermic reaction and prevents the star from collapsing under its own gravitational field as will be discussed in detail later. The elements heavier than iron are generated *via* endothermic reactions when a star dies and so were formed much later, from stellar supernovae.[11,12] The supernovae explosions, caused by the gravitational collapse of the dying star, distributed the products of nucleosynthesis across the new universe. The explosions from multiple different stars of different sizes helped to increase the elemental variation in the universe, to what we observe today, allowing for the formation of a multitude of complex molecular species.

1.3 Clouds of Dust and Gas

1.3.1 Clouds

The universe today is still largely similar to the earlier version, since the composition of both is mostly hydrogen and helium.[1,2,10,13] The rich chemistry that we observe in the universe is as a result of approximately 0.1% of its matter. Molecular hydrogen is the most abundant gas-phase species, with CO (the next most abundant) having an abundance of 10^{-5} relative to H_2.[14] We aim to understand how the complex molecules that we observe are made from such a small fraction of atoms present. In particular, the objective of this work is to investigate the chemistry occurring within the dense clouds of gas and dust which make up the ISM.

a) b)

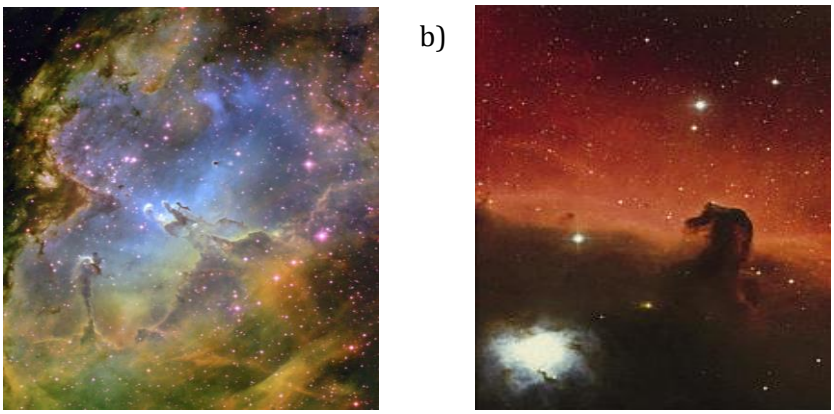

Figure 1.1: Images depicting diffuse and dense clouds. a) Diffuse clouds in the Eagle Nebula. b) Dense clouds in the Horsehead Nebula forming the shape of a horse's head. Images courtesy of NASA.

The two types of interstellar clouds, as mentioned above, are shown in Figure 1.1a and 1.1b.[15] Diffuse clouds (Figure 1a) are low density regions of gas and dust. These clouds are observed by studying the line absorption of light from background stars in the visible and ultra-violet regions of the spectrum.[3] The gas within these clouds is predominantly hydrogen.[2] The typical number densities of diffuse clouds are 10^{7}-10^{9} m^{-3}, meaning these clouds boast a somewhat limited chemistry, especially because most molecules are exposed to intense UV radiation from starlight.[2,16] Therefore, any complex molecules that may have formed are likely destroyed by photodissociation.

By comparison, dense clouds, such as those shown in Figure 1b, have much richer chemistry. These clouds have higher number densities than diffuse clouds; 10^{9}-10^{10} m^{-3}. This number density can be compared to the best ultra-high vacuum (UHV) found here on Earth. The use of such UHV techniques allows us to investigate the reactions that may take place within these interstellar regions. The inner regions of dense clouds are shielded from the intense radiation by the dust and molecules that make up the cloud.[2,3] The particulates act as shields by adsorbing or scattering the UV light.[1–4,17] Therefore, as opposed to diffuse clouds, the inner regions of dense clouds have temperatures of approximately 10 K. As a result of these low temperatures, new molecules have longer lifetimes and can go on to react further to produce the more complex molecules observed. As mentioned above, the generation of new molecules, and the subsequent increase in density, will cause the eventual collapse of these clouds under their own gravity leading to star formation. Dense clouds are often referred to as stellar nurseries because when they collapse a star can be born.[2,3,8,18] The observation of dense clouds is more difficult than that of diffuse clouds. Rotational spectroscopy in the microwave/submillimetre range can be used to investigate the gases present within the clouds but vibrational spectroscopy is necessary to study the dust particles. To avoid interference from the Earth's atmosphere, extra-terrestrial telescopes are required to study specifically the interstellar dust in the dense clouds, owing to the fact that vibrational spectroscopy is an infrared (IR) technique.[3,13]

1.3.2 Dust

Rich chemistry takes place within the ISM, in particular in the shielded regions of the dense clouds. However, although much gas-phase chemistry does take place, it alone cannot account for the observed molecular abundances.[1,3] To account for the observed molecular abundances, and depletions, we must conclude that gas-grain chemistry must also be occurring on the surface of the dust grains within the ISM. Astronomers are particularly interested in identifying the possible gas-grain interactions that may be taking place within the dense regions of the ISM. However, it was only in the 1960's that astronomers began to show an interest in how dust grains were

interacting with the gas, and the possible roles that these grains could have in complex molecule formation. Previously astronomers viewed the dust as an inconvenience, since it often masked other interesting astronomical features in the night sky.[13]

In 1784 William Herschel was the first astronomer to detect the presence of dust in the ISM.[5,13] While studying the Ophinchus nebula he noticed areas that were devoid of stars. He called these areas "ein Loch in Himmel" or " a hole in heaven".[18] In 1919, these dark regions were further studied by Barnard, who concluded that the apparent "holes" were in fact "obscuring bodies, nearer to us than the distant stars".[19] Modern astronomers have expanded upon this idea and we now know that these dark areas are dense interstellar clouds with high extinctions, where the light of background stars is blocked by the interstellar dust.[20] This identification was confirmed with the development of interstellar IR spectroscopy, as shown in Figure 1.2.[21] The interstellar dust causes Rayleigh scattering of the background starlight from the stellar objects behind the dust, making it appear as if there are areas where there are no stars. Infrared allows us to observe the background objects as IR radiation is not scattered as effectively by the dust grains.[22]

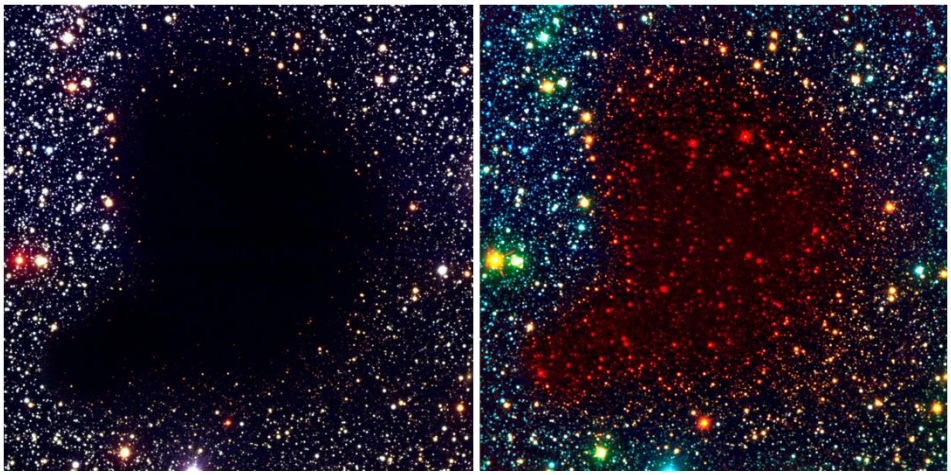

Figure 1.2: Image of Barnard 68, a "hole" in Ophiuchus of dense clouds of gas and dust taken under visible light (left) and using IR spectroscopy (right). This shows that the stars in the background are merely obscured by the dust.

Since Barnard's findings, there has been a multitude of evidence to prove the presence of dust grains in the interstellar medium. In 1930, while he was studying an open star cluster, Trumpler found that the distant stars were dimmer than expected and concluded that this was caused by "fine cosmic dust particles of various sizes" that were obscuring the starlight through selective absorption.[23] This process is now referred to as interstellar extinction, and we still examine the interaction of starlight with the dust particles today. In modern studies, stars are used as "standard candles" and we study the selective extinction of the starlight, or its reddening, as the selective absorption of the light causes us to perceive it as a different colour.[24] Interstellar extinction can be measured across a range of wavelengths, from UV to IR, and is often plotted as

a function of this wavelength, frequency or wave number, as shown in Figure 1.3, where the inverse wavelength of starlight is plotted against the extinction.[14] Figure 1.3 shows the typical shape of an extinction curve, with a broad bump at approximately 2175 Å or 4.6 μm^{-1}, which will be discussed later in this section.

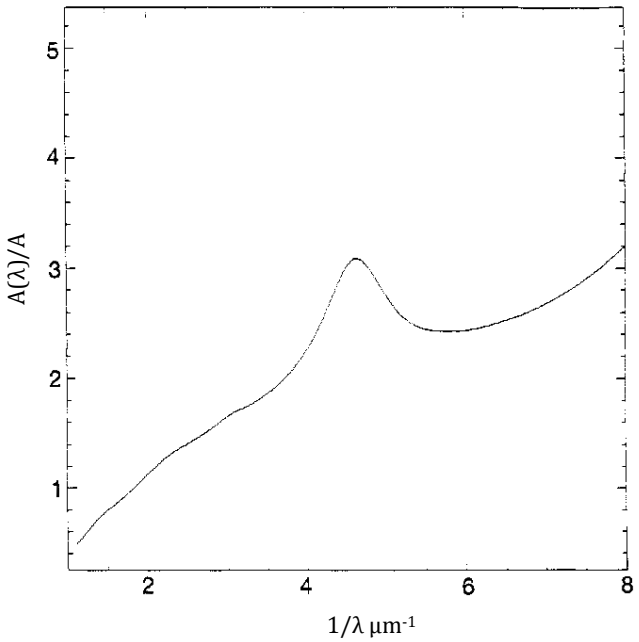

Figure 1.3: The typical shape of an average extinction curve, showing the extinction of starlight against the inverse of the wavelength of the light with a strong feature at 4.6 μm^{-1}.

Further evidence to support the presence of dust grains in the ISM arises from so-called "reflection nebulae". A reflection nebula occurs when the starlight of neighbouring stars is scattered by dust clouds. These nebula are often seen as "halos" such as is observed in the Pleiades (or Seven Sisters) star cluster, shown in Figure 1.4.[14,25]

Figure 1.4: Image of Pleiades star cluster. The reflection nebulae are visible as a blue haze or "halo" around the stars.

In 1949, Hiltner provided evidence for the polarization of starlight.[26] The light that travels from reflection nebulae is linearly polarised, allowing us to conclude that the dust particles are likely to be aligned and non-spherical, or anisotropic, in nature.[24,14]

Dust grains account for 1 % of the mass of interstellar clouds. They are observed *via* a variety of techniques such as extinction, reflection and emission measurements in order to study their properties.[1,2,13,15] This dust is composed of a mixture of amorphous carbonaceous material and amorphous silicates.[2,3,17] In fact, the 4.6 μm^{-1} feature observed in the extinction curve above (Figure 1.3), which is clearly quite intense, is associated with carbonaceous material, since graphite grains are expected to have a strong absorption feature at this wavenumber.[24,27] When studying oxygen-rich stars, there is also a broad infrared absorption feature at 9.7 μm which is associated with the Si-O stretching mode of silicates.[24] The 9.7 μm feature is not observed in studies of carbon-rich stars, which further suggests it is a silicate feature, as silicates are unlikely to form in the carbon-rich regions owing to insufficient oxygen as any O present is likely to react with carbon to form CO.[24] Additionally, in oxygen-rich regions there is also a broad absorption peak observed at 18μm which is assigned to the O-Si-O bend in silicates. Examination of these bands indicates that the silicates are likely amorphous, with the bands corresponding with the IR spectra of amorphous silicates made in the laboratory.[28]

Graphite and olivine are considered as acceptable laboratory analogues for these carbonaceous and siliceous interstellar grains. However, the dust grains can also include magnesium and iron as well as other silicates and carbon. In fact, the grains account for 100% of the magnesium and iron estimated to be present within the interstellar medium, as well as 30% of the oxygen and 70% of the carbon.[2] The grains themselves, are believed to be between 0.1 μm - 0.001 μm in size and elongated in shape with irregular surfaces.[2,3,13,18] These surfaces possess a large number of physisorption sites with a wide range of binding energies which can facilitate gas-grain interactions. When a gas is incident upon the surface of a dust grain it can be adsorbed onto the cold surface. Adsorbed species can then be brought together to react, meaning the dust grains act as a "reservoir" for gases.[2,29,30] Discrepancies (or depletions) between the observed gas-phase abundances of certain molecules and the abundances predicted in astronomical models can be explained if the grains can "store" gases on their surface after species "freeze-out" onto the cold surface.[20,31] In particular, there is a noticeable depletion of oxygen from the gas-phase in the interstellar medium. The observed depletion of oxygen has led astronomers to believe that oxygen containing species are adsorbed onto the surface of the cold grains of the dust in the ISM, allowing a number of surface reactions to proceed, as will be discussed later in this section.[1,31–34]

In the dense clouds, where the gas and grain temperatures are low, molecular ices can form on the surfaces of the grains.[1–4] Gaseous atoms and molecules readily condense onto the cold surfaces to form layers of ices but molecular ices are also formed by reactions on the surfaces of the dust grains.[35] The main component of interstellar ice is water, which accounts for between 60-70% of all ices.[36] In the dark clouds of the interstellar medium, extinction curves show an additional feature at 3.1 μm, which is believed to correspond to the O-H stretching frequency of water.[24] In addition, the 3.1 μm feature is not observed in diffuse clouds, which is what we would expect as the environment in diffuse clouds is not conducive to ice formation.[37] Other abundant molecular ices include carbon dioxide (CO_2), carbon monoxide (CO), methanol (CH_3OH), ammonia (NH_3), methane (CH_4) and formaldehyde (H_2CO).[2,3,38] Gases can also interact with the ice mantles on the surface of the grains.[18] As mentioned, the ices are made of small molecules and over the course of the lifetime of a cloud, the thickness of these icy layers can increase to a few hundred nanometres. The reaction of the incoming gas with the ice could lead to the formation of the more complex organic molecules observed in the ISM as will be discussed in detail below.

In order for us to fully understand the surface chemistry of the interstellar dust grains in the ISM, we must also understand the mechanisms through which the gases react on the surface. The two most accepted reaction pathways are known as the Langmuir-Hinselwood and Eley-Rideal mechanisms. The process described by the Langmuir-Hinselwood (LH) mechanism is a diffusive one. When a gas species is adsorbed onto the surface at a binding site, it is thermalized and can

then diffuse between the binding sites on the surface by overcoming a diffusive barrier, or *via* tunnelling, until it finds a reactive partner. When the adsorbates react together, one of two things can occur. Firstly, the molecule can desorb using the energy associated with its formation to overcome its binding energy in a process known as chemical desorption. Or secondly, the newly formed molecule can remain on the surface until the surface is irradiated in some way, after which the molecule will desorb (usually *via* thermal desorption or photodesorption). By contrast, the Eley-Rideal (ER) mechanism does not involve diffusion but instead describes a pathway in which the incoming gas species will "hit" an adsorbate directly causing a reaction.[1–3,13,17] Both the LH and ER processes are thought to occur to a certain degree on all the grain surfaces; the degree to which each process occurs varies with surface composition, shape, the gas-phase conditions and the gas that is involved. In understanding how a certain gas interacts with a certain surface under conditions that mimic conditions in the dense clouds, we can better understand how reactions with that same gas will occur on a similar surface in the ISM.

1.4 Life cycle of a star

As mentioned above, the interstellar medium can be divided into phases, differentiated by the density of the phase itself and the nature and intensity of the ambient radiation.[39] The diffuse and dense clouds described above are formed in regions of the ISM known as HI regions, where hydrogen is neutral and atomic. If the density of this neutral region is >1000 atoms per cm^3 then hydrogen exists as molecular hydrogen within molecular clouds.[39,40] The structures present with the HI regions, known as Giant Molecular Associations (GMAs), are gravitationally bound with masses as high as 10^7 solar masses ($M_\odot$), where 1 $M_\odot$ is equal to the mass of the Sun (2 x 10^{30} kg).[41] GMAs are subject to extreme turbulence from the diffuse ionised interstellar medium (HII regions).[39] The effect of turbulence and gravitational instabilities causes fragmentation within the GMAs, forming Giant Molecular Clouds (GMCs), with masses of approximately 10^4-10^6 $M_\odot$.[41,40] Giant molecular clouds are warm clouds (>10 K) that are largely located on the spiral arms of galaxies.[40] Molecular clouds with masses < 10^4 $M_\odot$ are known as Dwarf Molecular Clouds (DMCs), these are cold molecular clouds (<10 K) that are distributed throughout the galactic disk, which can account for the formation of stars in areas across the Milky Way.[40]

Within the dense clouds of the ISM are "cores"; the core is the densest part of the cloud, and it is the area that is completely shielded from Far Ultraviolet (FUV) rays from nearby stars.[41] As discussed above, the shielded region within these clouds are areas where interesting chemistry can take place owing to the increased longevity of molecules compared to diffuse regions or photodissociation regions (PDR).[41] Additionally, the dense cores are also the areas where star

formation takes place. In 1946, Bok was the first to suggest that these dark clouds were the main areas of star formation.[20] He referred specifically to areas known as Bok Globules, which are similar in nature to the dense cores within molecular clouds except they are less homogeneous than the cores and are not embedded within molecular clouds owing to exposure to external events.[20] In fact, it is now believed that Bok globules may be the sites of formation of low mass stars. As a result of the similarity between the two interstellar sites, this thesis will address what is happening in the dense cores prior to star formation and assume a similar process is happening within the Bok globules.

The dense cores within the molecular clouds are heated through the action of cosmic rays (as UV rays cannot penetrate the outer shell of protective gas and dust). The cosmic rays cause ionisation of the dust grains.[20] A cosmic ray is a ray that consists of high energy charged particles (MeV).[39] Upon impact between a ray and a dust grain, the grain loses an electron and this electron will thermally equilibrate with other electrons and molecules in the surrounding mediums, causing an increase in heat.[39] The dense cores are then cooled by line emission from the molecules within the core.[20] The core is gravitationally bound and would contract under its own gravity if not for a number of processes that counteract the inward pull of gravity. For example, the cooling emission of radiation creates a thermal pressure from the inner core towards the less dense outer regions of the cloud. Additionally, the magnetic field and the turbulence of the cores need to be taken into consideration. The magnetic field present within the ISM is widely considered a major factor for molecular cloud support because of the longevity of the field and the fact that it is not easily dissipated.[40]

Turbulence refers to the violent disturbance of matter and it is universally present within most of the molecular gas in galaxies, such as our own Milky Way.[41] As the ISM is subject to the mechanical effects generated from explosions of massive stars and violent stellar winds, turbulence is generated throughout.[39] Turbulence within the molecular clouds is supersonic which leads to a hierarchical distribution of densities from which we derive the diffuse and dense clouds.[20] This has been observed within the *p*Oph cloud, where a hierarchy of smaller and denser clouds are embedded in larger more diffuse ones.[42] The role of turbulence as a factor of gravitational support in molecular clouds is a greatly disputed topic. While the dust and gas in the ISM have supersonic motions, the gas and dust present within the cores are under a denser regime. [42]Therefore, there are only low levels of turbulence within the core and subsonic internal motions.[20] Many believe that the turbulence is only a minor contributor to the support of the core.

The dense core will continue to grow due to the continuous infall of material from the surrounding cloud.[39] At a certain critical mass, the gravitational force inward is greater than the

outward force causing the core to collapse on itself. The collapse of the core leads to the formation of a protostar, where the dense centre of condensed material is surrounded by a protostellar disk deeply imbedded within the infalling envelope of gas and dust.[40] Simultaneously, as the protostellar disk forms, bipolar jets also appear perpendicular to the disk. The velocity of the jets is several hundred km/s and they are composed of ionised gas. The jets disperse the remaining parent cloud away from the newly formed protostar.[39] Some matter from the parent cloud is carried away and can subsequently fall back onto the disk or the forming star. The protostar will continue to grow due to the infall of material so that the opacity of the core also increases, which hinders in the ability of the molecules present within the core to irradiate away the thermal energy. The core temperature, therefore, begins to increase as it is no longer being effectively cooled. If the mass of the core is >0.07 $M_{\odot}$, then nucleosynthesis can occur when the inner temperature is warm enough and a star is formed.[39] The fusion reactions within the core of the star generate a stellar wind that helps to disperse the remaining surrounding material into the surrounding cold disk. The solid material within these disks will eventually agglomerate together to form planets.[39] Planets that form, particularly far away from the newly formed star, will be able to capture some of the surrounding gas and form gas planets similar to the planets in the outer Solar System, e.g. Jupiter. For protostars that are too small, the temperature will not be sufficient for hydrogen fusion to occur but other nuclear fusion reactions can take place, which will lead to the formation of a brown dwarf.[39]

Nucleosynthesis refers to the nuclear fusion reactions that take place within a star. Nuclear fusion reactions are responsible for the large amounts of energy released from stellar objects. In 1938, von Weizsacker outlined the mechanism for the fusion of hydrogen into helium, the general equation for which is outlined below, where ν_e refers to an electron neutrino and e^+ is a positron:[39]

$$4\ {}^{1}H \rightarrow\ {}^{4}He + 2e^{+} + 2\nu_e + 24.7MeV$$

In stars similar in size to the Sun, the temperature of the stellar core is approximately 3 000 000 ˚C, whereas in more massive stars to temperature can be as high as 10 000 000˚C, resulting in the process of hydrogen fusion occurring at a much faster rate, leading to a shorter lifetime.[39] In brown dwarfs, the lower temperature only allows for the fusion of deuterium and lithium, preventing the cooling for the small mass object for a few million years. [39]

When the process of hydrogen fusion begins to occur within the core, the star is described as having entered the main sequence.[39] Stars can be classified differently depending upon their luminosity, size, colour and temperature. The Hertzprung-Russell diagram (Figure 1.5)[43] plots the absolute magnitude (or luminosity) of a star of known distance as a function of surface temperature and spectral class, where the spectral class refers to the spectral line emissions from the star that can be used to describe the metallicity of the star.[39]

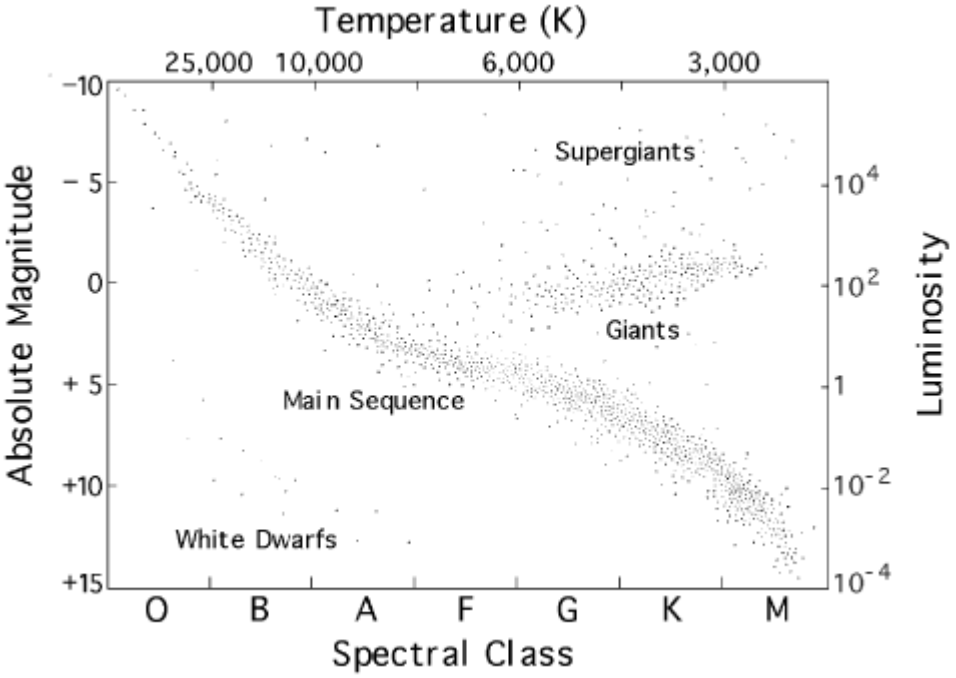

Figure 1.5: A Hertzsprung-Rusell diagram showing how stars can be classed based upon their absolute magnitude, their spectral class, their temperature or their luminosity. Our own Sun is classed as a G5 star so it lies in the main sequence. Image courtesy of NASA.

When a star has used all of its hydrogen, the core will increase in temperature and it will begin to burn helium.[39] The burning of helium into heavier elements, such as carbon, beryllium, and oxygen, is a more energetic process that causes the expansion of the star, leading to the progression of the star into a red giant.[39,44] Red giants are cooler than stars because the energy released from the fusion processes in the stars core is dissipated across a larger radius. For more massive stars (> 3 $M_{\odot}$), the expansion of the star into a red giant occurs on a much larger scale to form a red supergiant.[39] Red giants and red supergiants will continue to burn their fuel until no further nuclear fusion reactions can occur. Elements as heavy as iron can be formed through the nucleosynthetic processes taking place within the giant stellar objects.[12]

The manner through which the life of a star ends depends upon the size of the star. For a small star (< 1.4 $M_{\odot}$), when the fuel runs out, fusion stops and the remnants of the red giant contract. This forms a dense hot core, known as a white dwarf.[39,44] This core will eventually cool to form a

black dwarf. The rest of the matter not contained within its core is thrown off into a planetary nebula, where the matter will eventually incorporate itself into diffuse and dense interstellar clouds once more. When a star is more massive and has become a red supergiant, the same gravitational collapse occurs but again on a larger scale and very suddenly. During this process the outer layers of the star are drawn quickly into the core, then launched rapidly outwards from the centre in a shockwave known as a supernova.[11,12,39] During this process, the fusion of heavier elements will occur, and these heavier elements are then dissipated, along with a large amount of other matter, back into space. For the largest stars in the Universe, the gravitational collapse can lead to the formation of a black hole, which is a region in space where the gravitational pull is so strong that not even light is able to escape.[39,44]

This thesis focusses on the chemistry that takes place in the dense clouds/cores prior to the formation of a protostar. In these cold, dark regions the gases will freeze out onto the cold interstellar dust grains allowing a number of different chemical reactions to occur. As can be seen from the lifecycle of a star, the molecules that are made in the clouds can be distributed throughout the areas around a forming star. This realisation has led many scientists to believe that the molecules found on Earth that are necessary for the generation of life may have had interstellar origins. It is therefore vital that we understand the chemistry taking place within these regions.

1.5 Reactivity on the surface of dust grains

The formation and the reactivity of the most abundant species involved in the surface chemistry of the ISM have been studied in detail over recent years. Below I will outline the main studies into the formation of hydrogen, water and methanol as well as the reactivity of oxygen in the interstellar medium.

1.5.1 Hydrogen Formation

The 1930's saw the first detection of molecules in space. These early findings revealed the presence of several small molecules, in particular CH, CH^+ and CN, first found in the diffuse clouds of the interstellar medium. [45] Further research predicted the most abundant molecule in the ISM would be molecular hydrogen (H_2) which was subsequently detected in the 1970's by an extra-terrestrial telescope.[45] Since hydrogen is the most abundant molecule in the interstellar medium it is expected to play key roles in the formation of other molecules and so the formation of H_2 is of particular interest to astronomers. In the ISM atomic and molecular encounters are rare events, owing to the low densities and low temperature of the environment, meaning three-body reactions are unlikely to occur. The environmental conditions in the ISM are, therefore, not suitable for the most obvious hydrogen formation mechanism; direct association as shown in Equation 1.1, which occurs through a three-body process.[46,47]

$$H + H + M \rightarrow H_2 + M \qquad 1.1$$

Since direct atomic hydrogen association remains unlikely in the ISM, alternative reaction pathways for H_2 formation were considered. For example, Herzberg *et al.* (1955) proposed H_2 was formed through a series of exothermic reactions as shown in equation 1.2.[48] However the proposed mechanism had high activation energies and thus was deemed unlikely to occur in the cold clouds of the interstellar medium.

$$CH + H \rightarrow H_2 + C \qquad 1.2$$

Direct radiative capture as shown in equation 1.3 was also considered a possible H_2 formation reaction. However away from stars, the molecular ion H_2^+ does not readily form from H_2 because of the high ionization energy required for its formation. In addition, any H_2^+ ions that did form would likely undergo dissociative recombination to form atomic hydrogen, as shown below (1.4).[46]

$$H_2^+ + e^- \rightarrow H_2 + h\nu \qquad 1.3$$

$$H_2^+ + e^- \rightarrow 2H \qquad 1.4$$

In 1961, McDowell *et al.* proposed that H_2 formation occurred *via* associative detachment as shown in equation 1.5.[49] While H^- is a more likely ion than H^+ to be present within the ISM, owing to the multitude of free electrons that can bond to atomic hydrogen, the predicted abundance of H_2 formed was still orders of magnitude too small to account for the density observed in the ISM.

$$H^- + H \rightarrow H_2 + e^- \qquad 1.5$$

Van de Hulst (1948) was the first to propose that H_2 formation occurred *via* catalytic interactions with the surfaces of the dust grains.[50] This theory was further supported by Brackmann and Fite (1961), who investigated H_2 formation *via* the reaction of atomic H on a solid-state catalyst, in this case copper.[51] Brackmann and Fite concluded that H combination occurred readily on cold surfaces. Gould and Salpeter (1963) further investigated H_2 formation on the surfaces of dust grains.[46] Gould *et al.* concluded that surface temperatures in the ISM were cold (5-20 K) and calculated that the cold surface would allow hydrogen atoms to adsorb *via* weak Van der Waals bonds where the atoms could subsequently react together to form molecular hydrogen. Gould and Salpeter further calculated that the surface temperature itself would play a key role in H_2 formation, as too high a temperature would cause the H atoms to desorb before they could come together to react. In this work, Gould *et al.* also predicted that the reaction process would result in a release of energy that would allow the H_2 to desorb from the surface.

Interstellar abundances and distributions were also studied by Gould, Gold and Salpeter (1963), who stated that the H abundance in dense clouds was likely to be small as most H atoms would be tied up in molecular hydrogen, further confirming that H_2 formation likely occurred on the surface of dust grains.[52] Gould, Gold and Salpeter further calculated that there is a high H_2 abundance in dense clouds in the ISM because the major H_2 dissociation process is through photoionization. The majority of the radiation needed for this ionization process is blocked by the dust grains in the dense clouds meaning the H_2 molecules are shielded and unlikely to dissociate.[52]

It is important to note that, up until the 1980s, all studies investigating H_2 formation in space were either theoretical or the experiments were performed under conditions that did not really relate to the ISM.[45] However, experiments using ultrahigh vacuum enabled practical studies with more accurate conditions relating to the ISM to be performed. The first experiments to verify H_2 formation on the surface of dust grains were carried out at Syracuse University by Pironello *et al.* who used the temperature programmed desorption (TPD) technique to analyse the formation of molecular hydrogen on bare polycrystalline olivine.[45,47,53] The aim of the experiments by Pironello *et al.* was to measure the effect of surface temperature on the efficiency of the reactions under conditions similar to those in the ISM. Pironello *et al.* deduced that there was a weak interaction

between the surface and the hydrogen atoms and stated that a number of binding sites were available for atomic hydrogen to bind to. The different binding sites enabled H to diffuse across the surface until it reached another H to react with and form molecular hydrogen. The reaction mechanism proposed by Pironello *et al.* describes a Langmuir-Hinselwood relationship between the adsorbed species and the surface which was consistent with earlier studies by Hollenbach and Salpeter.[54] Earlier calculations also indicated that the Eley-Rideal mechanism may also play a role in the formation of H_2, in particular on surfaces with small cross-sections (typically of the order of $Å^2$).[45] Later experiments also indicated that the Eley-Rideal mechanism was a possible reaction pathway as seen in the experiments of Mennella *et al.* where hydrogen atoms were dosed on a previously hydrogenated amorphous sample.[45,55]

Katz *et al.* translated the results of Pironello *et al.* into a model more suited for the conditions of the ISM.[47,53,56] In particular, the experiments performed by Pironello *et al.* were modelled with a more appropriate flux of hydrogen atoms and under steady state conditions similar to the clouds of the ISM. Katz *et al.* found that there was a high efficiency of H_2 formation over a narrow surface temperature range.

Following the experiments described above, further studies were conducted on various other astrochemically relevant surfaces. Experiments on amorphous carbon found that there was a higher efficiency of molecular hydrogen formation on the carbon surface when compared with the polycrystalline olivine surfaces discussed above.[57] Vidali and Lemaire studied hydrogen formation on the surface of various silicates.[58–60]Together they confirmed that hydrogen atoms were weakly bound to the silicate surfaces, that various adsorption sites were available over an extended temperature range and that the Langmuir-Hinshelwood mechanism is responsible for hydrogen formation. He *et al.* studied the formation of H_2 and HD on a forsterite (Mg_2SiO_4) single crystal at 7 K as well as the adsorption and desorption of D_2.[61] Using this data He *et al.* employed rate equations to calculate the desorption energy of HD (24.5 meV) and of D_2 (27 meV). The formation of D_2 was also studied on an amorphous silicate thin film over a wide temperature range.[60] This study showed two possible processes with which deuterium interacts with the surface, the first of which involved immediate desorption of the newly formed molecule, detected by REMPI. In the second process the molecule was either made and remained on the surface until released when the surface temperature increased during the TPD or was synthesised during the TPD itself. These findings seemed to hint towards an Eley-Rideal type mechanism, contradicting what was calculated in earlier studies where the Langmuir-Hinselwood pathway was found to be the dominant mechanism.[47,53] Upon further investigation we can see that the two sets of results are collected under different experimental conditions; in particular Lemaire uses a thin film of

silicate while previous studies used a much rougher siliceous surface, accounting for the different mechanisms observed.[45]

The studies discussed above were carried out on bare surfaces be they amorphous carbons, olivine, forsterite or silicates. Various experiments have also been carried out to investigate the formation of hydrogen on icy mantles similar to those on the dust grains in the dense clouds of the ISM. As mentioned in a previous section, the most dominant ice component is water but other molecular ices are also present such as carbon dioxide, carbon monoxide, methanol and formaldehyde.[36] As observed above, for reactions on bare surfaces, there is some debate about whether H_2 is formed during the irradiation of the icy mantle or during the TPD.[62,63] The formation mechanism of H_2 on the icy mantles was found to depend on the atomic flux used during the experiments. If the flux of atoms was high then atoms that were adsorbing onto the surface would have a good chance of encountering another adsorbed species and reacting, forming a molecule which can desorb upon irradiation. Conversely, if the atomic flux is low the adsorbed species are likely to be more isolated.[45] When heat is applied during the TPD, the atoms can diffuse until they encounter each other and react. Amiaud *et al.* presented results that favour the first scenario where the D_2 will desorb promptly as opposed to the data presented by others, who favour the diffusive mechanism.[62,63]

1.5.2 Water Formation

The most abundant molecule in interstellar ices is water (H_2O). In dense interstellar clouds, gas-phase chemistry cannot account for the abundance of water ice observed in the ISM.[64] Therefore, the formation mechanism of H_2O is of great interest to astronomers. Van de Hulst proposed water formation occurred on the surfaces of the interstellar dust grains through surface hydrogenation of molecular oxygen, O_2.[65] In his book, van de Hulst states that if a solid oxygen molecule was exposed to hydrogen ions or atoms in the ISM then the following reactions were likely to occur (equations 1.6, 1.7 and 1.8) with little or no activation energy.

$$H + O_2 \rightarrow HO_2 \qquad 1.6$$

$$HO_2 + H \begin{cases} \rightarrow H_2O_2 \\ \rightarrow H_2 + O_2 \end{cases} \qquad 1.7$$

$$H + H_2O_2 \rightarrow H_2O + OH \qquad 1.8$$

Tielens & Hagen proposed a gas-grain model consisting of three reaction pathways for surface catalysed water formation.[66] The pathways consisted of the sequential hydrogenations of three

different states of oxygen; O, O_2 and O_3 , as outlined in the general equations below (equation 1.9, 1.10 and 1.11).

$$2H + O \rightarrow H_2O \quad 1.9$$

$$4H + O_2 \rightarrow 2H_2O \quad 1.10$$

$$6H + O_3 \rightarrow 3H_2O \quad 1.11$$

The reaction pathways proposed by Tielens and Hagen were more extensive than those shown above, involving various intermediates. In order for us to fully appreciate the pathway for water formation from hydrogenation of oxygen is summarised in the scheme below (Figure 1.6).[66]

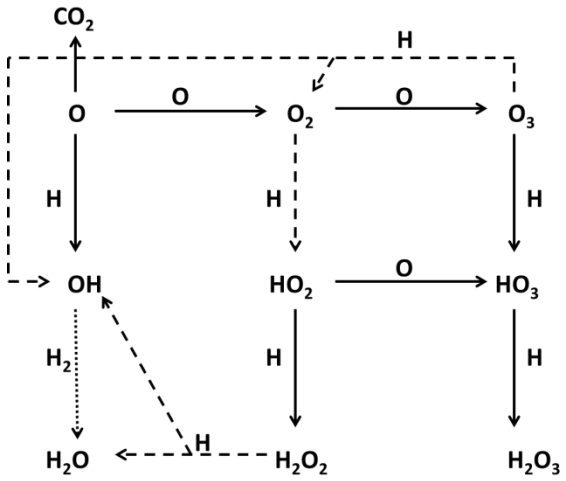

Figure 1.6: Tielens and Hagen estimation of the water formation process on dust grains in the ISM. The dashed lines represent reactions with activation barriers and the dotted lines represents the reaction between molecular hydrogen and a hydroxide.

Since the pathways described above were proposed by Tielens and Hagen, all three pathways have been studied to see if they are viable mechanisms for the formation of water. The reaction of atomic hydrogen and ozone was investigated theoretically by Cuppen *et al.* in 2007 and experimentally by Mokrane *et al.* and Romanzin *et al.*[67–70] Mokrane *et al.* investigated the deuteration of ozone on a surface held at 10 K. Romanzin *et al.* expanded upon the work of Mokrane *et al.* by conducting the same experiments but using various surface temperatures. Both authors conclude that the H + O_3 reaction pathway is the most efficient route for water formation

in dense clouds. The formation of water occurs *via* the hydrogenation of ozone to form molecular oxygen and OH. O_2 and OH can then go on to react with either H or H_2 respectively to form H_2O.[71] The hydrogenation of molecular oxygen to form water in the ISM has been extensively studied.[67,68,72–76] Miyachi *et al.* and Ioppolo *et al.* confirmed experimentally that the O_2 + H/D pathway proceeded efficiently when atomic hydrogen was dosed onto a surface coated with a multilayer of O_2 ice through the following reactions, which were expanded from the work of Tielens and Hagen in 1982 (1.12-1.15).[72,73]

$$H + O_2 \rightarrow HO_2 \quad 1.12$$

$$H + HO_2 \rightarrow H_2O_2 \quad 1.13$$

$$H + H_2O_2 \rightarrow H_2O + OH \quad 1.14$$

$$H + OH \rightarrow H_2O \quad 1.15$$

These studies were extended by Ioppolo *et al.* in 2010, who used RAIRS to analyse experiments involving the dosing of atomic hydrogen onto a multilayer of O_2 ice at astrochemically relevant temperatures (< 30 K).[76] This study addresses the temperature and thickness (of the ice) dependence of the reaction as well as the efficiency of the reaction pathways proposed by Tielens *et al.*.[66] Ioppolo *et al.* concluded that H diffusion into the ice can cause a temperature and thickness dependence in the formation of water. The competition between the formation reactions and the diffusion of the atoms increases with surface temperature because the atoms have a greater penetration depth at higher temperatures. Ioppolo *et al.* also found that the formation of H_2O and H_2O_2, shown in 1.13 and 1.14 above, were efficient under laboratory conditions. However, they suggested that owing to the presence of ozone in the ice, that there may be side reactions taking place that had not been previously accounted for in the astrochemical models. Cuppen *et al.* explained this behaviour through experiments involving the simultaneous deposition of H atoms and O_2 using the same set up as described above for Ioppolo *et al.*[67] During these experiments Cuppen *et al.* varied the ratio of H:O_2 in order to better investigate the hydrogenation process in stages. As shown in 1.10, four hydrogen atoms are needed to fully hydrogenate O_2 into $2H_2O$. When the H:O_2 ratio is high and hydrogen atoms are abundant the reaction proceeds efficiently to form water and hydrogen peroxide. However, in an oxygen dominated regime the reactions are less efficient and various intermediate molecules are detected including OH and HO_2. The reaction pathway deduced from this data is shown in Figure 1.7.

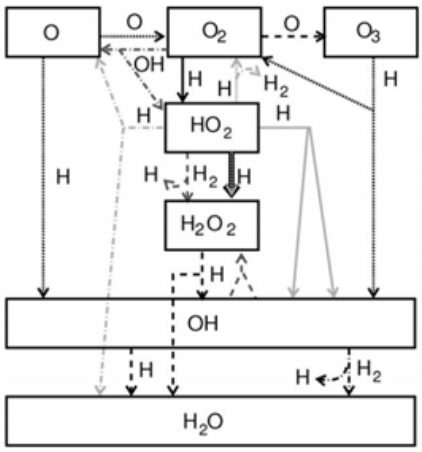

Figure 1.7: Schematic representation of the study by Cuppen et al. into water formation from molecular oxygen on the surfaces of dust grains in the ISM. The solid arrows represent barrierless reactions. The dashed arrows represent reactions with activation barriers and the dotted arrows represents the reactions where the efficiency could not be determined. Gray arrows indicate the same entering channel but different outgoing channels. Taken from Cuppen et al.

The ozone observed by Ioppolo *et al.* can therefore be explained in the reactions below (1.16, 1.17).[64,67]

$$HO_2 + H \rightarrow H_2O + O \qquad 1.16$$

$$O + O_2 \rightarrow O_3 \qquad 1.17$$

The reaction of atomic oxygen with atomic hydrogen has also been investigated. An early theoretical study showed that this radical reaction was the most likely to take place in the diffuse clouds of the ISM due to the high levels of UV radiation, meaning high abundances of atomic species.[68] Various independent studies indicated that the successive hydrogenation of atomic oxygen proceeded *via* a barrierless reaction. In their study, Dulieu *et al.* directed beams of atomic oxygen and atomic deuterium onto a porous amorphous water surface at 10 K.[77] Water formation occurred at 50% efficiency via the reactions shown below (1.18, 1.19). Jing *et al.* dosed O and D atoms onto a silicate surface held at 15 K and 25 K and they also observed the formation of water.[78] In addition, Jing *et al.* observed the formation of various other species from incomplete hydrogenation or side reactions, including D_2O_2 and O_3.

$$H + O \rightarrow OH \quad 1.18$$

$$H + OH \rightarrow H_2O \quad 1.19$$

1.5.3 Methanol Formation

Methanol and formaldehyde have been detected in various comets and in interstellar ices.[79–81] Tielens *et al.*, Charnley *et al.* and Woon *et al.* postulated that both molecules were formed through the successive hydrogenation of CO on the surfaces of the dust grains since gas-phase chemistry was unable to account for the abundances observed.[82–85] The proposed hydrogenation process is shown in the scheme below (1.20).

$$CO \xrightarrow{H} HCO \xrightarrow{H} H_2CO \xrightarrow{H} H_3CO \xrightarrow{H} CH_3OH \quad 1.20$$

The formation of methanol through successive hydrogenation of CO was first confirmed experimentally by Watanabe *et al.* (2002), who exposed an amorphous H_2O/CO ice to a beam of atomic hydrogen at 10 K.[81] Watanabe *et al.* found both formaldehyde and methanol were products, consistent with the hydrogenation of carbon monoxide. This experiment was later repeated with deuterium in place of hydrogen and both deuterated formaldehyde and deuterated methanol were detected, though at a lower yield.[86] Conversely, an independent group also carried out an investigation into the hydrogenation of CO ice. Hiraoka *et al.* (2002) deposited CO onto a silicate surface and exposed the ice layer to a beam of atomic hydrogen which resulted in formaldehyde formation, yet no methanol was detected.[87] Fuchs *et al.* later investigated this discrepancy using a gold coated copper substrate coated with few to several monolayers of amorphous CO ice.[88] The substrate was exposed to an atomic hydrogen beam and the resulting products were detected with combined RAIRS and TPD techniques. The data showed a high efficiency for both formaldehyde and methanol formation and Fuchs *et al.* concluded that the discrepancy observed between Hiraoka *et al.* and Watanabe *et al.* was likely due to the very different hydrogen flux used in both experiments. Using the results they obtained from this study, and Monte Carlo techniques, Fuchs *et al.* showed a good correlation between the rates of formation of CH_3OH and H_2CO observed experimentally and those observed in the ISM allowing them to conclude that "the surface hydrogenation of CO can now be safely used to explain the majority of the found methanol in the interstellar medium".

1.5.4: Oxygen reactivity

Oxygen is the third most abundant element in the ISM making it of considerable interest to astronomers.[33] However, the observed abundances of oxygen in the ISM cannot account for the

abundance that is predicted by astrochemical models. There appears to be less gas-phase interstellar oxygen than is expected, an observation known as a "depletion". The main theory explaining this observed depletion is that oxygen accretes onto the surfaces of the dust grains in the ISM to form ices.[34] Oxygen may therefore play a key role in a number of chemical processes that occur on the surfaces of these icy mantles.

We have already discussed the key role that oxygen plays in the formation of water on the surface of dust grains (Figure 1.7). We can see in this figure that all three states of oxygen can be successively hydrogenated to form H_2O.[67] Since the insight into the role of oxygen into water formation, many groups have investigated the reactivity of oxygen in both atomic and molecular form on astrochemically relevant surfaces.

It is widely believed that the hydrogen atoms can diffuse across the surfaces of dust grains even at low temperatures to encounter other reactive species. This diffusion is efficient because the hydrogen atoms are only physisorbed to the surface through weak Van der Waals forces.[74,89] However, in an attempt to help explain the complex chemistry observed in the ISM, Dulieu's group has investigated the diffusion of oxygen atoms on interstellar surfaces. Dulieu's group perform experiments using the "FORMOLISM" (FORmation of MOLecules in the ISM) setup shown in Figure 1.8.[90]

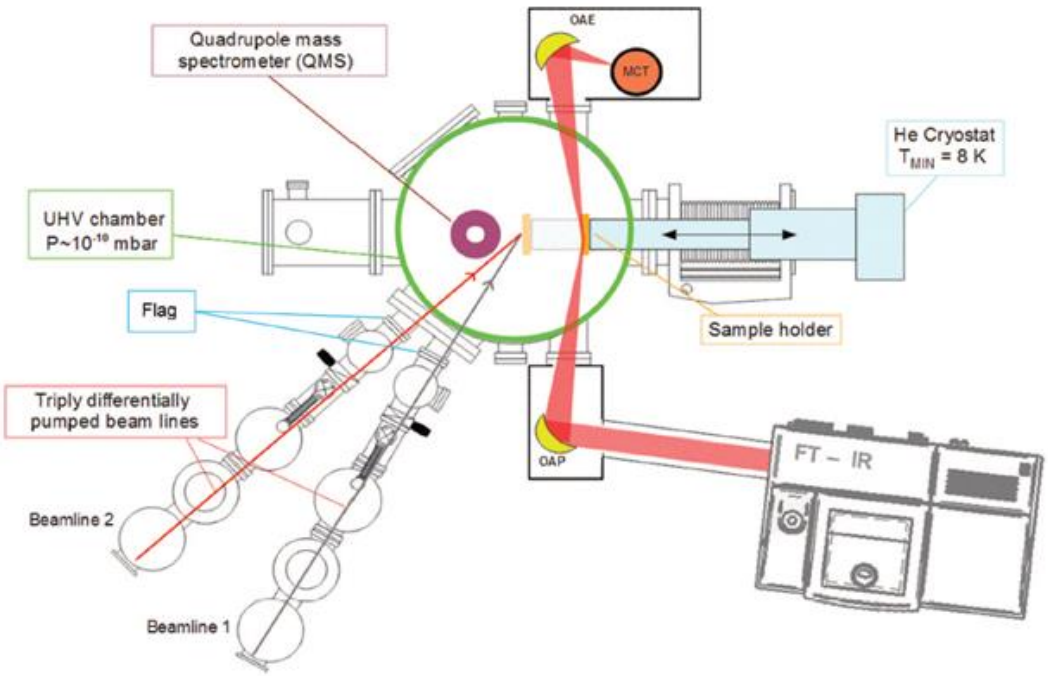

Figure 1.8: Schematic representation of the FORMOLISM setup used by Dulieu to investigate the diffusion of atomic oxygen on astrochemically relevant surfaces.

With the above setup, Dulieu's group dose a beam of atomic oxygen onto astrochemically relevant surfaces and investigate the formation of molecular oxygen and ozone, which are made *via* the following reactions: O + O and O + O_2.[91] The oxygen atoms are obtained through the dissociation of O_2 in a pyrex cylinder using a microwave discharge. These experiments showed that oxygen diffusion is a viable process on the cold surfaces in the ISM at temperatures from 6 K to 25 K.[91,92] Concurrently, Congiu *et al.* argued that the abundance of CO_2, the most abundant component of interstellar ices aside from H_2O, can only be accurately accounted for if its formation proceeds via atomic oxygen diffusion across the surface.[90] Although CO_2 formation can take place through energetic processes such as the irradiation of ices by UV photons, energetic processes are unlikely to occur with the dense clouds of the ISM as the dust particles are shielded from UV radiation. Therefore, CO_2 formation is likely to take place *via* reactions involving non energetic processes, such as CO + OH and CO + O.[91] Congiu *et al.* state that if only H atoms are mobile on the surface then the most likely products are CH_3OH and H_2O.[90] However, if oxygen diffusion occurs at a fast enough rate then CO_2 and O_3 are the more likely results, as illustrated in Figure 1.9, where both pathways are shown.

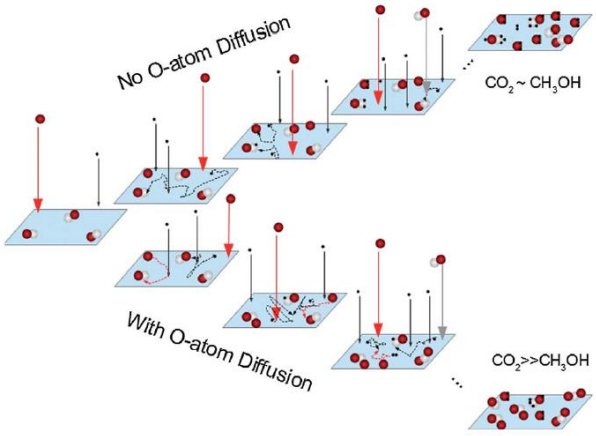

Figure 1.9: Scheme highlighting the two possible pathways on the dust grains surfaces. The top path shows the most likely products if O atoms are unable to diffuse across the surface, whilst the bottom path shows the most likely products if O atoms can diffuse. CO_2 is most likely formed from the O atom diffusion pathway. Taken from Minissale et al. (2014)

Around the same time as the study by Congiu *et al.*, Kimber *et al.* were also investigating the reactivity of oxygen atoms.[1] In particular, they dosed atomic oxygen onto a graphite surface coated with propyne ice under astrochemically relevant conditions, where the surface was held at 14 K. A TPD was then performed to analyse any possible products. From their data Kimber *et*

al. found that the reaction between propyne and atomic oxygen readily occurred under their experimental conditions to form both the single and double addition products. Using kinetic data obtained from this study Kimber *et al.* were able to conclude that this reaction was also relevant under astrochemical conditions.[1] The work by Kimber *et al.* built upon the Price groups other studies into oxygen atom reactivity in the ISM, in particular the reactions of O atoms with CS_2 and simple alkenes.[93,94] The modelling by Kimber *et al.*, along with a similar model by another group allowed a value for the desorption energy of O atoms to be determined.[95] These values were 14.0 ± 0.2 kJ mol^{-1} and 14.6 ± 1.9 kJ mol^{-1} respectively, which were in good agreement with each other and with certain astronomical observations.[96] These concurrent results indicate a higher binding energy of O atoms to the surface of dust grains than previously predicted.[97]

1.6 Summary

In this Chapter, the different regions of the interstellar medium were introduced. In particular, the environments of diffuse and dense interstellar clouds were described in detail with more focus on the dark cores of the dense clouds. Evidence was provided of the existence of dust grains within the interstellar medium. Additionally, the main theory for the origin of the Universe was summarised and the lifecycle of a star was described.

The aim of this work is to investigate the interactions and reactions of small molecules on astrochemically relevant surfaces. Therefore, previous research into the most commonly studied astrochemical molecules, hydrogen, water, methanol and oxygen, were reviewed.

In this thesis, the desorption of small molecules from graphite will be studied as will the reaction of atomic oxygen with a small unsaturated molecule under astrochemical condition. Furthermore, other investigations will focus on the interactions and reactions of molecules on different amorphous carbonaceous surfaces, which have been proposed as more realistic dust grain analogues than the standard graphitic substrate.

1.7 References

1 H. J. Kimber, C. P. Ennis and S. D. Price, *Faraday Discuss.*, 2014, **168**, 167–184.

2 E. F. Van Dishoeck, *Faraday Discuss.*, 2014, **168**, 9–47.

3 E. Herbst, *Phys. Chem. Chem. Phys.*, 2014, **16**, 3344–59.

4 A. G. G. M. Tielens, *Rev. Mod. Phys.*, 2013, **85**, 1021–1081.

5 M. Agúndez and V. Wakelam, *Chem. Rev.*, 2013, **113**, 8710–8737.

6 T. Sabri, L. Gavilan, C. Jäger, J. L. Lemaire, G. Vidali, H. Mutschke and T. Henning, *Astrophys. J.*, , 2014, **780**, 1-8.

7 P. Fleischer, *The Big Bang: Revised Edition*, Twenty-First Century Books, Minneapolis, 2006.

8 J. Silk, *On the Shores of the Universe: A Short History of the Universe*, Cambridge University Press, United Kingdom, 2005.

9 Collins Online Dictionary, http://www.collinsdictionary.com/dictionary/english/singularity, (accessed April 2020).

10 S. Lepp, P. C. Stancil and A. Dalgarno, *J. Phys. B At. Mol. Phys.*, 2002, **35**, 57.

11 F. Hoyle and W. A. Fowler, *Astrophys. J.*, 1960, **132**, 565

12 S. Mitton, *Fred Hoyle: A Life in Science*, Cambridge University Press, United Kingdom, 2011.

13 D. A. Williams and E. Herbst, *Surf. Sci.*, 2002, **500**, 823–837.

14 J. E. Dyson and D. A. Williams, *The Physics of the Interstellar Medium*, Taylor & Francis, New York, Second Edi., 1997.

15 J. Mayo Greenberg, *Surf. Sci.*, 2002, **500**, 793–822.

16 M. Steglich, C. Jäger, F. Huisken, M. Friedrich, W. Plass, H. J. Räder, K. Müllen and T. Henning, *Astrophys. Journal, Suppl. Ser.*, 2013, **208**, 2 .

17 S. T. Bromley, T. P. M. M. Goumans, E. Herbst, A. P. Jones and B. Slater, *Phys. Chem. Chem. Phys.*, 2014, **16**, 18623–18643.

18 D. A. Williams and C. Cecchi-Pestellini, *The Chemistry of Cosmic Dust*, RSC Publishing, United Kingdom, 2016.

19 E. E. Barnard, *Astrophys. J.*, 1919, **49**, 1-24

20 E. A. Bergin and M. Tafalla, *Astron. Astrophys. Rev.*, 2007, **45**, 339–396.

21 J. F. Alves, C. J. Lada and E. A. Lada, *Nature*, 2001, **409**, 159–161.

22 J. T. Robert, *Publ. Astron. Soc. Pacific*, 1930, **42**, 214.

23 R. J. Trumpler, *Publ. Astron. Soc. Pacific*, 1930, **42**, 214–227.

24 A. W. Blain, F. Combes and B. T. Draine, *The Cold Universe: Saas-Free Advanced Course*,

Springer-Verlag, Berlin, 2004.

25 NASA, Astronomy Picture of the Day, http://apod.nasa.gov/apod/ap120903.html., (accessed Jan 2017)

26 W. A. Hiltner and W. A., *Astrophys. J.*, 1949, **109**, 471.

27 T. P. Strecher and B. Donn, *Astrophys. J.*, 1965, **142**, 1681–1682.

28 B. T. Draine, in *The Cold Universe: Saas-Fee Advanced Course 32*, 2003.

29 S. Hocuk, S. Cazaux, M. Spaans and P. Caselli, *Mon. Not. R. Astron. Soc.*, 2016, **456**, 2586–2610.

30 T. Pauly and R. T. Garrod, *Astrophys. J.*, 2015, **817**, 146.

31 J. A. Noble, E. Congiu, F. Dulieu and H. J. Fraser, *Mon. Not. R. Astron. Soc.*, 2012, **421**, 768–779.

32 J. A. Noble, S. Diana and F. Dulieu, *Mon. Not. R. Astron. Soc.*, 2015, **454**, 2636–2646.

33 J. He, J. Shi, T. Hopkins, G. Vidali and M. J. Kaufman, *Astrophys. J.*, 2015, **801**, 120.

34 S. Wang, A. Li and B. W. Jiang, *Mon. Not. R. Astron. Soc.*, 2015, **454**, 569–575.

35 L. J. Allamandola, M. P. Bernstein, S. A. Sandford and R. L. Walker, *Space Sci. Rev.*, 1999, **90**, 219–232.

36 A. S. Bolina, A. J. Wolff and W. A. Brown, *J. Phys. Chem. B*, 2005, **109**, 16836–16845.

37 F. C. Gillett, T. W. Jones, K. M. Merrill and W. A. Stein, *Astron. Astrophys.*, 1975, **45**, 77–81.

38 D. A. Williams, W. A. Brown, S. D. Price, J. M. C. Rawlings and S. Viti, *Astron. Geophys.*, 2007, **48**, 25–34.

39 J. Lequeux, *Birth, Evolution and Death of Stars*, World Scientific Publishing Co. Pte. Ltd., London, 2013.

40 F. Shu, F. Adams and S. Lizano, *Annu. Rev. Astron. Astrophys.*, 1987, **25**, 23–81.

41 C. F. McKee and E. C. Ostriker, *Annu. Rev. Astron. Astrophys.*, 2007, **45**, 565–687.

42 R. B. Larson, *Mon. Not. R. Astron. Soc*, 1981, **194**, 809–826.

43 NASA, https://imagine.gsfc.nasa.gov/educators/lifecycles/LC_main_p8.html., last accessed Apr 2020

44 P. Crowther, *Astron. Geophys.*, 2012, **53**, 30–36.

45 G. Vidali, *Chem. Rev.*, 2013, **113**, 8762–8782.

46 R. J. Gould and E. E. Salpeter, *Astrophys. J.*, 1963, **138**, 393.

47 V. Pirronello, C. Liu, L. Shen and G. Vidali, *Astrophys. J.*, 1997, **475**, L69–L72.

48 Herzberg, *Mem. Soc. R. Sci. Liege*, 1955, **15**, 562.

49 M. R. C. McDowell, *Observatory*, 1961, **81**, 240.

50 H. C. van de Hulst and H. C., *Centen. Symp. December 1946. Harvard Obs. Monogr. No. 7. Contrib. Interstellar Matter, Electron. Comput. Devices, Eclips. Bin. Gaseous Envel. Earth. Cambridge, MA Harvard Obs. 1948., p.73*, 1948, **7**, 73.

51 R. T. Brackmann and W. L. Fite, *J. Chem. Phys.*, 1961, **34**, 1572.

52 R. J. Gould, T. Gold and E. E. Salpeter, *Astrophys. J.*, 1963, **138**, 408.

53 V. Pirronello, O. Biham, C. Liu, L. Shen and G. Vidali, *Astrophys. J.*, 1997, **483**, L131–L134.

54 D. Hollenbach and E. E. Salpeter, *J. Chem. Phys.*, 1970, **53**, 79.

55 V. Mennella, *Astrophys. J.*, 2008, **684**, L25.

56 N. Katz, I. Furman, O. Biham, V. Pirronello and G. Vidali, *Astrophys. J.*, 1999, **522**, 305.

57 V. Pirronello, C. Liu, J. Roser and G. Vidali, *Astron. Astrophys.*, 1999, **344**, 681.

58 G. Vidali, V. Pirronello, L. Li, J. Roser, G. Manicò, R. Mehl, A. Lederhendler, H. Perets, J. Brucato and O. Biham, *J. Phys. Chem. A*, 2007, **111**, 12611.

59 G. Vidali, L. Li, J. Roser and R. Badman, *Adv. Space Res.*, 2009, **43**, 1291.

60 J. L. Lemaire, G. Vidali, S. Baouche, M. Chehrouri, H. Chaabouni and H. Mokrane, *Astrophys. J. Lett.*, 2010, **725**, L156.

61 J. He, P. Frank and G. Vidali, *Phys. Chem. Chem. Phys.*, 2011, **13**, 15803.

62 L. Amiaud, F. Dulieu, J. H. Fillion, A. Momeni and J. L. Lemaire, *J. Chem. Phys.*, 2007, **127**, 144709.

63 J. Roser, G. Manicò, V. Pirronello and G. Vidali, *Astrophys. J.*, 2002, **581**, 276.

64 H. Linnartz, S. Ioppolo and G. Fedoseev, *Int. Rev. Phys. Chem.*, 2015, **34**, 205–237.

65 H. C. van de Hulst, *The Solid Particles in Interstellar Space Part 2*, Drukkerij Schotanus & Jeus, Utrecht Netherlands, 1949.

66 Tielens, A. G. G. M. and W. Hagen, *Astron. Astrophys.*, 1982, **114**, 245.

67 H. M. Cuppen, S. Ioppolo, C. Romanzin and H. Linnartz, *Phys. Chem. Chem. Phys.*, 2010, **12**, 12077–12088.

68 H. M. Cuppen and E. Herbst, *Astrophys. J. Lett.*, 2007, **668**, 294.

69 H. Mokrane, H. Chaabouni, M. Accolla, E. Congiu, F. Dulieu, M. Chehrouri and J. L. Lemaire, *Astrophys. J.*, 2009, **705**, 1–16.

70 C. Romanzin, S. Ioppolo, H. M. Cuppen, E. F. van Dishoeck and H. Linnartz, *J. Chem. Phys.*, 2011, **134**, 84504.

71 H. Chaabouni, M. Minissale, G. Manicò, E. Congiu, J. A. Noble, S. Baouche, M. Accolla, J. L. Lemaire, V. Pirronello and F. Dulieu, *J. Chem. Phys.*, 2012, **137**, 234706.

72 N. Miyauchi, H. Hidaka, T. Chigai, A. Nagaoka, N. Watanabe and A. Kouchi, *Chem. Phys. Lett.*, 2008, **456**, 27.

73 S. Ioppolo, H. M. Cuppen, C. Romanzin, E. F. van Dishoeck and H. Linnartz, *Astrophys. J.*, 2008, **686**, 1474.

74 E. Matar, E. Congiu, F. Dulieu, A. Momeni and J. L. Lemaire, *Astron. Astrophys.*, 2008, **492**, L17.

75 Y. Oba, N. Miyauchi, H. Hidaka, T. Chigai, N. Watanabe and A. Kouchi, *Astrophys. J.*, 2009, **701**, 464.

76 S. Ioppolo, H. M. Cuppen, C. Romanzin, E. F. van Dishoeck and H. Linnartz, *Phys. Chem. Chem. Phys.*, 2010, **12**, 12065.

77 F. Dulieu, L. Amiaud, E. Congiu, J. H. Fillion, E. Matar, A. Momeni, V. Pirronello and J. L. Lemaire, *Astron. Astrophys.*, 2010, **512**, A30.

78 D. Jing, J. He, J. Brucato, A. D. Sio, L. Tozzetti and G. Vidali, *Astrophys. J. Lett.*, 2011, **741**, L9.

79 J. Crovisier and D. Bockelee-Morvan, *Space Sci. Rev.*, 1999, **90**, 19.

80 J. V. Keane, A. G. G. M. Tielens, A. C. A. Boogert, W. A. Schuttle and D. C. M. Whittet, *Astron. Astrophys.*, 2001, **376**, 254.

81 N. Watanabe and A. Kouchi, *Astrophys. J.*, 2002, **571**, L173–L176.

82 S. B. Charnley, A. G. G. M. Tielens and S. D. Rodgers, *Astrophys. J.*, 1997, **482**, L203–L206.

83 D. E. Woon, *Astrophys. J.*, 2002, **569**, 541–548.

84 O. M. Shalabiea and J. M. Greenberg, *Astron. Astrophys.*, 1994, **290**, 266–278.

85 N. Watanabe, A. Nagaoka, T. Shiraki and A. Kouchi, *Astrophys. J.*, 2004, **616**, 638–642.

86 A. Nagaoka, N. Watanabe and A. Kouchi, *Astron. Astrophys. Suppl. Ser.*, 2005, **624**, L29.

87 K. Hiraoka, T. Sato, S. Sato, N. Sogoshi, T. Yokoyama, H. Takashima and S. Kitagawa, *Astrophys. J.*, 2002, **577**, 265–270.

88 G. W. Fuchs, H. M. Cuppen, S. Ioppolo, C. Romanzin, S. E. Bisschop, S. Anderson, E. F. van Dishoeck and H. Linnartz, *Astron. Astrophys.*, 2009, **505**, 629–639.

89 N. Watanabe, Y. Kimar, A. Kouchi, T. Chigai, T. Hama and V. Pirronello, *Astrophys. J. Lett.*, 2010, **714**, L233.

90 E. Congiu, M. Minissale, S. Baouche, H. Chaabouni, A. Moudens, S. Cazaux, G. Manicò, V. Pirronello and F. Dulieu, *Faraday Discuss.*, 2014, **168**, 151–166.

91 M. Minissale, E. Congiu and F. Dulieu, *J. Chem. Phys.*, , DOI:10.1063/1.4864657.

92 M. Minissale, E. Congiu, S. Baouche, H. Chaabouni, A. Moudens, F. Dulieu, M. Accolla, S. Cazaux, G. Manicó and V. Pirronello, *Phys. Rev. Lett.*, 2013, **111**, 1–5.

93 M. D. Ward, I. A. Hogg and S. D. Price, *Mon. Not. R. Astron. Soc.*, 2012, **425**, 1264–1269.

94 M. D. Ward and S. D. Price, *Astrophys. J.*, 2011, **741**, 121.

95 J. He and G. Vidali, *Faraday Discuss.*, 2014, **168**, 517–532.

96 G. J. Melnick, V. Tolls, P. F. Goldsmith, M. J. Kaufman, D. J. Hollenbach, J. H. Black, P. Encrenaz,

E. Falgarone, M. Gerin, Å. Hjalmarson, D. Li, D. C. Lis, R. Liseau, D. A. Neufeld, L. Pagani, R. L. Snell, F. Van Der Tak and E. F. Van Dishoeck, *Astrophys. J.*, 2012, **752**.

97 R. T. Garrod, S. L. Widicus Weaver and E. Herbst, *Astrophys. J.*, 2008, **682**, 283–302.

Chapter 2: Experimental Methodology

2.1 Overview

The Cosmic Dust Experiment is used to study the interactions of gases with astrochemically relevant surfaces under conditions similar to those in space. In particular, we are interested in the gas-grain interactions that occur within the dark, dense molecular clouds in the interstellar medium (ISM). These dense regions within the ISM have pressures as low as 10^{-14} Torr and the gas molecules and dust grains are held at temperatures of approximately 10-20 K. In the laboratory, such low temperature and pressure conditions are achieved through the combined use of ultra-high vacuum techniques and cryogenic cooling methods.

A typical experiment carried out using this apparatus involves the dosing of small amounts of gases onto a carbonaceous surface which is housed within the ultra-high vacuum (UHV) chamber. Through linear heating of the specific surface, where the gases are adsorbed as ices, we can desorb the species over a particular temperature range which ultimately relates to the binding energy of the molecule in question. The desorbing gases are detected by a quadrupole mass spectrometer (QMS) and the desorption profile of a specific gas over a temperature range is obtained. Experimental specifics regarding the gases dosed, their desorption profiles and analysis of the data can be found in subsequent chapters.

The apparatus used in the experiments discussed here has previously been used to investigate the desorption characteristics of various gases from graphite surfaces. In particular, it has been used to investigate the formation of molecular hydrogen on interstellar surfaces from hydrogen and deuterium atoms.[1-4] Additionally, it has been used to investigate the interaction and reaction of atomic oxygen with simple alkenes on a graphite surface.[5] Oxygen atoms were also co-dosed onto the graphite surface with CS_2, and the reaction between these two species was investigated.[6] These studies were further expanded upon through the investigation of the interaction and reaction of oxygen atoms with propyne.[7] Various changes have been made to the apparatus to improve the robustness of the equipment, the most notable being the induction of the QMS to replace the Time-of-Flight Mass Spectrometer. As will be discussed in greater detail later, the heating unit has also been recently redesigned to house a cartridge heater to allow for more accurate control of the surface temperature.

In general, the Cosmic Dust Experiment has been used to study and compare the desorption characteristics of various gases from different carbonaceous surfaces: Highly Oriented Pyrolytic Graphite (HOPG), amorphous ^{13}C labelled carbonaceous surfaces made *via* laser ablation (ACS)

and, most recently, amorphous C coated surfaces of various morphologies sourced from Teer Coatings. Analysis of the desorption profiles of the adsorbates can yield information on the binding characteristics of the molecules to each carbonaceous surface. Additionally, the TPD spectra can be used to identify the products of surface mediated reactions that may take place between the gases.

In this chapter, the experimental arrangement will be outlined in detail, including the vacuum setup, oxygen atom generation from a microwave source and the surface mount within the apparatus. Each experiment uses a combined Temperature Programmed Desorption (TPD) and Mass Spectrometry (MS) technique. The joint TPD-MS technique enables us to monitor and identify the gases as they desorb from the carbonaceous surface. Both TPD and MS will be discussed in detail in a later chapter (Chapter 3).

2.2 Vacuum Set-Up

The Cosmic Dust Experiment (schematically outlined in Figure 2.1) consists of two stainless steel vacuum chambers referred to as the "source chamber" and the "main chamber". The source chamber has a base pressure of approximately 10^{-8} Torr, while the main chamber reaches base pressures as low as 10^{-10} Torr.

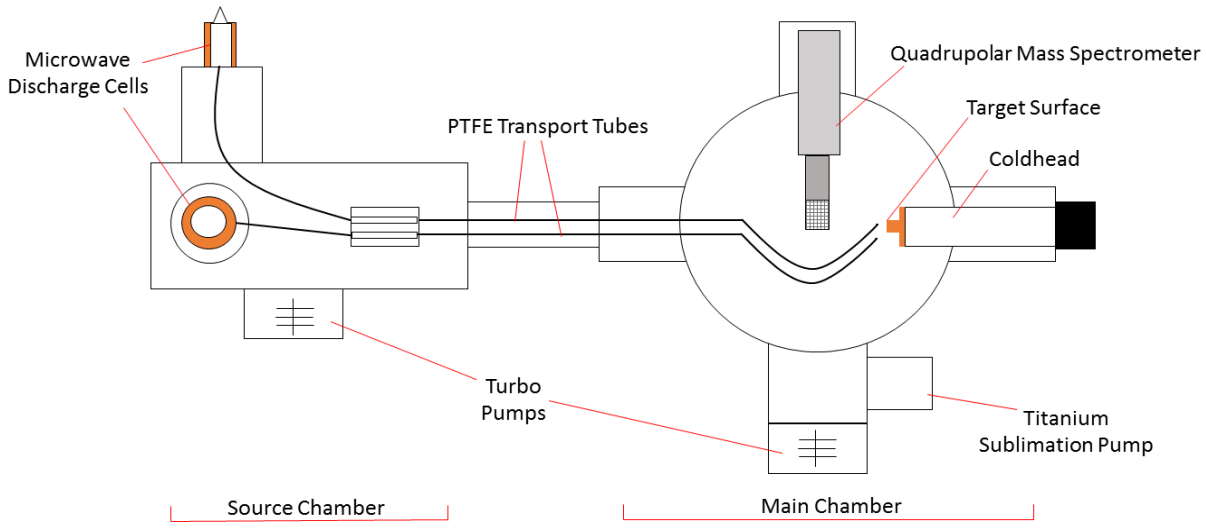

Figure 2.1: Experimental setup showing the various components of the source and main chambers.

The source chamber is a high vacuum chamber through which the various gases are introduced to the apparatus prior to dosing onto the carbonaceous surface. The vacuum is achieved through the use of a turbomolecular pump (TMP), with a two-stage rotary backing pump and, monitored

by a Penning gauge. The TMP maintains a pumping speed of approximately 400 l s^{-1} for molecular nitrogen (N_2). The chamber is equipped with two separate gas lines, allowing for the introduction of multiple gases into the experiment.

As opposed to the source chamber, the main chamber achieves ultrahigh vacuum with a base pressure of 10^{-10} Torr monitored by an ion gauge. The UHV is achieved through the use of a TMP and two-stage rotary backing pump coupled with the facility to bake the chamber. The main chamber is also equipped with a titanium sublimation pump (TSP) for efficient pumping of hydrogen gas. The desorption experiments are carried out in the main chamber; this chamber contains the mount for the carbonaceous surface and the mass spectrometer for monitoring the desorbates. In order to mimic the conditions of the ISM, the pressures within this chamber are kept as low as possible *via* a low flux of molecules from the source chamber and through baking, prior to and between experiments. The baking temperature of the apparatus is limited to 60 °C/ 333 K as opposed to the normal baking temperature for stainless steel chambers (100 °C/ 373K), resulting in more lengthly baking periods. The chamber cannot be baked to higher temperatures due constrictions of the cryogenic coldhead (used to cool the surface) and the thermodiode, which is attached to the surface. These devices cannot be heated above 60 °C. Recent experimental developments mean the baking is now controlled by the Eurotherm Nanodac temperature controller, where the baking apparatus will switch on/off if the temperature falls outside of a specified temperature range.

Despite the best efforts, the low pressures achieved in these experiments have to be several orders of magnitude higher than the actual pressures of the dense clouds within the ISM (10^{-14} Torr). It is currently extremely difficult for researchers to reach the low pressures needed for direct comparison with the ISM and the vacuum technology needed to reach these pressures is not readily available for university laboratories. Furthermore, in order to maintain sufficiently low pressures within the main chamber during dosing experiments, the molecular flux of the gases would have to be greatly reduced. However, this would result in extremely lengthy experiments. Therefore, at UCL, the Cosmic Dust experiment is constructed such a way, so as to allow researchers to investigate the desorption characteristics and reactions of astrochemically relevant molecules on a manageable timescale.

2.3 Transport of Gases

Gases are introduced into the Cosmic Dust apparatus *via* the source chamber. The source chamber contains two separate gas delivery lines and each line is pumped by the same rotary pump, allowing the cells to reach base pressures as low as $1x10^{-3}$ Torr. The presence of two gas lines ensures that multiple gases can be dosed onto the surface simultaneously if required. Both

delivery lines are equipped with identical microwave discharge cells for the optional dissociation of the molecules into atoms during dosing. Currently, the microwave discharge is exclusively used to generate atomic oxygen (as discussed below) although with previous experiments on this apparatus, the microwave discharge was used to generate atomic hydrogen. The cell set-up for both delivery lines is illustrated in Figure 2.2. Each cell is made of Pyrex glass, with a metal-glass seal connecting the glass cell to the gas inlet line. Gases are transported from the cylinder to the cell then transported onwards via polytetrafluoroethylene (PTFE) tubes with ¼ in outer diameter (OD). PTFE is used because of its inert properties which ensure that the gases do not react with the transport medium before reaching the surface.

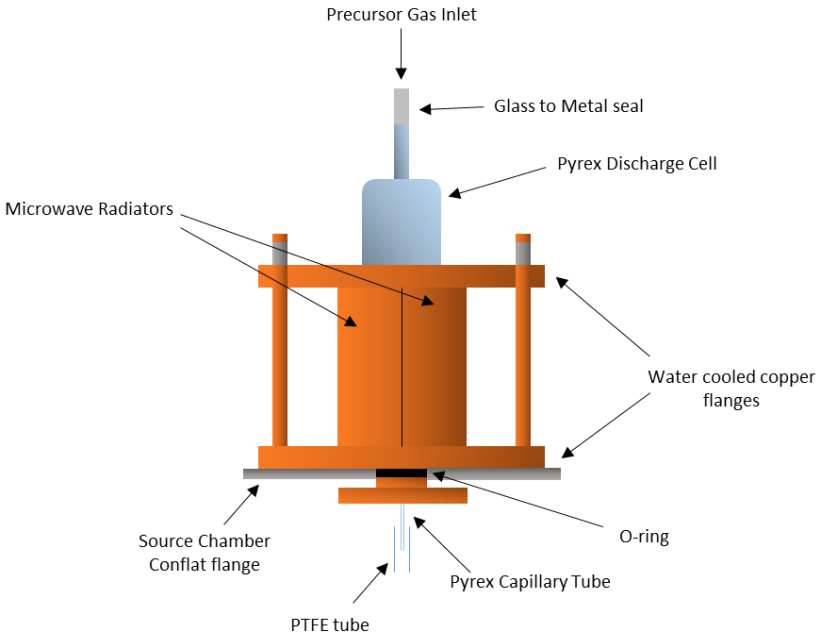

Figure 2.2: Schematic showing the discharge source through which gases are introduced to the high vacuum system.

The gases are dosed into the main chamber through the PTFE tubes. The main chamber is sealed from the higher pressures of the source chamber by a brass plug which is also used to secure the PTFE tubes in place. The PTFE lines are differentially pumped prior to entering the main chamber to ensure a low atomic/molecular flux. As shown in Figure 2.3, the tube from each cell is connected to a separate PTFE connector, each of which is fitted with a pumping hole that can be a variety of sizes depending upon the desired dose. The pumping holes are in place to ensure the ultra-high vacuum conditions in the main chamber are maintained as they ensure the gas delivery line can be differentially pumped before the gases are transported to the main chamber. This pumping results in the majority of the gases introduced into the apparatus being pumped away, therefore only a small amount will be able to enter the main chamber. The larger the pumping holes then the more gas is pumped away, hence the smaller the dose that enters the main chamber. The experiment is set up as such because it is more convenient to accurately control a higher gas pressure within the delivery lines and pump most of the gas away than to attempt to accurately control and monitor lower pressures within the cell.

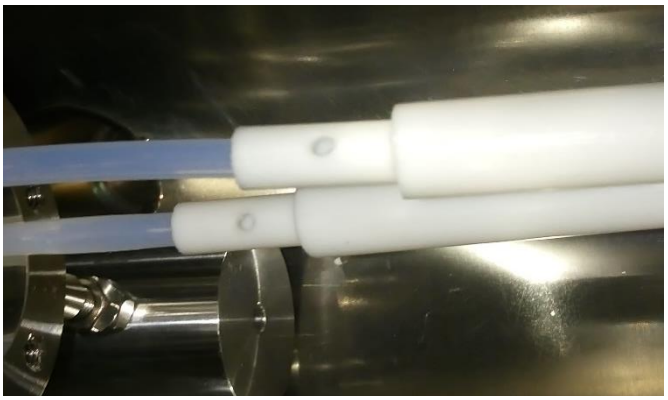

Figure 2.3: Image showing the pumping holes on the PFTE connectors. The size of the holes can be varied to change the amount of gas reaching the main chamber.

After being differentially pumped *via* the pumping holes, the remaining molecular flux is transported from the source chamber to the main chamber through PTFE tubes traversing the brass plug. The brass plug and an O-ring act as a seal between the two chambers thus ensuring that the only gas introduced into the ultra-high vacuum chamber is through the two dosing lines, which deliver the gases directly to the target surface. The dosing lines are held in place adjacent to the target surface by a copper mount which holds the lines approximately 10 mm away from the surface, as shown in Figure 2.4. There is also a secondary mount to which the PTFE tubes can be attached which is directed towards the mass spectrometer. The secondary mount is used in gas analysis studies (e.g., to check on the dissociation of O_2) and it allows the gases to be directly detected by the quadrupole mass spectrometer without interacting with the surface. The two different mounts are made of stiff copper wire mounted on the end of the cold shield, and they ensure that the PTFE tubes do not move during dosing.

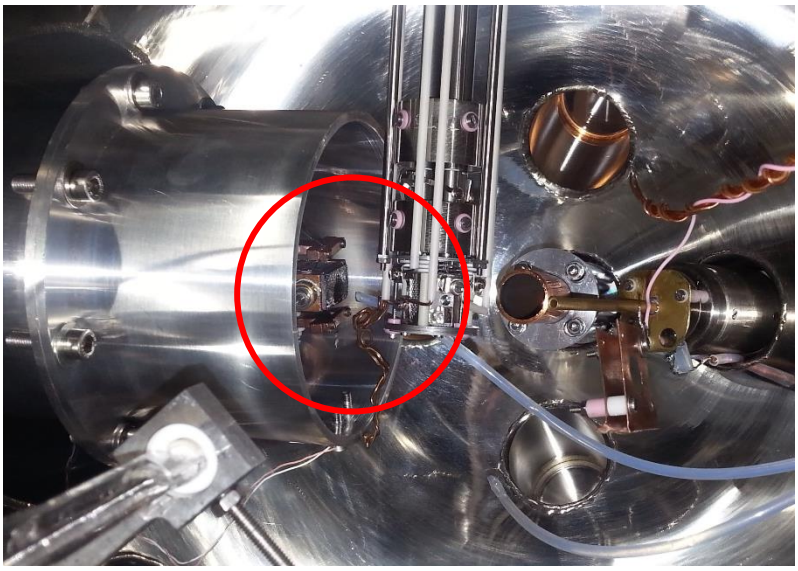

Figure 2.4: Image showing the set-up within the main chamber. The PTFE delivery lines are mounted directly above the target surface, as outlined in red.

2.4: The Surface Mount

Traditionally, in experiments at UCL and elsewhere, a HOPG (highly ordered pyrolytic graphite) surface is used as a carbonaceous dust grain analogue. Indeed, many experiments in this thesis take place on such a graphite surface. However, we are also interested in more disordered carbonaceous structures as they are more likely to occur in the interstellar medium. As a result, this thesis presents studies of desorption characteristics and reactivity of various astrochemically relevant molecules on graphite, as well as some amorphous carbonaceous surfaces (ACSs) made via laser ablation or by Teer Coatings in a patented coating technique (both processes will be addressed in more detail elsewhere). Each carbonaceous (or "target") surface measures approximately 20 mm x 10 mm x 2 mm and is mounted upon a closed cycle He cryostat. The cryostat has a base temperature of 8 K, allowing for a minimum experimental surface temperature of 10-18 K owing to the extra heat load induced by the mount.

The target surface is mounted a few millimetres away from the centre of the source region of the QMS, as shown in Figure 2.4. The surface mount is shown in Figure 2.5. The surface sits upon a copper block, which houses a cartridge heater. The introduction of the cartridge heater is a recent experimental development. This heater replaced a tantalum strip heater in order to allow better temperature control. By combining the action of the coldhead and the heater, a surface temperature range of 10-500 K is achieved. The surfaces are cleaned at temperatures from 400 K to 500 K. The current experimental arrangement allows for precise temperature control of the target surface over time, hence one is able to perform TPD experiments, which will be discussed further in subsequent chapters. Whilst typical interstellar reactions will take place within the

range of 10 -20 K, reactions at various higher temperatures were investigated in order to gain an insight into the kinetics and desorption characteristics of certain molecules.

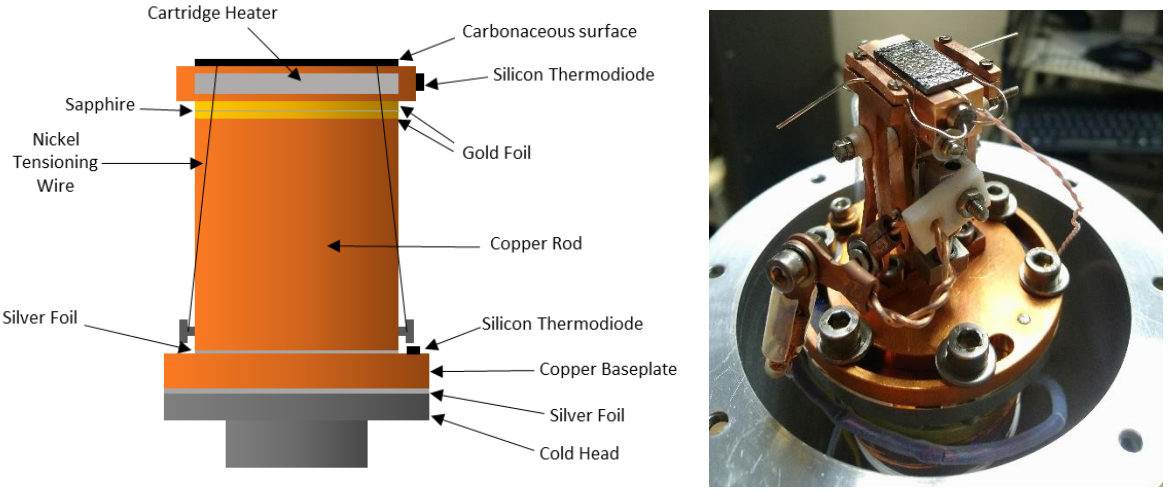

Figure 2.5: Schematic of the surface mount within the main chamber, and image showing the actual surface mount with a graphite target surface.

The surface is held in place by two nickel tensioning wires secured to the copper rod, which are sufficiently tense to ensure good thermal contact between the surface, the copper block heating unit and the coldhead. Good thermal contact is also achieved through the use of gold or silver between the copper components. A strip of sapphire is placed between the copper rod and the heater. Sapphire is known to have unique thermal conduction properties. Specifically, sapphire is an excellent thermal conductor below temperatures of 50 K and a poor thermal conductor at temperatures above 200 K. Due to its poor thermal conductivity at high temperatures, the sapphire will restrict heat transfer from the heater down to the coldhead which, as previously mentioned, cannot be heated above 330 K. As heat cannot transfer down the rest of the surface mount, the surface itself can be heated to the high temperatures required for cleaning, while the temperature of the coldhead remains at 50 K. A coldshield surrounds the surface mount, acting as a radiation shield to ensure that the surface temperature is unaffected by black body radiation from other elements in the chamber, such as the steel walls.

The surface temperature is monitored by a thermodiode, which is mounted on the side of the copper block, as shown in Figure 2.5. N-type thermocouples are also attached to the setup in various places to provide temperature readings to check the temperature of the mount and the coldhead. In particular, one N-type thermocouple is located under the surface, where it is

wrapped in gold and placed within a small grove that will allow it to have good thermal contact with the surface and provide an accurate surface temperature. The other thermocouple is located at the end of the coldshield. When a specific surface temperature is required, a Lakeshore diode reader records the current temperature from the thermodiode attached to the side of the copper block. The diode reader then sends a 0-10 V signal to a Eurotherm Nanodac temperature controller. The controller drives a power supply (TTi Power Supply Unit), which in turn will run the desired current through the cartridge heater until the required temperature is reached, at which point the controller will shut off the power supply. The Nanodac allows for linear control of the surface temperature, therefore during the course of a TPD experiment the surface can be heated from 10-300 K at a constant rate (usually 10 K min^{-1}). As a result of the linear heating rate, the desorption temperatures of the species desorbing from the surface can be monitored and ultimately a desorption energy can be estimated, as will be discussed in detail in further chapters.

2.5: Oxygen Atom Generation

As mentioned above, the oxygen atoms are generated within the microwave discharge cell on one of the gas inlet lines. As discussed above, each inlet line contains a Pyrex cell, which is 260 mm long with an outer diameter (OD) of 25.5 mm and is equipped with a Cajon glass to metal seal to connect the cell to the gas cylinder. During the course of an experiment, oxygen gas (99.5% BOC, as received) is introduced into the discharge cell. Prior to the start of the experiment, the line is flushed with the dosing gas multiple times to remove any contamination that may already be in the line. To generate atomic oxygen, microwaves are applied to the cell resulting in the production of an O/O_2 gaseous mixture . A needle valve is used to control the gas flow into the cell. The gas is irradiated with microwaves *via* the two-piece radiators shown in Figure 2.6a. These copper radiators surround the discharge cells and are designed in such a way so as to ensure as little clearance as possible is present between the cell and the radiator, thus enabling efficient coupling of the microwaves to the plasma whilst reducing stress on the Pyrex cells.[8,9] As shown in Figures 2.6a and 2.6b, the radiator is divided into two parts, where each half has a pair of 2 mm wide slots linking to a female type-N connector. When microwaves are applied to the cell, a potential difference is generated between the two radiators across the walls of the slots. The electric fields generated from all four slots are in phase as the centre of each is half a wavelength apart from each adjacent slot. Since the waves are in phase, no tuning is required, and the microwaves are superimposed, as is evident in the etching pattern observed in old cells (Figure 2.6c).

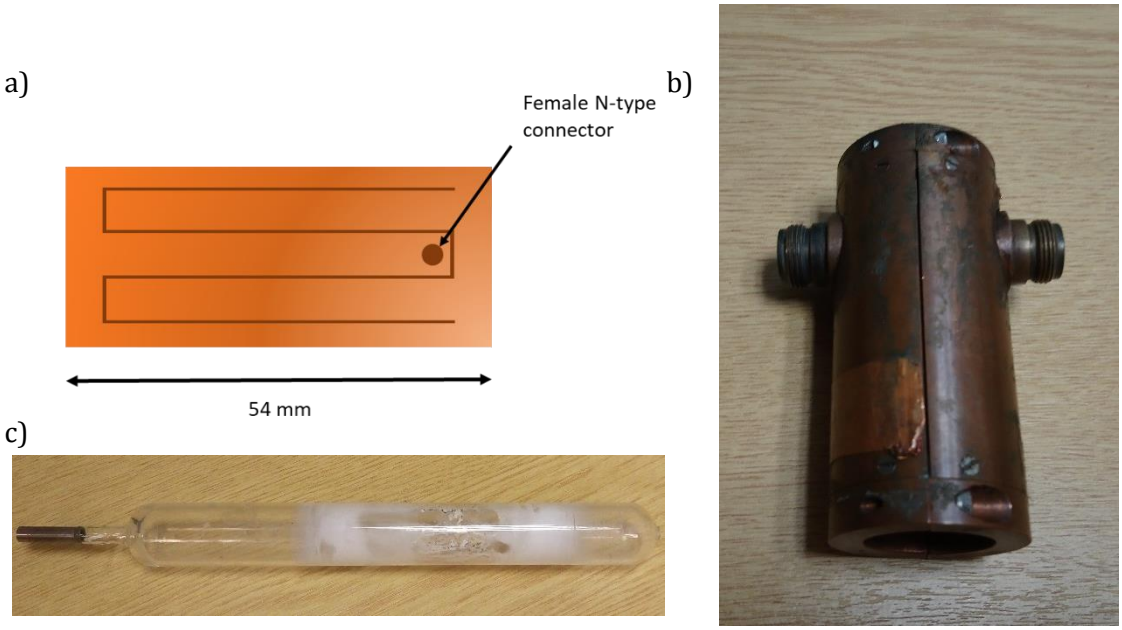

Figure 2.6: a) Schematic of half the copper radiator, showing the N-type connector, b) image of the copper radiator, c) image of an old Pyrex cell showing the etching by the discharge.

Atomic oxygen is generated in the microwave discharge of molecular oxygen. To light the discharge, the high voltage tip of a Tesla coil is applied to the side of the Pyrex cell. This spark induces the ionisation of a few of the molecules within the Pyrex cell, generating free electrons. These electrons oscillate within the electric field that is established across the cell by the microwave superposition. The oscillating electrons collide with more molecules in the cell and further ionisation occurs in a "cascade". A plasma is created within the discharge cell as a result of this cascade effect. The plasma is at low temperature, meaning that although the electrons oscillate within the discharge cell, the gas within the cell remains at or close ambient temperature as the atoms and molecules are too heavy to oscillate with the field.

A 300W Sairem microwave power supply unit is used to generate the required microwaves at a frequency of 2.45 GHz. Two Sucoflex wave guide cables are used to transfer the microwaves to the cell. The wave guides are not the same length but are instead half a wavelength different which allows the microwaves to arrive at either side of the cell 180° out of phase.[9] The half a wavelength difference in length coupled with the half a wavelength separation between adjacent slots within the radiator means the generated electric fields at each slot are in phase and can be superimposed as mentioned above. In the majority of experiments discussed in this thesis, a microwave power of 200-250 W was used to generate atomic oxygen. In order to increase the lifetime of the microwave unit, an optimum microwave power was chosen before each set of experiments to reduce the reflected power. If too much power is reflected back to the microwave generator the

magnetron will overheat and this, over time, will inhibit its ability to function efficiently. Ideally, a reflected power of less than 10% is recommended.

During the course of an experiment the copper radiator can become hot, which would in turn heat the cell. Consequently, the copper radiators are cooled by two water cooled copper flanges situated at either end of the radiators. Other research has shown that the lower the temperature of the cavity, then the greater the yield of atomic species, as under warmer conditions recombination reactions readily take place on the walls of the cell.[9] In addition, the copper radiators are flush to the cell meaning any temperature change to the Pyrex could cause it to expand into the radiator, therefore water cooling is of vital importance to reduce cell expansion. With the current setup the radiators are also air cooled by a fan positioned close to the discharge cell. Before being added to the apparatus, each new Pyrex cell is soaked in phosphoric acid for 12 hours. The acid is thought to passivate the cell surface and can help prevent recombination reactions.[10]

Despite the cooling, passivation and low pressure conditions employed to reduce recombination, it is impossible to obtain a pure beam of oxygen atoms with our current setup. As a result, an O/O_2 gas mixture is dosed onto the surface. Maximum dissociation efficiency measured in the target chamber is currently approximately 10%. Although this number is small, it is enough to allow us to investigate what reactions will occur between the O atoms and other gases that are dosed onto the surface. Analysis of the gas when the PTFE tubes are mounted on the secondary mount directly at the QMS (as mentioned above) allows us to be certain that there are still O atoms present within the gas mixture prior to it being dosed onto the surface.

2.6: Experimental developments for temperature control

2.6.1: Temperature control

As mentioned above and illustrated in Figure 2.5, the surface temperature is measured *via* a thermodiode situated on the side of the copper heating block. The copper heating block shown in Figure 2.5 houses the cartridge heater, which is used to heat the surface. PID control is used to ensure a linear heating rate during desorption experiments.

Prior to the installation of the current copper block and the cartridge heater, the surface was heated through application of a current to a tantalum strip heater. However, oscillations in the heating rate manifested in the desorption spectra causing corresponding signal fluctuations during the TPD cycle. The method used to calculate the desorption energy of an adsorbate will be outlined in detail in Chapter 3, however here it is noted that the small oscillations in the heating

rate caused subsequent oscillations in our data leading to inaccurate values for the desorption energy being obtained. The perturbations observed in the spectra could not be damped by tuning of the PID settings and were thought to be intrinsic to the instrumentation. The oscillations are more noticeable at lower temperatures, and so are particularly apparent in our oxygen and argon data, where both molecules initially desorb at temperatures of approximately 30 K, as shown in Figure 2.7.

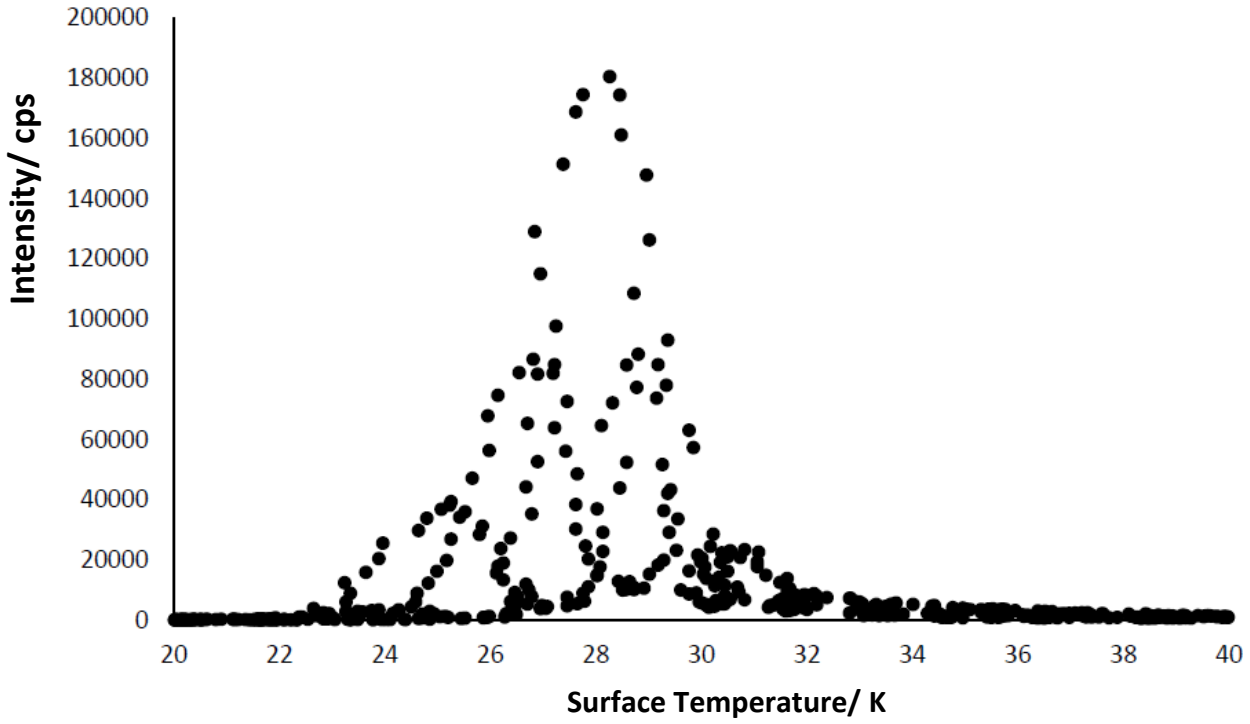

Figure 2.7: TPD desorption spectrum of Ar dosed at 15K onto a graphite surface, where the surface was heated using the tantalum strip heater and not the copper block.

In order to achieve better data quality, a new heating system was designed and installed. A 100 W cartridge heater was installed to replace the tantalum strip heater. The design for the new heater mount, the completed mount and the new setup are shown in Figure 2.8.

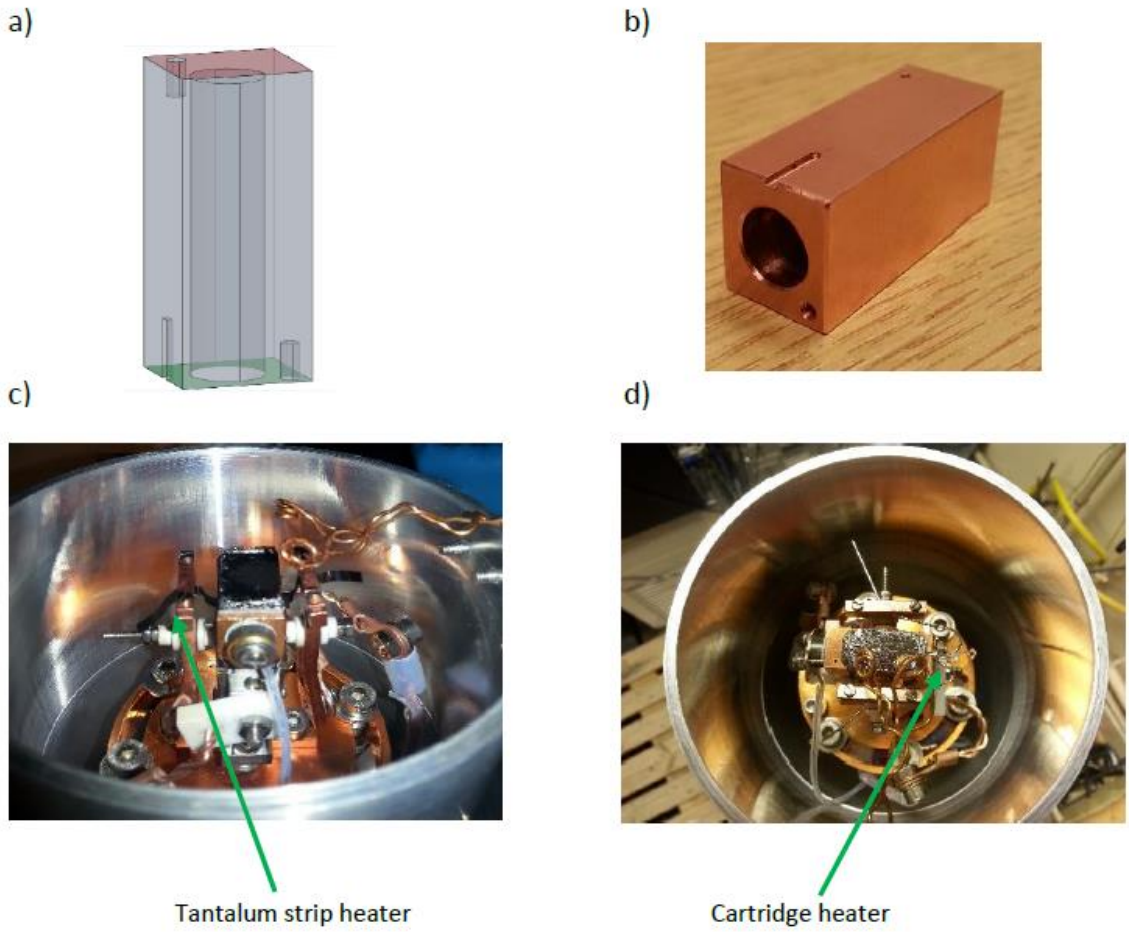

Figure 2.8: a) The AutoCAD design for the new heating block, b) image of the completed copper heater mount for the cartridge heater, c) old heating block set up with tantalum strip heater highlighted, d) new heating block set up, with the cartridge heater

The installation of the cartridge heater greatly reduced the oscillations that were observed in the spectra. As can be seen in later Chapters, some of the data still contained a small number of these oscillations. The oscillations are further reduced by fitting the data, thereby removing the artefacts from the spectra and allow more reliable values for the desorption order and desorption energy to be obtained.

2.6.2 Temperature offset

Comparison between the desorption temperatures measured using the current apparatus and desorption temperatures of the same gas by other groups indicated that there was a temperature offset between the recorded temperature and the actual temperature of the surface. Table 1 shows the recorded desorption temperatures for a variety of gases and their desorption temperatures reported in the literature.[11-16]

Table 1.1: Table showing the differences between the measured peak desorption temperatures and those reported in the literature.

Molecules	Measured temperature (K)	Literature reported temperature (K)
NH_3	84	94 [11]
MeOH	124	144 [16]
CO_2	71	83 [12]
CO_2 lower	66	77 [13]
CO_2 multilayer	76	86 [13]
O_2	27	32 [12,14]
CO	19	26 [15]

By plotting the measured desorption temperatures against the literature reported value of desorption temperature, we were able to identify that the temperatures measured experimentally vary linearly from the values reported in the literature, as highlighted in Figure 2.9.

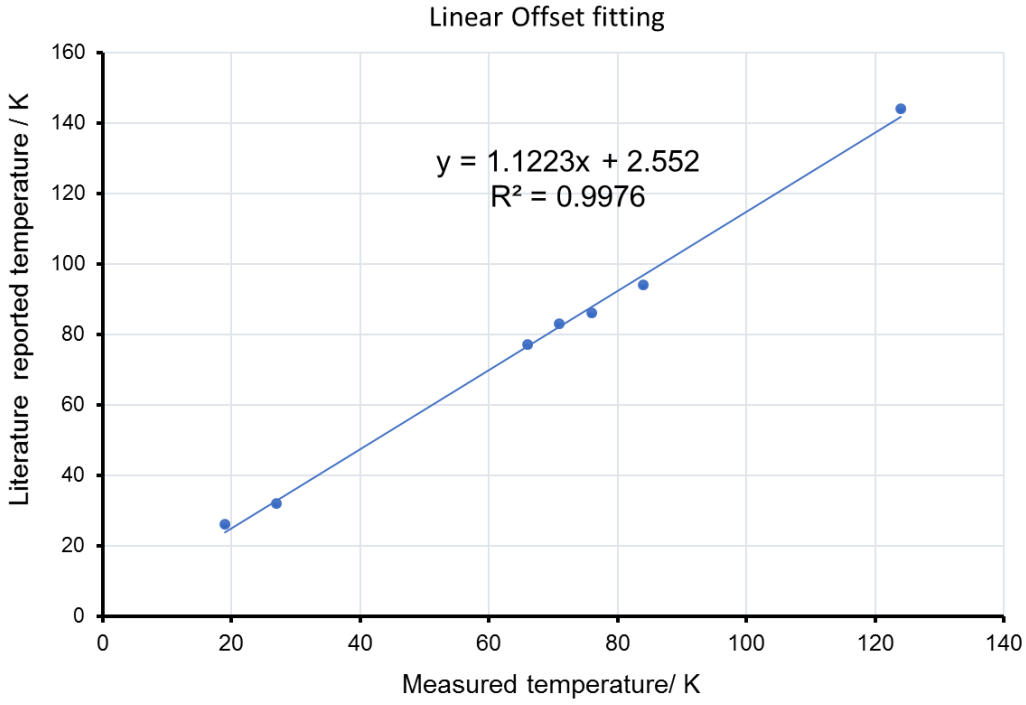

Figure 2.9: Plot showing the linear difference between the measured desorption temperature and the temperatures reported in the literature.

Owing to the linearity observed in Figure 9, we assumed that the offset between measured and actual temperature is perfectly linear across the entire temperature range used in our studies. For this reason, all recorded temperatures in this thesis have been adjusted using the equation shown in Figure 9.

2.7 Summary

In summary, this chapter has provided a detailed description of the Cosmic Dust apparatus used in the desorption experiments discussed in this study. In particular, this chapter addressed the generation of the high and ultra-high vacuum environments necessary to mimic the conditions in the ISM, as well as explaining how the gases are transported from one chamber to the other and how the atomic oxygen atoms used in the reactions discussed in subsequent chapters are generated. Furthermore, details about experimental developments have been provided and the specifics regarding how the observed temperature offset is corrected have been explained.

2.8 References

1 J. S. A. Perry, J. M. Gingell, K. A. Newson, J. To, N. Watanabe and S. D. Price, *Meas. Sci. Technol.,* 2002, **13**, 1414.

2 S. C. Creighan, J. S. A. Perry and S. D. Price, *J. Chem. Phys.*, 2006, **124**, 114701.

3 F. Islam, E. R. Latimer and S. D. Price, *J. Chem. Phys.*, 2007, **127**, 064701.

4 E. R. Latimer, F. Islam and S. D. Price, *Chem. Phys. Lett.*, 2008, **455**, 174-177.

5 M. D. Ward, I. A. Hogg and S. D. Price, *Mon. Not. R. Astron. Soc.*, 2012, **425**, 1264–1269.

6 M. D. Ward and S. D. Price, *Astrophys. J.*, 2011, **741**, 121.

7 H. J. Kimber, C. P. Ennis and S. D. Price, *Faraday Discuss.*, 2014, **168**, 167–184.

8 D. P. Higgins, R. W. McCullough, J. Geddes, J. M. Woolsey, M. Schlapp and H. B. Gilbody, *Adv. Eng. Mater.*, 1995, **99**, 177–183.

9 R. W. McCullough, J. Geddes, A. Donnelly, M. Liehr, M. P. Hughes and H. B. Gilbody, *Meas. Sci. Technol.*, 1993, **4**, 79–82.

10 A. Donnelly, M. P. Hughes, J. Geddes and H. B. Gilbody, *Meas. Sci. Technol.*, 1992, **3**, 528–532.

11 A. S. Bolina and W. A. Brown, *Surf. Sci.*, 2005, **598**, 45–56.

12 H. Ulbricht, R. Zacharia, N. Cindir and T. Hertel, *Carbon N. Y.*, 2006, **44**, 2931–2942.

13 J. A. Noble, E. Congiu, F. Dulieu and H. J. Fraser, *Mon. Not. R. Astron. Soc.*, 2012, **421**, 768–779.

14 H. J. Kimber, C. P. Ennis and S. D. Price, *Faraday Discuss.*, 2014, **168**, 167–184.

15 W. A. Brown and A. S. Bolina, *Mon. Not. R. Astron. Soc.*, 2007, **374**, 1006–1014.

16 A.S. Bolina, A. J. Wolff and W. A. Brown, *J. Chem. Phys*., 2005, **122**, 044713

Chapter 3: Analytical Techniques

3.1 Overview

This chapter describes the techniques used to gather and analyse the data that will be presented in later chapters. In particular, the mass spectrometer and temperature programmed desorption techniques will be explained.

3.2 Mass Spectrometry

The mass spectrometer is an instrument that can be used to measure the abundances of ions with different mass-to-charge (*m/z*) ratios.[1] In mass spectrometry, the application of electric or magnetic fields is used to separate ions with different *m/z* ratios, as will be discussed below.[2] Mass spectrometry can also be used to identify unknown molecules from their fragmentation patterns in the mass spectrometer. Specifically, the nominal mass of the unknown molecule can be determined and further analysis of the fragmentation patterns can help elucidate the structure of the ion itself. [3] Mass spectrometry is, therefore, one of the most widely used techniques in chemistry. In this study, mass spectrometry is used to detect the reactants and products that desorb from a surface as it is heated. As discussed in the previous chapter, during the course of an experiment, gaseous molecules are dosed onto a cooled surface, where they will freeze out into molecular ices. As the surface is heated the molecules will desorb over specific temperature ranges, and they are then detected by the mass spectrometer. The detection of the desorbing species helps one to understand how the different molecules interact with the surface as well as identify any reactions that may be taking place on the surface. Such studies will ultimately provide more information on the interactions and reactions of these molecules within the interstellar medium.

3.2.1 The Basics of Mass Spectrometry

As briefly mentioned above, mass spectrometry can be used to separate various ions with different *m/z* ratios based upon the interaction of these ions with an applied electric and/or magnetic field.[2] The ions are charged particles and so any applied field (magnetic or electric) will affect the position of the ion within a mass spectrometer. Other non-charged particles such as molecules or radicals are not detected by the mass spectrometer.[2]

A mass spectrometer is comprised of three basic stages as illustrated below in Figure 3.1.[2] The Ion Source is the source of the charged particles. After the ions are produced, they enter the *m/z* analyser, where they are separated using a variety of techniques (the implementation in this work will be described in greater detail below) and finally they reach the detector. The mass

spectrometer separates the ions based upon their mass-to-charge ratio, which is the mass of the ion divided by the charge of the ion.[2] Normally in mass spectrometry the charge of the ion is equal to the charge of the molecular ion (+1), and so in most cases the *m/z* ratio is indicative of the actual mass of the ion.[2] A mass spectrometer is always operated under vacuum conditions to reduce the number of unwanted ion collisions which could skew the position of the ions within the mass spectrometer, change their trajectory or cause additional fragmentation.[1,2] Moreover, the detector itself operates under high vacuum conditions as highlighted in Figure 3.1.[1]

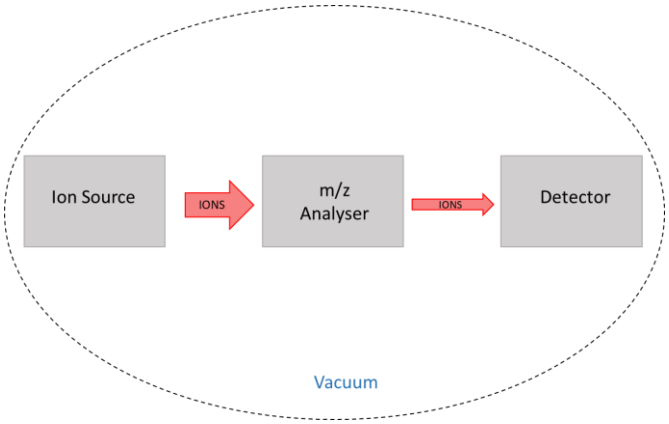

Figure 3.1: Diagram illustrating the three basic steps of a mass spectrometer. Ions are introduced via the ion source, in either solid, liquid or gaseous form depending upon the technique being used. The ions travel through the m/z analyser (discussed below) where they are separated. The ions are then detected and can be identified through analysis of the mass spectrum.

3.2.2 Quadrupole mass spectrometer

The quadrupole mass spectrometer (QMS), also known as the Transmission Quadrupole or the Quadrupole Mass Filter (QMF) was invented by Wolfgang Paul *et. al.* in the early 1950's.[2,4] This work uses such a QMS as it is mass-selecting, as will be described in greater detail below. The QMS is a non-magnetic *m/z* analyser, which uses a combination of radio frequency (RF) fields and stable DC fields to separate the ions by their mass-to-charge (m/z) ratio.[2]

In this apparatus, a standard Residual Gas Analysis (RGA) Triple Filter Quadrupolar Mass Spectrometer from Hiden Analytical (Hiden 3F series RGA QMS) is used, with an operating range of 1-300 amu and unit mass resolution. The spectrometer is controlled using MASsoft software. As will be discussed in more detail below, the QMS allows for mass selectivity, where specific masses are selectively monitored during an experiment. In the experiments presented in this work, the mass selectivity of the QMS is used to monitor the desorption of specific relevant ions only as they desorb from the carbonaceous surface, and a TPD spectrum of each of these ions is obtained (as will be discussed in more detail later in the Chapter). If a non-mass selective instrument (such as the Time-Of-Flight Mass Spectrometer (TOF-MS)) was used instead, then a

series of complete mass spectra would need to be run as the temperature of the surface was increased, then the data on the ions of interest would need to be extracted from the mass spectra. The mass selectivity of the QMS ensures that the desorption characteristics of only the ions of interest are recorded, allowing for a more detailed study into how these ions interact with the surface and each other.

3.2.2.1 The Ion Source

During the desorption stage of the experiments, when the adsorbed gas molecules are desorbing from the surface over specific temperature ranges, the desorbing gases enter the source cage of the mass spectrometer where they undergo Electron Ionisation (EI). In the source cage, the gas molecules or atoms are bombarded with electrons, generated via thermionic emission when a potential is applied to the oxide-coated iridium filament (Figure 3.2).[5] The potential applied to the filament determines the energy of the ionising electrons in the ion source. The potential applied to the filament in the experiments discussed in this thesis is 70 eV (e^-). The bombardment of the gas molecules by energetic electrons within the source cage generates positively charged ions, including the molecular ion and fragment ions from the original gas species.[5] However, the generation of ions from molecular rearrangement, metastable ions and doubly charged ions is also possible. The positive ions are extracted from the source cage *via* a focus plate. A negative voltage is applied to the focus plate (-90 V) to ensure that the cations are accelerated into the quadrupole filter while electron transmission into the filter is blocked. [5]

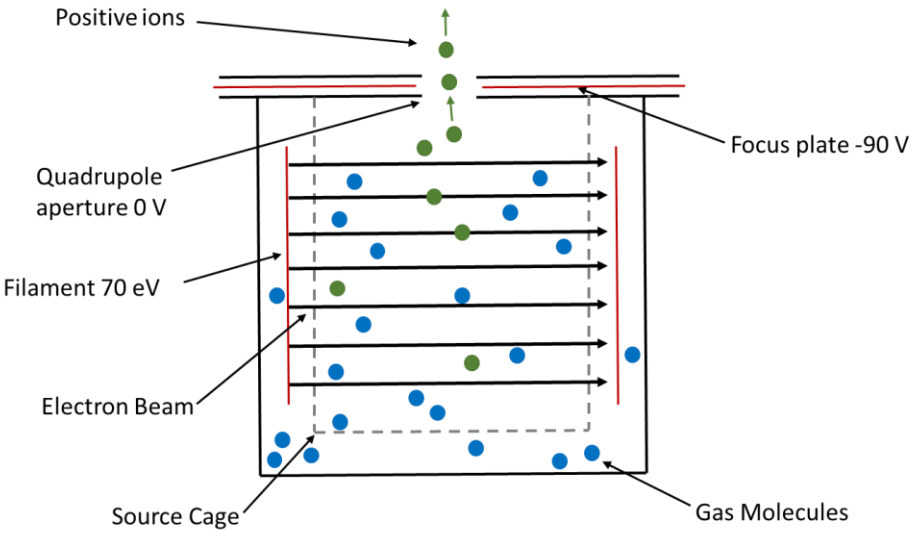

Figure 3.2: Diagram illustrating the ion source region of the mass spectrometer. Blue dots represent the molecules, while green dots represent cations made after contact with the electron beam.

3.2.2.2 The m/z Analyser

The quadrupole mass filter consists of 4 longitudinally parallel circular rods of equal lengths, as seen in Figure 3.3.[2] DC (direct current) potentials and AC (alternating-current) potentials in the radiofrequency (RF) range are applied to these rods.[3] The same DC potential is applied to the rods positioned opposite to each other, as shown in Figure 3.3. The combined DC and RF potentials generate overlapping electric fields around each rod. As the positive ions enter the mass filter their trajectories are affected by these fields, which will be discussed in greater detail below. The degree to which their trajectories are affected is dependent upon the m/z ratio of the ion.[1–3] When the ions enter the mass filter, the vast majority of the species are unstable within the electric fields and are deflected and neutralised upon impact with the rods.[2] Only ions with a particular m/z ratio can resonate within the fields and traverse the length of the mass filter to be detected.

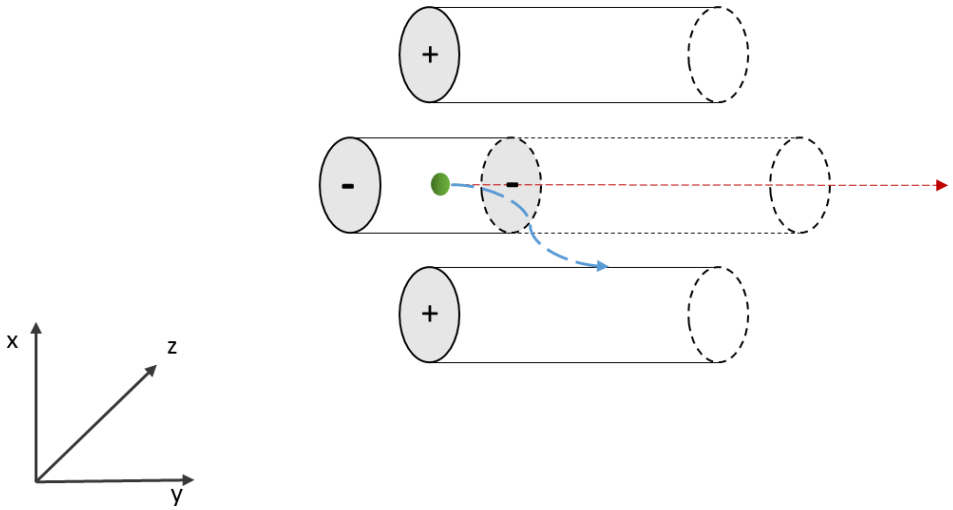

Figure 3.3: Diagram illustrating the mass analyser region of the mass spectrometer. Four circular rods are aligned parallel to each other and a mixture of rf and DC voltages are applied to them. Depending on the current rf and DC settings the ion will either be deflected towards the rods (blue, occurs if it is not the desired mass/charge ratio) or it travels between the rods towards the detector (red, occurs with the selected mass/charge ratio).

3.2.2.3 Ion trajectory through the mass filters

In order to understand how ions move through the mass filter, one must first understand that the QMS operates on two basic principles: firstly, an ion with a higher mass will change direction in an applied field more slowly than a ion with a lower mass, and secondly all ions are subject to the basic laws of electrostatic attraction and repulsion.[6]

As mentioned above, the same potentials are applied to the rods opposite each other, which generates the same charge within each rod. Therefore, there are two sets of rods; one set where the combined DC (U) and RF ($V \cos(\omega t)$) potentials applied to the rods is equal to ($U+ V \cos(\omega t)$),

referred to as the positively charged rods and one set where the combined DC and RF potential applied to the rods is equal to ($-U+V\cos(\omega t)$), referred to as the negatively charged rods (as seen in Figure 3.3)[1,2,6]. The positive and negative rod sets can be referred to as high pass mass filters and low pass mass filters respectively.[6]

The pair of positive rods acting as a high pass mass filter are illustrated in Figure 3.4. Figure 3.4a is a schematic representation of how a low mass and a high mass ion travel through the positive rods.[6] As the ions are also positive, when only a DC potential is applied to the rods, the two ions are repelled by the positive rods and therefore travel straight through the mass filter to the detector. When a RF potential is applied, this causes the potential of the rods to briefly oscillate. The majority of the time the rods remain positive, however, owing to the oscillation of the RF field, the rods will periodically acquire a negative potential. The change in the potential of the rods will affect the trajectory of the ion through the mass filter. The extent of the change in trajectory of the ions depends on the m/z of the ion.[6] As illustrated in Figure 3.4b, when an RF potential is applied, the rods are briefly negatively charged, which attracts the positive ions causing them to change direction and travel towards the rods. As the RF potential oscillates, the rods regain their positive potential and repel the positive ions again. [6] As mentioned above, high mass ions will react more slowly to changes in the electric field than low mass ions. As a result, the high mass ions can travel the length of the filter without being neutralised through impact with the rods. Conversely, the ions with lower masses will react drastically to the change in potential of the rods and change direction abruptly. This will eventually cause them to collide into the rods and become neutralised. The positive rods are referred to as High Pass Mass Filters as only ions above a certain mass can survive the change in charge of the rods from positive to negative, and the subsequent change in trajectory.[6] Ions with lower masses are eliminated, as shown in Figure 3.4c.

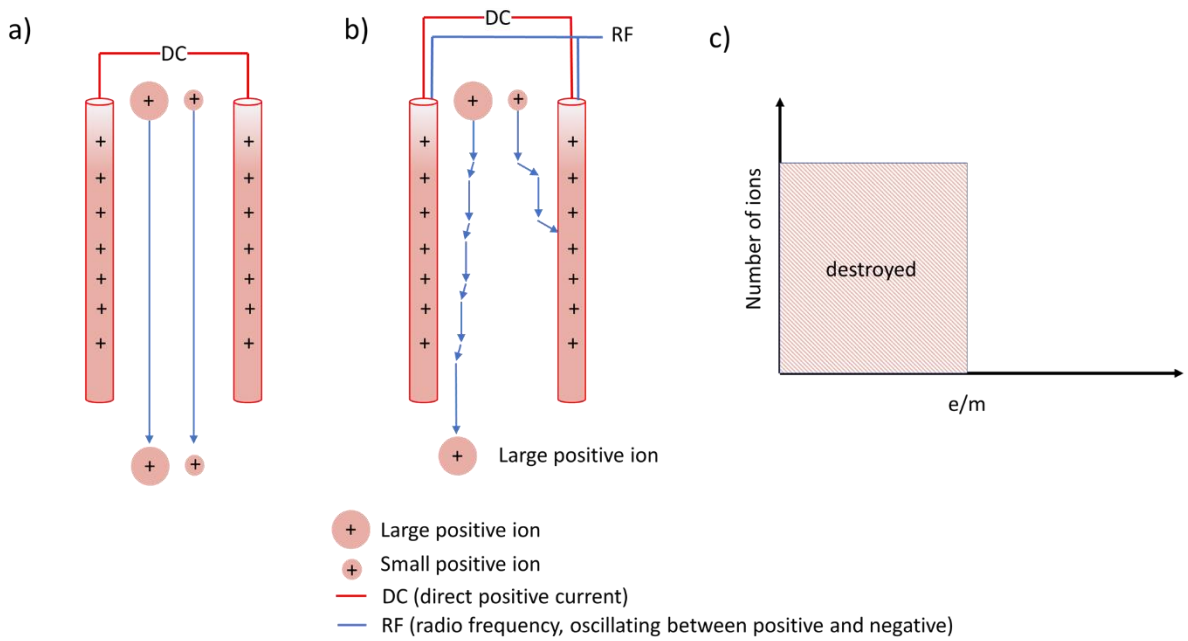

Figure 3.4: Schematic representation of the High Mass Pass Filter of the QMS; a) shows the direction of travel of different sized positive ions through the electric field generated by a stable DC current, b) shows the direction of travel of the same ions through the electric field generated through the superposition of the stable DC current and the alternating RF potential, c) shows that the ions with low mass to charge ratios are destroyed through contact with the rods, and only higher mass ions survive.

The negative rods which act as a low pass mass filter are illustrated in Figure 3.5. When a DC field is applied to these rods, a negative potential is generated. As shown in Figure 3.5a, when only the negative DC potential is applied across the rods, any positively charged ion travelling through the filter is attracted to the rods.[6] The ions will, therefore, travel towards the rods where they will collide with the rods and be destroyed. However, when an RF potential is applied, as mentioned above, this causes an oscillation in the electric field. The oscillation of the RF potential periodically changes the charge of the rods and the electric field. The trajectory of the ions through the mass filter changes to compensate for this change in the electric field. In this case, the rods become positively biased, which will repel the positively charge ions. Higher mass ions are slow to change direction, so will continue their eventual trajectory towards the rods, where they will collide and be destroyed.[6] Conversely, the low mass ions can change direction more quickly, so when the rods oscillate to being positively charged, the ions are quickly repelled in a rapid change of direction. The low mass ions continue to move towards and away from the rods periodically with the oscillation of the RF field until they exit the mass filter, as shown in Figure 3.5b. The negatively

charged set of rods is referred to as the Low Pass Mass Filter as only low mass ions can pass through the filter, whereas high mass ions are destroyed as shown in Figure 3.5c.[6]

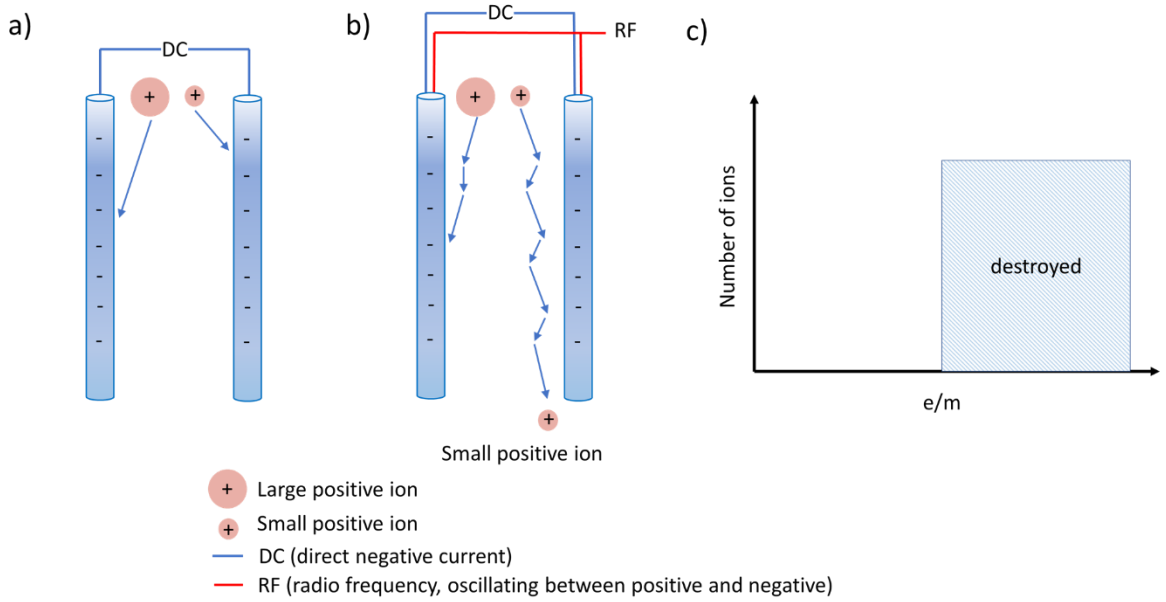

Figure 3.5: Schematic representation of the Low Mass Pass Filter of the QMS; a) shows the direction of travel of different sized positive ions through the electric field generated by a stable DC current, b) shows the direction of travel of the same ions through the electric field generated through the superposition of the stable DC current and the alternating RF potential, c) shows that the ions with high mass to charge ratios are destroyed through contact with the rods, and only lower mass ions survive.

The high pass and low pass mass filters discussed above qualitatively indicate the trajectory of the ions through the electric fields generated by the positive or negative sets of rods. However, in a QMS, both sets of mass filter are present, so one must consider the trajectory through the quadrupole. Due to the overlapping electric fields, ions will travel through the mass filter in a spiral motion, as depicted in Figure 3.6a. [6–8] As shown in Figure 3.6b, the elimination of high mass and low mass ions results in a selectivity within the mass spectrometer for a particular ion with the correct *m/z* ratio.

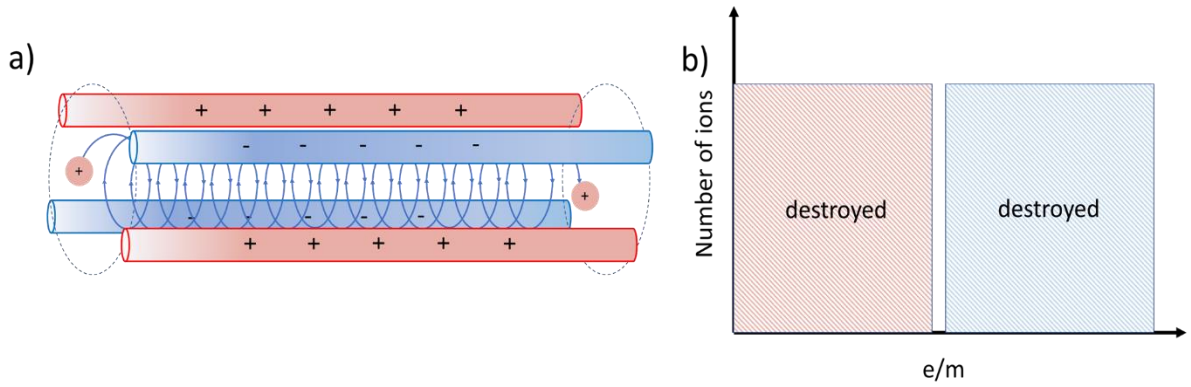

Figure 3.6: a) Diagram showing how an ion travels through the electric fields generated from the high pass and low pass mass filter. Ions are directed in a spiral towards the detector b) Graph showing that as a result of the overlap between the high pass and low pass mass filters, the majority of ions are destroyed. Only ions with certain mass to charge ratios survive.

The selectivity of the mass filters is one of the main advantages of the quadrupole mass spectrometer, as certain masses can be exclusively monitored.[3] The mass to charge ratio of the ion that will reach the detector can be varied, so more masses can be selectively monitored. The simplest way to vary this is to vary the RF regime applied, whilst keeping the DC constant. However, in reality, the masses are normally selected through variation of the DC/RF ratio.[1]

The *X*- and *Y*- motion of the ion within the mass filter can be modelled using the Matheiu equations, which are simply versions of the Newtonian equation of motion, where:

$$Force = ion\ charge \times electric\ field \qquad 3.1$$

Assuming the *X* axis lies along the positively charged rods, and the *Y* axis lies along the negatively charge rods, the motion of an ion with mass (m) and charge, can be described by the equations of motion for three separate axes (equations 3.2-3.4).[1–3,7]

$$\frac{\delta^2 x}{\delta t^2} = -\left(\frac{e}{m}\right)\frac{[U + V\cos(\omega t)]}{r_o^2} \qquad 3.2$$

$$\frac{\delta^2 y}{\delta t^2} = \left(\frac{e}{m}\right)\frac{[U + V\cos(\omega t)]}{r_o^2} \qquad 3.3$$

$$\frac{\delta^2 z}{\delta t^2} = 0 \qquad 3.4$$

where $2r_0$ is the closest distance between the four electrodes of the QMS and e is the magnitude of the electron charge.

3.2.2.4 The Detector

The detector used in the QMS discussed in this thesis is a secondary electron multiplier (SEM), more specifically it is an electron multiplier tube. The electron multiplier tube amplifies the electron signal generated from each ion that reaches the actual detector, using a cascade effect to amplify this signal.[1] A voltage is applied across the detector to sustain the cascade of electrons. When a positive ion reaches the detector, it impacts upon the surface of the detector. The impact generates 2 or 3 electrons, which will in turn go on to collide with the surface and generate the release of more electrons in a cascade effect, as highlighted in Figure 3.7.[1] The signal is finally converted to a digital input which can be easily recorded in the QMS software. The electron multiplier greatly increases the ion signal and allows for high sensitivity to small concentration/ weak ion beams.[5]

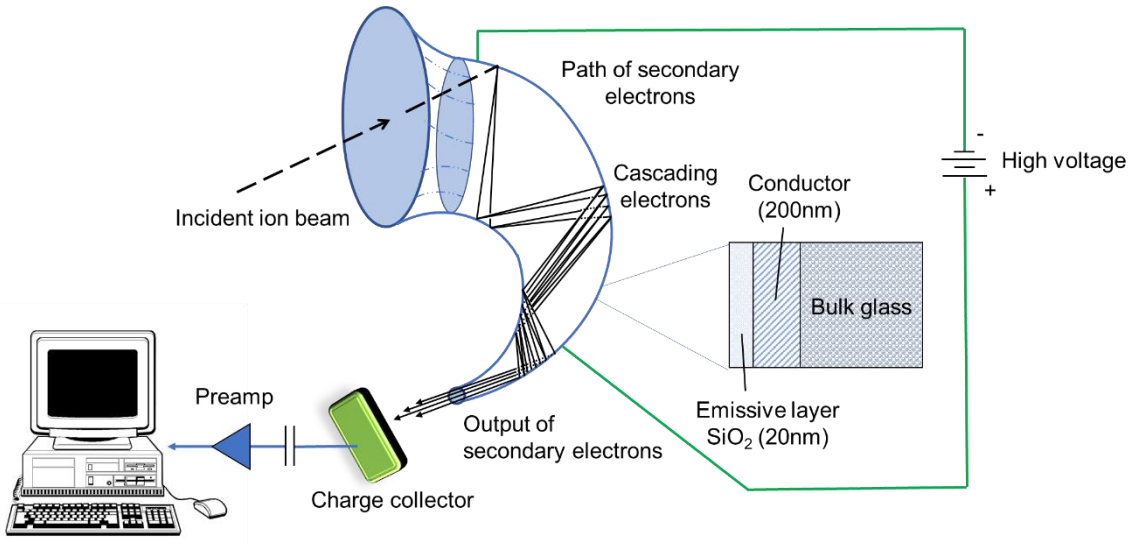

Figure 3.7: Diagram showing how the electron multiplier tube detector works to amplify ion signals. Incident ions impact upon the surface of the tube, causing a cascade of electrons.

3.2.3 Conclusion

In this section, the basics of mass spectrometry were summarised and the Quadrupole Mass Spectrometer was introduced. The various sections of the mass spectrometer were outlined in detail to show how the QMS can be mass selective, allowing for exclusive monitoring of selected masses as they desorb from the astrochemically relevant surfaces studied in this thesis.

3.3 Temperature Programmed Desorption

3.3.1 TPD technique

Desorption was first used as an analytical technique in the 1950's with the introduction of "flash desorption".[9] Flash desorption involves the adsorption of a gas onto a single crystal surface. Rapid or "flash" heating is used to rapidly desorb the adsorbate, and today the technique is most commonly used for surface cleaning. In Temperature Programmed Desorption (TPD) however, a slower and controlled heating rate is used. As explained below, this slow linear heating ramp allows us to gain a greater understanding of what is happening on the surface. As with flash desorption, TPD involves the adsorption of a gas or mixture of gases onto a surface. As the surface is heated the adsorbate desorbs over a specific temperature range and is detected by the QMS, as shown in Figure 3.8a. Specifically, before the gas is dosed onto the sample, the surface must be cooled to a temperature below the desorption temperature of the specific gas. If the temperature of the surface is too high then the gas will not stick/adsorb. When the gas is dosed at a sufficiently low surface temperature it will adsorb on specific binding sites. The surface is then heated slowly, as mentioned above, and the adsorbate will begin to desorb over the specific range of temperatures where the adsorbate gains enough energy to overcome the binding energy.[10,11] TPD is often coupled with mass spectrometry so that the desorbing species can be detected. As the temperature of the surface is varied linearly with time an accurate desorption temperature range for the specific adsorbate is measured. The behaviour of the adsorbate with time and temperature can be analysed through examination of the TPD profile as shown in Figure 3.8b.

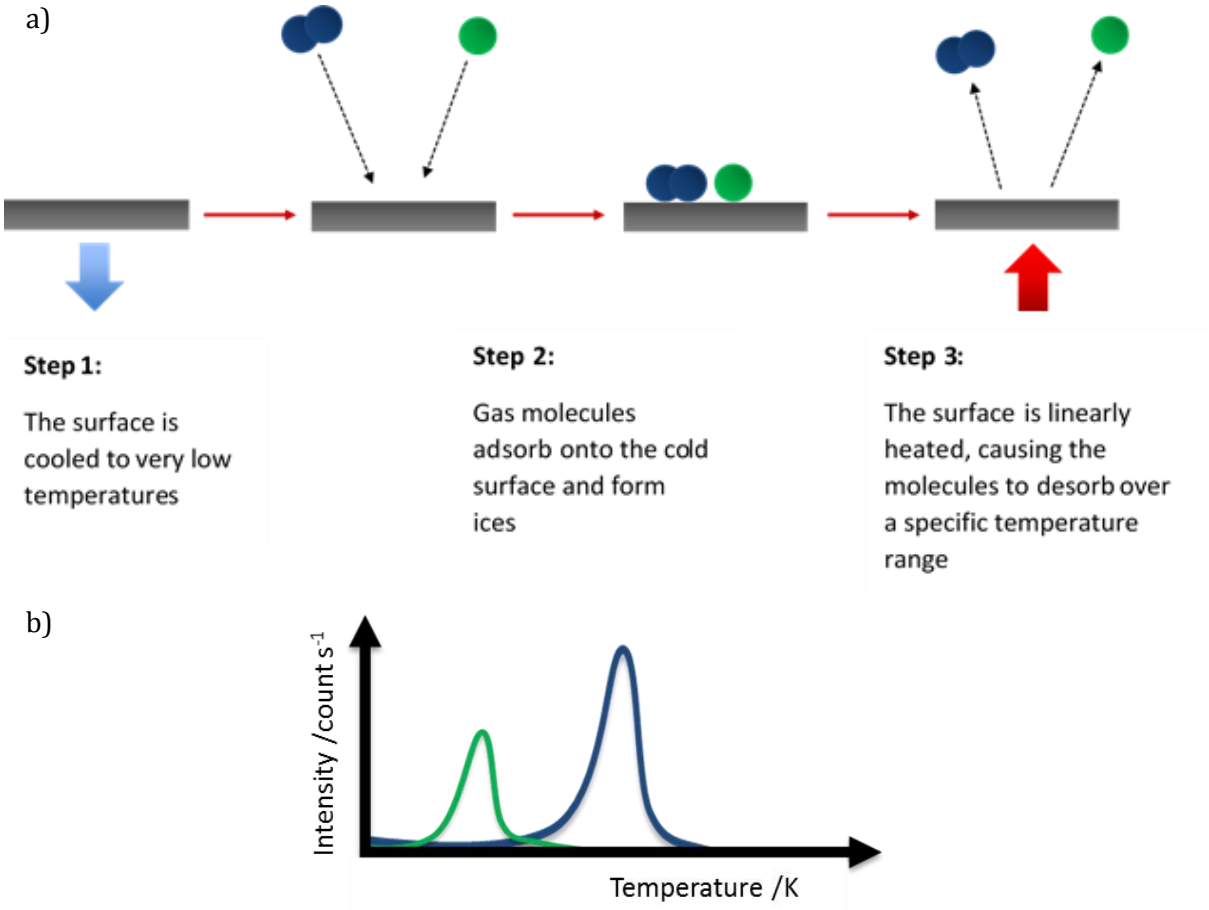

Figure 3.8: a) Schematic illustrating how TPD works, b) an example TPD spectrum showing the number of counts per second at specific temperatures.

As mentioned above, TPD requires the adsorption of gases onto a surface. Adsorption only takes place at so-called "active sites" on the surface, which have specific binding energies. Each surface has a range of binding sites, and molecules or atoms bind to these sites with various different binding energies. TPD can be used to derive information regarding the binding energies of each gas and their desorption kinetics through the application of an Arrhenius law. Specifically, the Polanyi-Wigner equation (3.5) is used to analyse TPD data,[12–15]

$$r_{Des} = -\frac{d\theta}{dt} = v_n \theta^n exp\left[\frac{-E_{Des}}{RT_s}\right] \qquad 3.5$$

where r_{Des} is the rate of desorption, θ is the coverage of the adsorbate on the surface, v is the pre-

exponential factor, n is the order of desorption, E_{Des} is the desorption energy, R is the gas constant and T_s is the surface temperature.

In order to analyse a TPD spectrum, the Polanyi –Wigner equation (3.5) is rigorously applied to the data obtained. In particular, the relationship between the coverage and the surface temperature is analysed through the complete analysis technique as outlined below.[16] In order to fully understand the surface reactions, through the use of equation (3.5), a "family" of spectra are usually recorded. The term "family" corresponds to a number of dosing experiments carried out on the same surface under the same pressure and temperature conditions. The only difference between the experiments in such a "family" is the length of dose. When a whole "family" has been obtained, we should have a number of TPD profiles corresponding to a number of different coverages. The relationship between the spectra of these different coverages can be used to determine values for the order of desorption and the desorption energy, as will be described below.

3.3.2 Desorption Order of the Adsorbates

Further manipulation of the Polanyi- Wigner equation (equation 3.5) can allow for the order of desorption (n) to be calculated, as discussed in detail below. Alternatively, analysis of the shape of a "family" of desorption profiles corresponding to different coverages can provide an estimate of the desorption order.[16,17] In particular, the shapes of the TPD profiles of different doses of a molecule can be compared to give an approximate order of desorption. The typical shapes of desorption profiles for the desorption of adsorbates studied in this thesis, with desorption orders of n = 0 and 1, are outlined in Figure 3.9, which will be discussed in detail below.

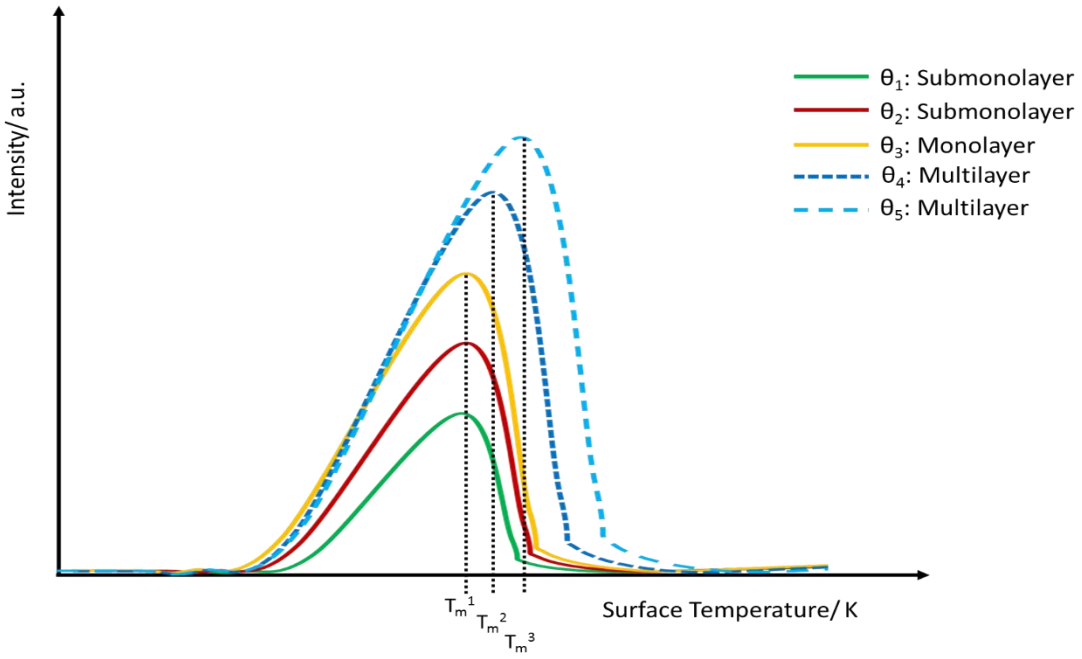

Figure 3.9: Diagram showing the typical shapes of the desorption profiles of a species from the carbonaceous surface. The graphs listed above show that submonolayer and monolayer coverages (green, red and yellow) share the same peak temperature, T_m^1. Multilayer coverages (blue, dashed lines) share the same "leading edge" as the monolayer coverage but the peaks shift to higher temperatures, T_m^2 and T_m^3.

Desorption spectra corresponding to various coverages (θ_1, θ_2, θ_3, θ_4 and θ_5) are shown in Figure 3.9. Through examination of the shapes of TPD profiles corresponding to different coverages we can estimate the dose at which the surface is just completely covered by the adsorbate (a monolayer). As zero and first order kinetics are usually observed for multilayer or monolayer/submonolayer desorption respectively, if with increasing dose we see a shift in the shape of the spectra we can estimate when the monolayer limit is reached. Specifically, when n = 0 the family of spectra are said to share a leading edge (Figure 3.9, blue dashed spectra), or rather desorption occurs at the same initial temperatures but as the coverage increases the peak of the spectra shifts to higher temperatures. The peak temperature refers to the temperature at which the maximum rate of desorption occurs. The peak temperature shifts for zero order desorption because there is more adsorbate on the surface so it takes longer to completely desorb. The typical desorption profiles for a family of different coverages exhibiting first order desorption can also be seen in Figure 3.9. When n = 1 the spectra align in a way where, with increasing coverage, the peak temperature (T_m) remains constant as does the temperature range of the desorption, (Figure 3.9, green, red and yellow spectra). One can determine when the monolayer is complete by examining the shape of the spectra for a family of increasing doses. When the first monolayer is filled, the leading edge of the spectrum will no longer shift to lower temperatures as is seen in first order kinetics but will instead remain the same for any higher doses indicating zero order desorption is taking place from the multilayer.

Examining the shape of a "family" of spectra is a quick way to judge how much of the surface is covered at a given dose. However, for a more accurate value for the desorption order, n, Equation 1 can be manipulated to give a definite value from the experimental data.[13–15] In order to accomplish this derivation, we need to consider the intensity of the signal observed, which is proportional to the rate of change of coverage with time hence,

$$I(T) \propto \ v_n \theta_{rel}^n \, exp\left[\frac{E_{Des}}{RT_s}\right] \qquad 3.6$$

where *I(T)* is the intensity of the TPD trace. With our current set up it is difficult to gain quantitative values for the coverage(θ). In this analysis, the integrated area under the TPD curves provides a value for coverage known as relative coverage (θ_{rel}). To isolate the order (n) from 3.6, logarithms of each side are taken as shown in 3.7.

$$\ln[I(T)] \propto n \ln \ [v_n \theta_{rel}] - \frac{E_{Des}}{RT_s} \qquad 3.7$$

The order of desorption can therefore be obtained by plotting a graph of ln*[I(T)]* against In$[\theta_{rel}]$ at a fixed surface temperature for a variety of coverages. This technique assumes that the pre-exponential factor (v) and the energy of desorption (E_{Des}) are independent of coverage and temperature. This is not always the case. When desorption energy and the pre-exponential factor are dependent on coverage, the corresponding equation derived from the Polanyi-Wigner becomes more complicated. Various second order terms are added that will relate the parameters to the coverage, making it a lot harder to extract useful values.[18] In addition to this, the value for the pre-exponential factor can only be calculated when the absolute coverage is known, which means further experiments would be necessary to calculate this parameter.[19] In general, the assumption that the desorption energy and the pre-exponential factor are independent of coverage is acceptable as previous studies which use the complete analysis technique have shown.[13–15]

3.3.3 Desorption energy of the adsorbates

Further exploitation of the Polanyi-Wigner equation (3.5) can also allow us to obtain a value for the energy of desorption for a particular species.[13–15] Isolation of the desorption energy through further rearrangement of (3.7) is shown in (3.8) and (3.9). From the relationship between coverage, intensity and the surface temperature shown in (3.9) we can derive the desorption energy as shown below.

$$\ln I(T) \propto n \ln v_n + n \ln \theta_{rel} - \frac{E_{Des}}{RT_s} \quad 3.8$$

$$\ln[I(T)] - n \ln \theta_{rel} \propto \ln v_n - \frac{E_{Des}}{RT_s} \quad 3.9$$

A graph of ln*[I(T)]-n* $\ln \theta_{rel}$ against *1/T* will have a gradient of $-E_{Des}/R$, allowing us to calculate the desorption energy. Alternatively, the energy of desorption can be obtained by reading the intensity and temperature at a specific coverage (θ_{rel}') from a family of spectra corresponding to different coverages. As a result of this, the relative coverage is constant in each spectrum and can be ignored, leading to a plot of ln*[I(T)]* against *1/T*, with a gradient of $-E_{Des}/R$.

3.3.4 Conclusion

In this section, the method of analysis of the TPD spectra that will be used in this thesis, was examined. In particular, the complete analysis technique was outlined in detail to show how one could obtain desorption order and energy values for a particular adsorbate from a family of TPD spectra of the same species. This section also showed that analysis of the shape of the desorption spectra relating to different coverages could yield some information into when desorption was taking place from submonolayer, monolayer or multilayer coverages.

3.4 References

1 J. H. Gross, *Mass Spectrometry, A Textbook*, Springer International Publishing AG, Switzerland, Third., 2017, vol. 56.

2 J. T. Watson and O. D. Sparkman, *Introduction to Mass Spectrometry: Instrumentation, Applications and Strategies for Data Interpretation*, John Wiley & Sons Ltd., Chichester, Fourth., 2007.

3 W. M. A. Niessen and D. Falck, in *Analyzing Biomolecular Interactions by Mass Spectrometry*, eds. J. Kool and W. M. A. Niessen, Weinheim, First., 2015, pp. 1–54.

4 R. G. Cooks and R. E. Kaiser, *Acc. Chem. Res. J. Chem. Soc. J. Org. Chem. J. Org.Chem. J. Org. Chem. Pure Appl. Chem*, 1990, **23**, 219–225.

5 Hiden Analytical, Quadrupole Mass Spectrometry Concepts Mass Spectrometers for Residual GasAnalysis,https://www.hidenanalytical.com/wp-content/uploads/2016/08/Mass_spec_concepts_Widescreen.pdf, (accessed 28 January 2019).

6 P. E. Miller and M. B. Denton, *J. Chem. Educ.*, 1986, **63**, 617–622.

7 P. H. Dawson, in *Quadrupole Mass Spectrometry and its Applications*, 1976, pp. 9–64.

8 P. H. Dawson, in *Quadrupole Mass Spectrometry and its Applications*, 1976, pp. 65–78.

9 V. Rakić and L. Damjanović, *Calorimetry and Thermal Methods on Catalysis*, Springer, Berlin, 2013.

10 R. I. Masel, *Principle of Adsoprtion and Reaction on Solid Surfaces*, United States of America, 1996.

11 K. W. Kolasinski, *Surface Science: Foundations of catalysis and nanoscience*, United Kingdom, Third Edit., 2012.

12 J. A. Noble, E. Congiu, F. Dulieu and H. J. Fraser, *Mon. Not. R. Astron. Soc.*, 2012, **421**, 768–779.

13 A. S. Bolina, A. J. Wolff and W. A. Brown, *J. Chem. Phys.*, , DOI:10.1063/1.1839554.

14 A. S. Bolina, A. J. Wolff and W. A. Brown, *J. Phys. Chem. B*, 2005, **109**, 16836–16845.

15 D. J. Burke, A. J. Wolff, J. L. Edridge and W. A. Brown, *J. Chem. Phys.*, 2008, **128**, 0–12.

16 A. M. de Jong and J. W. Niemantsverdriet, *Surf. Sci.*, 1990, **233**, 355–365.

17 M. P. Collings, V. L. Frankland, J. Lasne, D. Marchione, A. Rosu-Finsen and M. R. S. McCoustra, *Mon. Not. R. Astron. Soc.*, 2015, **449**, 1826–1833.

18 J. B. Miller, H. R. Siddiqui, S. M. Gates, J. N. Russell, J. T. Yates, J. C. Tully and M. J. Cardillo, *J. Chem. Phys.*, 1987, **87**, 6725–6732.

19 A. Clemens, L. Hellberg, H. Grönbeck and D. Chakarov, *Phys. Chem. Chem. Phys.*, 2013, **15**, 20456–20462.

Chapter 4. The Reactions of Acrolein with Atomic Oxygen

4.1 Overview

In this chapter the reaction of acrolein with atomic oxygen on a graphite surface under astrochemically relevant conditions will be discussed. The presence of acrolein and oxygen in the ISM will be addressed in detail as will addition reactions previously investigated with this experimental setup. The results of the observed addition reaction will be discussed and modelled to provide a better understanding of the detailed reaction mechanisms taking place between acrolein and oxygen upon the surface of the dust grain analogue.

4.2 Introduction

The interstellar medium is comprised mainly of light elements; 99.9% is hydrogen and helium.[1] Heavier elements such as carbon, oxygen and nitrogen are approximately 4 -5 orders of magnitude less abundant than hydrogen.[2] Despite the relatively low abundance of the heavier elements, and the harsh conditions of the interstellar medium, a rich chemistry takes place within the dense interstellar dust clouds. Over 200 complex molecules have been detected in the ISM to date. Owing to the low pressure and temperature conditions within the interstellar dust clouds, it is unlikely that the abundance of different species can be accounted for by gas-phase chemistry alone.[2] It is, therefore, highly likely that there are reactions taking place upon the surface of the interstellar dust grains, where the gas molecules can bind to the grain surfaces and come together to react. As discussed in previous chapters, it is likely that these surface reactions take place within the dense, cold clouds of the interstellar medium, where the dust grains are shielded from irradiation from surrounding stars by an outer protective layer of gas and dust. The opacity of these dense clouds results in extended molecular lifetimes, allowing more fragile or reactive molecules to survive for longer periods of time. It is possible that many of these molecules are early precursors to biologically relevant species necessary for life.

This chapter will focus on the reaction of atomic oxygen with acrolein. Oxygen is the third most abundant element in the ISM.[1] Molecular oxygen has been detected in multiple interstellar environments, including in molecular clouds such as ρ Ophiuchi A and Orion Molecular Cloud 1.[3] However, oxygen undergoes a “depletion” in the gas-phase, where less molecules are detected in regions than is expected based on the modelling.[4] It is widely believed that the depletion of oxygen can be accounted for if the dust grains are considered as “sinks” for oxygen atoms and if one considers the surface chemistry that takes place upon the dust grains, where it is highly

possible that atomic oxygen will be incorporated into organic species.[1] Studies have been carried out demonstrating the relative reactivity of oxygen on the surface of dust grains. In particular, there have been studies illustrating the hydrogenation of oxygen on such surfaces to form water and ozone, which represents a likely reaction pathway as solid water is one of most abundant interstellar ices detected.[5,6] Previous studies within the Price group at UCL, have investigated the reactions of oxygen atoms with ethene, propene, propyne and CS_2 on graphitic surfaces.[1,2,7] Oxygen atoms were shown to add across the double bonds of the alkenes, with double addition occurring on the alkyne at surface temperatures above 40 K.[1,2] The reactions of atomic oxygen with CS_2 resulted in the production of OCS.[7] At temperatures below 40 K, the addition reactions did not proceed efficiently owing to the competing barrierless formation of ozone from the addition of atomic oxygen to molecular oxygen.[1] Gas phase ozone has been detected towards the IC5146 system, but solid ozone has proven relatively difficult to detect either due to its reactivity on the surface, resulting in a short lifetime, or owing to the detection bias towards silicates, which show an absorption band at 10 μm which can often hide the absorption of ozone at 9.6 μm.[8,9]

Formaldehyde was the first aldehyde to be detected in the interstellar medium.[10] Aldehydes are commonly referred to as the "sugars of space", and since various aldehydes have been detected in the gas phase within molecular clouds, it is believed that the formation of these organic molecules takes place within the ISM.[10,11] Specifically, the formation of the aldehydes is often attributed to simple hydrogen addition reactions upon the surfaces of interstellar dust grains.[11] Propenal, or acrolein is one of the simplest conjugated aldehydes to be detected. In particular, 2 transitions of the trans isomer of acrolein have been observed by the Green Bank Telescope in the star forming region of Sagittarius B2 (N).[10,11] The presence of acrolein in the Sgt B2(N) cloud is thought to be due to hydrogen addition to the well-known interstellar molecule propynal, where it is also possible for further hydrogenation reactions to occur, resulting in the production of propanal.[11]

The presence of acrolein in the ISM is significant because the aldehyde is often regarded as a prebiotic molecule owing to its formation during the decomposition of sugars and its role in the synthesis of amino acids on Earth.[10] Understanding the various reactions of acrolein under interstellar conditions could provide an important insight into the processes that lead to development of life in our universe, as it is possible the molecules necessary for the propagation of life on Earth had interstellar origins. In this chapter, oxygen addition across the conjugated system of acrolein will be investigated.

4.3 Experimental

The experimental apparatus used in this investigation is discussed in detail in Chapter 2. In brief, acrolein and an atomic oxygen/molecular oxygen mixture were co-dosed onto a graphite surface held at specific surfaces temperatures relevant to the low temperatures of the interstellar medium. A reservoir of liquid acrolein was attached to the gas inlet manifold of the Cosmic Dust apparatus and degassed with three freeze-pump-thaw cycles. The liquid acrolein was kept chilled in an ice bath throughout the dosing to ensure a steady flux was obtained for all experiments. Analysis of the spectra indicated a flux of acrolein equal to 2.08 x 10^{-3} ML s^{-1}. Molecular oxygen was also admitted to the gas inlet manifold, and oxygen atoms were produced by passing the oxygen beam through the microwave discharge cell as discussed in Chapter 2. As mentioned in Chapter 2, the dissociation of the O_2 gas resulted in fluxes of 3.98 x 10^{-3} ML s^{-1} and 0.44 x10^{-3} ML s^{-1} for molecular and atomic oxygen respectively, indicative of a dissociation fraction of approximately 10%.

4.4 Results and Discussion

Desorption of Acrolein from Graphite

In this experiment, the reaction of atomic oxygen with acrolein was investigated. As there is little data about the desorption characteristics of acrolein from graphitic surfaces, the desorption spectra of various doses of acrolein from graphite are shown below (Figure 4.1). The parent ion of acrolein, *m/z* 56, was monitored during the TPD.

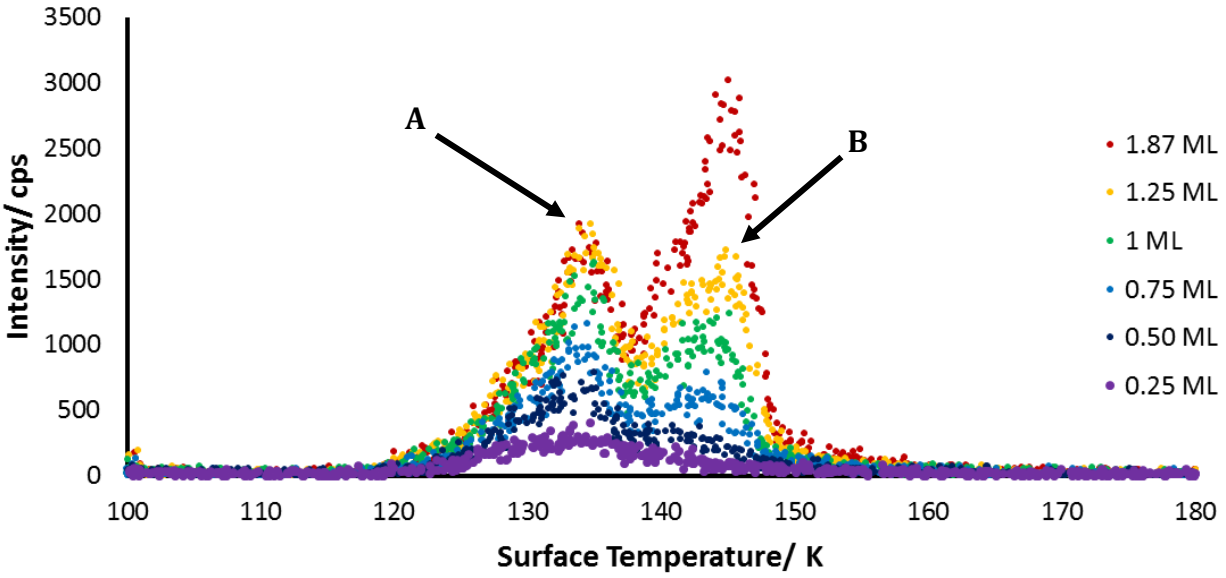

Figure 4.1: Desorption spectra of various doses of acrolein from a graphitic surface held at 110K. Peak A and B are highlighted showing monolayer and multilayer desorption peaks respectively.

As can be seen in Figure 4.1, acrolein shows two desorption peaks, indicating desorption of acrolein is occurring from two different environments. For the lowest dose, Peak A is observed at 134 K, while the second peak, Peak B, is observed at approximately 140 K, although the intensity of this peak in the initial dose (0.25 ML, where 1ML = 2 x 10^{15} molecules) is quite low. As the dose is increased, the intensity of Peaks A and B also increase. Noticeably, the temperature at which Peak A desorbs remains constant, whereas the peak temperature of B shifts to higher temperatures with increasing dose. Both peaks increase in intensity until the 8 minute (1ML) dose, after which we can see that Peak A is saturated. The saturation of Peak A indicates that this lower temperature peak represents desorption of monolayer and sub-monolayer ices. Peak B cannot be saturated and is therefore assigned to the formation of multilayer ices. The formation of both multilayer and monolayer ices at sub monolayer doses, suggests the formation of 3D islands on the surface of the substrate. Island formation occurs when the energy for the adsorbate-adsorbate interaction is greater that the energy of the adsorbate-substrate interaction, so the adsorbate preferentially binds to itself forming ice clusters on the surface of dust grain analogue. Through manipulation of the Polanyi-Wigner equation, as described in Chapter 3, the multilayer desorption energy of acrolein was calculated and a value of 27 ± 0.26 kJ mol^{-1} was obtained. This value is in good agreement with the desorption energy previously calculated for propene ices by Ward et al. (21.45 ± 0.03 kJ mol^{-1}).[2] As the acrolein molecule is heavier, containing an additional oxygen atom, we would expect it to have a higher desorption energy than propene.

Reaction of Acrolein and O atoms on graphite

The reaction of acrolein and atomic oxygen on a graphitic surface was also investigated. The surface was held 22 K while multilayer doses of acrolein (30 min, approximately 4 ML), were co-dosed with atomic and molecular oxygen onto the cold surface. After dosing, the surface was linearly heated, causing the desorption of the molecular ices over a particular temperature range. The desorbing species were monitored by the QMS. After the experiment, the surface was set to a different temperature, ranging from 30-140 K, and the dosing and TPD experiment was repeated. During each TPD, ions with *m/z* 32, 48, 56, and 72 were monitored. Masses at *m/z* 32 and 56 correspond to the parent ions of molecular oxygen and acrolein, whereas the masses at *m/z* 48 and 72, were believed to be possible product peaks. Previous investigations into the reaction of small unsaturated organic molecules revealed that oxygen added across the double bond of the molecules.[1,2] Therefore, the peak at *m/z* 72 corresponds to the mass of the possible product formed through the addition of an O atom to acrolein, $C_3H_4O_2$. Additionally, as molecular oxygen is co-dosed along with the atomic oxygen, the reaction of O atoms with O_2 molecules is expected to occur, as it has previously been investigated and found to proceed barrierlessly. Therefore, the ion at m/z 48 was monitored, to investigate the possible production of ozone.

As a control experiment, O_2 and acrolein were co-dosed in the same way as outlined above. That is, no O atoms were present. This was to confirm that any reactivity observed was as a result of O atom chemistry, and not because of the reaction of acrolein and molecular oxygen.

At surface temperatures below 50 K, no peak was observed at *m/z* 72 but a peak was observed at *m/z* 48, which desorbed at approximately 70 K. For dosing temperatures above 50 K, the opposite was true, where no peak for *m/z* 48 was observed but a peak for *m/z* 72 desorbed between 161 and 183 K. The *m/z* 72 product peak in the TPD is shown in Figure 4.2. Additionally, the *m/z* 72 spectrum for the dosing of acrolein and just molecular oxygen, is also shown in Figure 4.2. No peak was observed for the co-dose of molecular oxygen and acrolein in this temperature range, indicating the peak at *m/z* 72 is solely as a result of the reaction between atomic oxygen and acrolein.

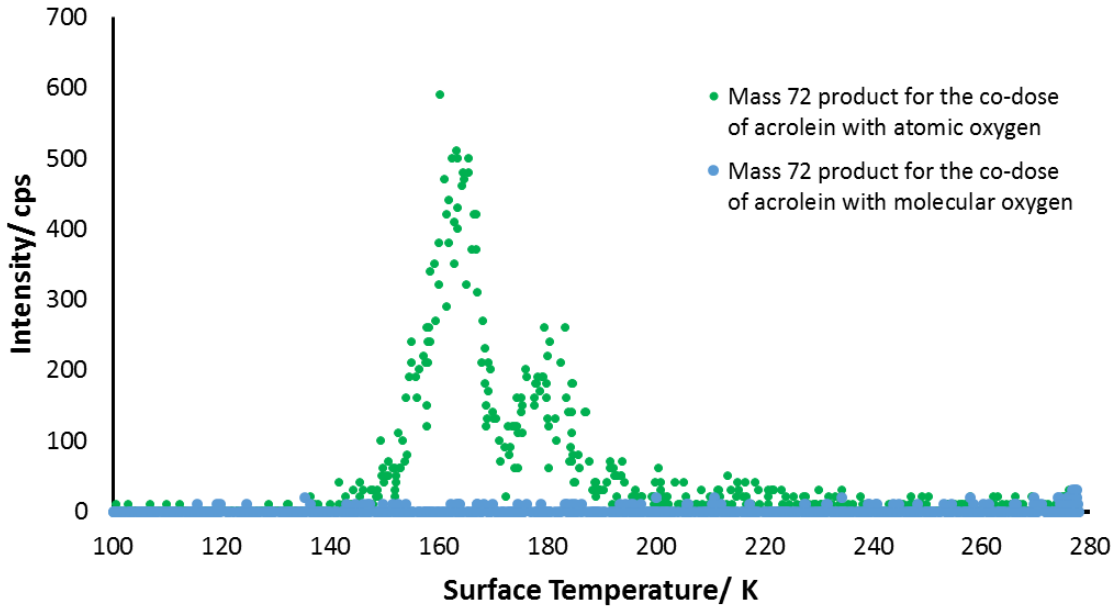

Figure 4.2: TPD spectra of the m/z 72 product for the reaction of atomic oxygen with acrolein (green) and molecular oxygen with acrolein (blue). No product is formed when acrolein is co-dosed with molecular oxygen.

Analysis of the fragmentation patterns of the mass 48 product peak, and the mass 72 product peak enabled us to assign them as ozone and $C_3H_4O_2$ respectively. However, owing to its large number of possible isomers, the exact structure of the $C_3H_4O_2$ product could not be elucidated. Ward et al. examined the addition reactions of atomic oxygen to ethene and confirmed that the major product was ethylene oxide, where the O atom adds across the double bond to form an epoxide ring. They also postulated the formation of propylene oxide for the oxidation of propene. It is therefore possible that the product we observe has a similar structure to what was observed

for addition reactions to smaller alkenes. This possible structure is shown in Figure 4.3, which highlights the two main reactions that are occurring on graphite surface, a) the addition of atomic oxygen to acrolein via the double bond and b) the reaction of oxygen atoms with molecular oxygen.

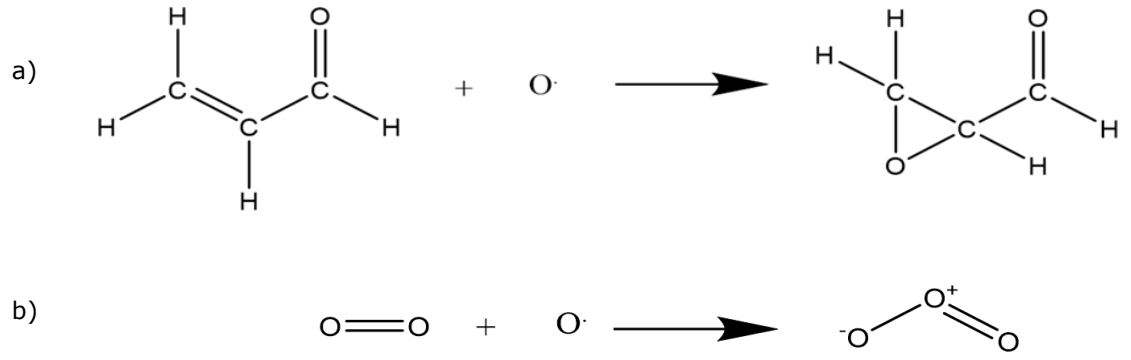

Figure 4.3: Reaction scheme showing the processes taking place on the surface of the dust grain analogue, a) the addition of atomic oxygen across the double bond of acrolein to yield an epoxide and b) the reaction of molecular oxygen with atomic oxygen to yield ozone.

The lack of the m/z 72 product peak at lower surface temperatures indicates the competing reaction, the formation of O_3, (Figure 4.3b) is dominating the chemistry on the surface at these low temperatures. As surface temperature is increased after each experiment, the yield of ozone decreases. This is caused by the desorption of molecular oxygen. All molecular oxygen has desorbed from the surface at temperatures of 50 K so the atomic oxygen is available for reaction with acrolein.

In order to gain a complete understanding of the reactions and interactions that are occurring on the surface, the experiment was modelled, and product yields were compared to the experimental values. However, prior to modelling the data, we extracted absolute values for the yield of O_3 and $C_3H_4O_2$. Owing to the low signal intensity of the ozone peak at m/z 48, the ozone fragmentation peak at *m/z* 32 was used to in data analysis. The yield of each product was obtained through integration of the peaks on the mass spectrum, by calculating the area under the curve. However, in order to ascertain the absolute yield of both products the detection efficiency of the mass spectrometer for each product, had to be taken into account.

To calculate the detection efficiency of the mass spectrometer for ozone, the total ion count of a known dose of molecular oxygen (O_2) was found. As the flux of molecules to the surface is known,

the number of molecules of O_2 on the surface for this dose could be calculated. Therefore, the number of ion counts could be related to the total number of molecules on the surface in order to gain a proportionality constant between ion counts and the number of molecules. The total number of counts of the ozone product was then calculated. As previously mentioned, the O_2 peak at *m/z* 32 was used to calculate the yield of ozone formed on the surface. Therefore, to calculate the detection efficiency of the mass spectrometer for the product, the partial ionisation cross sections of molecular oxygen ($O_2 \rightarrow O_2^+$) and ozone ($O_3 \rightarrow O_3^+$) were compared to get the overall partial ionisation constant of the ozone product for *m/z* 32. After adjusting the number of counts of O_3 observed based upon this new partial ionisation cross section, the ion count was then multiplied by the proportionality constant in order to obtain an absolute yield for ozone formation on the graphite surface.

Calculating the absolute yield of $C_3H_4O_2$ was more complicated. The area under the product peak was calculated to give the general yield, but the partial ionisation cross section of $C_3H_4O_2 \rightarrow C_3H_4O_2^+$ is not yet known. Therefore, a novel approach was employed to calculate the detection efficiency of the mass 72 ion. The equation used to calculate the detection efficiency of the organic product is shown below (4.1)

$$\alpha_{product} = \frac{\alpha_{acrolein}}{\%\ of\ acrolein\ at \frac{m}{z} 56} \times \%\ of\ product\ at \frac{m}{z} 72 \qquad 4.1$$

where α_x refers to the detection efficiency of the desorbing species. The detection efficiency of acrolein was assumed to be the same as the detection efficiency of propyne which was previously calculated in past experiments and models with the group. The mass spectrum of acrolein from the NIST chemical database was used to analyse the percentage of acrolein desorbing from the surface that was actually present at the *m/z* 56 peak. Through examination of the fragmentation pattern of the mass spectrum, it was determined that approximately 8.855% of the acrolein that was dosed on the surface would be accounted for in the desorption spectrum monitoring the peak at *m/z* 56.

As the actual structure of the $C_3H_4O_2$ product was unknown, we needed to generate a full spectrum scan of its structure in order to calculate the percentage of the product detected when m/z 72 was scanned. The mass spectrum for the product was generated by recording a continuous series of mass spectra as the product was desorbing, where the temperature was noted at the beginning of each scan. With this method, we were able to generate a spectrum that

showed how the masses of each ion varied with increasing temperature, and we noted the temperature range that each ion desorbed over. Any peak desorbing over the same range of temperatures as the parent ion was identified as a fragment of the product peak. The acrolein and O experiments were repeated, and during the TPD different fragment product ions were monitored each time. These TPD spectra were then integrated and combined to generate an approximate mass spectrum for the product at m/z 72. Analysis of the fragmentation pattern showed that the percentage of the product that could be measured at m/z 72 was approximately 3.26 %. The combination of these values allowed for the calculation of the detection efficiency of the mass spectrometer for the addition product, thereby enabling the absolute yield of product to be calculated.

The yield obtained from the technique outlined above is only an approximation of the absolute yield of the product as many assumptions need to be taken into consideration. In particular, the assumption that the detection efficiency of acrolein and propyne are the same could be a potential source of error in our calculations and modelling, however propyne and acrolein are similar in size and structure so it is a justifiable assumption. Additionally, the fragmentation pattern of acrolein is used to provide a more accurate estimation of how much acrolein is actually being accounted for for the peak at *m/z* 56. Furthermore, the estimation of the mass spectrum of the product at *m/z* 72 is another source of error, as this mass spectrum is used to estimate the fragmentation of the product within the mass spectrometer. The fragmentation pattern needs to be analysed to account for how much of the product is observed at the molecular ion peak, which is the only peak used to calculate the yield. While these potential errors may affect the overall yield of the product, it would be a continuous error across all temperatures. It should not affect the overall shape of the experimental data, only its intensity. Therefore, the model can still be fitted to the shape of the experimental data to yield results on the kinetics of the reaction on the surface, as will be discussed in detail below.

The Kinetic Model

The experiments discussed in this chapter were modelled using Wolfram Mathematica. The modelling of the results can provide insight into how the reactions are proceeding on the surface of the dust grain analogue and enhance our understanding of how such reactions would take place within the ISM. The model used in this study was developed from similar kinetic models used by Ward et al. and Kimber et al. to investigate the reactivity of adsorbates on surfaces. [1,2,7]

In general, any surface reaction can proceed through two prototypical mechanisms: the Langmuir-Hinshelwood (LH) mechanism and the Eley-Rideal (ER) mechanism. The LH mechanism is a diffusive process. When a gas species is adsorbed onto the surface at a binding site, it is thermalized. The weak binding of the adsorbed species to the surface results in the

diffusion of light species between the binding sites on the surface by overcoming a diffusive barrier or via tunnelling, until they find a reactive partner, as outlined below in Figure 4.5. When the adsorbates react together, one of two things can occur. Firstly, the molecule can desorb using the energy associated with its formation to overcome its binding energy in a process known as chemical desorption. Or the newly formed molecule can remain on the surface until the surface is heated, after which the molecule will desorb (usually via thermal desorption or photodesorption) as shown in expression 4.2. The rate of the Langmuir-Hinshelwood mechanism is dependent upon the rate coefficient (k_{LH}) and the surface concentrations of the two reacting species.

$$X_{(ads)} + Y_{(ads)} \rightarrow XY_{(ads)} \qquad 4.2$$

By contrast, the Eley-Rideal (ER) mechanism does not involve diffusion but instead describes a pathway *via* which the incoming gas species will "hit" an adsorbate directly causing a reaction (4.3). The ER pathway occurs before the incoming gas species can equilibrate with the surface. The rate of the ER mechanism is therefore dependent upon the rate coefficient (k_{ER}) as well as the concentration of the adsorbed species and the flux of the incoming gas.

$$X_{(g)} + Y_{(ads)} \rightarrow XY_{(ads)} \qquad 4.3$$

The third possible reaction pathway that could take place upon the graphite surface is the hot atom mechanism. This mechanism occurs when an incoming gas phase species is only partially thermalized with the surface upon adsorption, meaning the reactant can diffuse across the surface before meeting a reaction partner. This process is not addressed in the current model as it would require quantification of the rate of thermalization of the species with the surface, which is difficult to distinguish. The inclusion of hot atom chemistry within the model is therefore not currently practical as it would introduce too many parameters for a meaningful fit to be obtained.

Our model will focus on the Langmuir-Hinshelwood and Eley-Rideal processes taking place upon the graphite surface, outlined in Figure 4.4. Both the LH and ER processes are thought to occur to a certain degree on all the grain surfaces; where the degree to which each process occurs varies with surface composition, surface conditions and the gas that is involved. The model allows for both Eley-Rideal and Langmuir-Hinshelwood processes to occur simultaneously on the surface. In understanding how a certain gas interacts with a certain surface under conditions that are mimicking the environments in the dense clouds, we can better understand how reactions with that same gas will occur on a similar surface in the ISM.

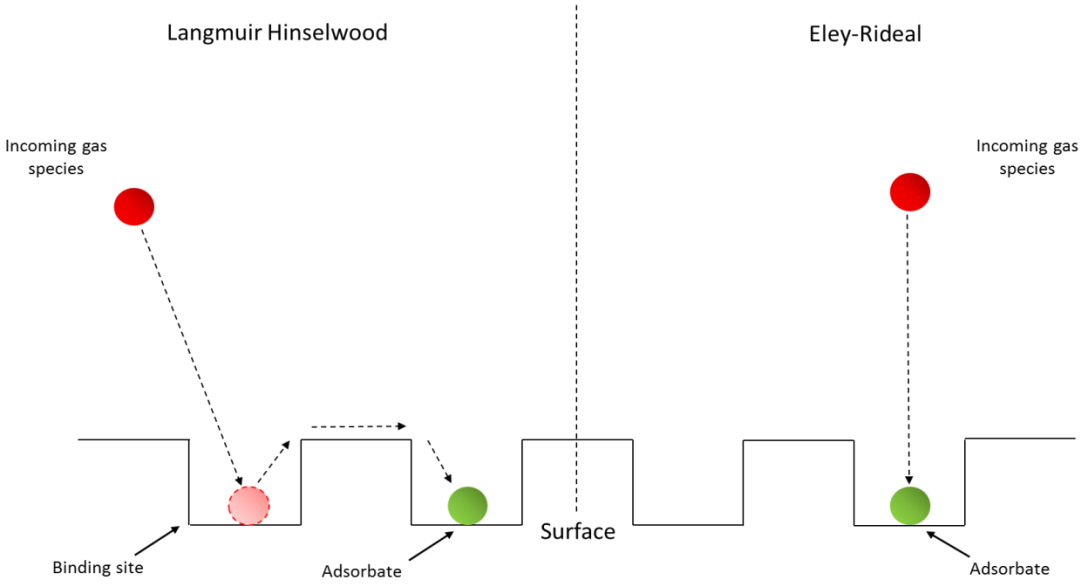

Figure 4.4: Schematic representation of the Langmuir-Hinshelwood (left) and Eley-Rideal (right) surface mechanisms. The LH mechanism shows an incoming gas species binding to the empty binding site on the surface then diffusing to the next binding site to react with the adsorbate. The ER mechanism shows the incoming gas, coming in directly on top of the adsorbate to react.

For the reaction of acrolein with atomic oxygen, the LH and ER mechanisms proceed as shown in 4.4-4.6.

$$C_3H_4O_{(ads)} + O_{(ads)} \rightarrow C_3H_4O_{2(ads)} \qquad 4.4$$

$$C_3H_4O_{(ads)} + O_{(g)} \rightarrow C_3H_4O_{2(ads)} \qquad 4.5$$

$$C_3H_4O_{(g)} + O_{(ads)} \rightarrow C_3H_4O_{2(ads)} \qquad 4.6$$

There are two possible pathways for the ER mechanism to take, as either of the reactants could act as the adsorbate or the incoming gas molecule during the reaction. From the equations above the rates of the LH and ER mechanisms for the reaction of acrolein and atomic oxygen on the graphite substrate can be expressed as:

$$r_{LH} = k_{Diff}\, k_{LH}[C_3H_4O_{(ads)}][O_{(ads)}] \qquad 4.7$$

$$r_{ER1} = k_{ER1}[C_3H_4O_{(ads)}]F_O \quad 4.8$$

$$r_{ER2} = k_{ER2}[O_{(ads)}]F_{C3H4O} \quad 4.9$$

where r_i is the rate of the reaction, k_i refers to the rate coefficient of that reaction, F_y is the flux of the incoming gas species and *[X]* refers to the concentration of the adsorbates in molecules cm^{-2}. In Equation 4.7, k_{Diff}, refers to the diffusion rate coefficient. As acrolein and molecular oxygen are too heavy to diffuse efficiently across the graphite surface upon adsorption, at these low temperatures only the diffusion coefficient for atomic oxygen need be considered. The diffusion coefficient (k_{Diff}) for the diffusion of O atoms on our surface was derived from the empirical diffusion coefficient outlined by Minissale *et al*., who used the coefficient to successfully account for the yield of ozone they observed in their study (4.10).[3]

$$k_{Diff} = k_0 (1 + T^3/T_0^3) \quad 4.4.10$$

Where k_0 is 0.9 and T_0 is 10 K.

In order to accurately model the reactions taking place on the surface we must also consider the mechanisms through which the competing reaction between atomic and molecular oxygen proceeds. The LH and ER mechanisms for the reaction of atomic oxygen with molecular oxygen are described in Equations 4.4.11, and 4.4.12 - 4.4.13 respectively.

$$O_{2\,(ads)} + O_{(ads)} \rightarrow O_{3(ads)} \quad 4.11$$

$$O_{2\,(ads)} + O_{(g)} \rightarrow O_{3(ads)} \quad 4.12$$

$$O_{2\,(g)} + O_{(ads)} \rightarrow O_{3(ads)} \quad 4.13$$

The rate equations for the reaction between atomic oxygen and molecular oxygen on the graphite surface as expressed as such:

$$r_{LH2} = k_{Diff}\, k_{LH2}[O_{2(ads)}][O_{(ads)}] \quad 4.14$$

$$r_{ER3} = k_{ER3}[O_{2(ads)}]F_O \quad 4.15$$

$$r_{ER4} = k_{ER4}[O_{(ads)}]F_{O2} \quad 4.16$$

where r_i is the rate of the reaction, k_i refers to the rate coefficient of that reaction, F_y is the flux of the incoming gas species and *[X]* refers to the concentration of the adsorbates in molecules cm^{-2}.

Furthermore, the LH and ER mechanism for the reaction between oxygen atoms on the surface to produce molecular oxygen must also be taken into consideration (4.17-4.18)

$$O_{(ads)} + O_{(ads)} \rightarrow O_{2(ads)} \quad 4.17$$

$$O_{(g)} + O_{(ads)} \rightarrow O_{2(ads)} \quad 4.18$$

The rate equations for the reactions of 2 atoms of oxygen on the graphite surface are outlined in Equation (4.19 and 4.20).

$$r_{LH3} = k_{Diff}\, k_{LH3}[O_{(ads)}][O_{(ads)}] \quad 4.19$$

$$r_{ER5} = k_{ER5}[O_{(ads)}]F_O \quad 4.20$$

where r_i is the rate of the reaction, k_i refers to the rate coefficient of that reaction, F_y is the flux of the incoming gas species and *[X]* refers to the concentration of the adsorbates in molecules cm^{-2}.

The variation of the rate coefficient of the rate equations (k_i) can be described by an Arrhenius type expression,

$$k_i = A_i\, exp(-E_i/RT) \quad 4.21$$

where *i* refers to a particular pathway (for example, k_{LH} or k_{ER1}), A_i describes the pre-exponential factor of that pathway and E_i is the activation energy of that pathway.

In order to simplify the model, and reduce the number of free parameters, certain assumptions have been made. In particular, for the reactions of acrolein and atomic oxygen (4.7-4.9), the pre-exponential factors (A_{LH} and A_{ER1}, A_{ER2}) are assumed to be the same. Additionally, as previous studies have shown that the reaction between atomic oxygen and molecular oxygen, as well as 2 atoms of oxygen are barrierless, the activation energy of the reactions is assumed to be zero.

As previously mentioned above, LH and ER mechanisms can occur simultaneously on the surface. Therefore, in order to describe the overall rate of formation for any of the products, we can

combine the rate equations, as shown below for the rate of formation of $C_3H_4O_2$ (4.22), O_3 (4.23) and O_2 (4.24) respectively.

$$r_{C3H4O2} = k_{Diff}\, k_{LH}\left[C_3H_4O_{(ads)}\right]\left[O_{(ads)}\right] + k_{ER1}\left[C_3H_4O_{(ads)}\right] F_O + k_{ER2}\left[O_{ads}\right] F_{C3H4O} \quad 4.22$$

$$r_{O3} = k_{Diff}\, k_{LH2}\left[O_{2(ads)}\right]\left[O_{(ads)}\right] + k_{ER3}\left[O_{2(ads)}\right] F_O + k_{ER4}\left[O_{ads}\right] F_{O2} \quad 4.23$$

$$r_{O2} = k_{Diff}\, k_{LH3}\left[O_{(ads)}\right]\left[O_{(ads)}\right] + 2(k_{ER5}\left[O_{(ads)}\right] F_O) \quad 4.24$$

As can be deduced from the rate equations for the formation of each of the products, that the reaction rate is dependent upon the surface concentration of the reactants. Therefore, the rate of change of the surface concentration of the reactants needs to be taken into consideration. By combining the processes occurring in r_{C3H4O2}, r_{O3} and r_{O2}, along with other surface characteristics, that will be described in greater detail below, we can describe the factors that are affecting the surface concentration of the reactants.

$$\frac{d\,[C_3H_4O]}{dt} = F_{Acrolein} - r_{C3H4O2} - r_{Des,acrolein} \quad 4.25$$

$$\frac{d\,[O]}{dt} = F_O - r_{C3H4O2} - r_{O3} - r_{O2} - r_{Des,O} \quad 4.26$$

$$\frac{d\,[O_2]}{dt} = F_{O2} - r_{O3} + r_{O2} - r_{Des,O2} \quad 4.27$$

where F_j refers to the flux of the reactant (j) to the surface, r_i refers to the rate equations for the formation of the products (i) (described above in equations 4.22 - 4.24) and $r_{Des,\,j}$ is the rate of desorption of the reactant (j) from the surface.

The rate of desorption of the reactants is dependent upon the surface temperature and so the rate of desorption can be described through a second Arrhenius expression.

$$r_{Des,j} = A_{Des,j}\, exp\left(-E_{Des,j}/RT\right) \quad 4.28$$

where $A_{Des,j}$ is the preexponential factor for the desorption of the reactant and $E_{Des,j}$ refers to the desorption energy of the reactant. In our model, a standard pre-exponential factor for the desorption of the reactants was assigned as 1×10^{12} s^{-1}, which is a standard value.

To determine the yield of the products, the rate equations (4.25 - 4.27) were integrated with respect to deposition time. The rate equations were integrated numerically, from initial conditions, where the concentration of the reactants on the surface ([O], [C3H4O] and [O2]) is zero at t=0.

In our model, we do not consider the desorption energy of the products as they do not desorb during the dosing period of the experiment. This is in agreement with Kimber et al. who investigated the reaction of propyne with atomic oxygen. The desorption energy of the products were set to higher energies of desorption as the products were heavier and more polar. Concurrently, our products are similar more polar and heavier, and therefore the model assumes they do not desorb during the dosing part of the experiment (with the exception of O_2, which also acts as a reactant).

The model yields of the $C_3H_4O_2$ product and O_3 product are shown in Figure 4.5a & 4.5b. In these figures, the dependence of the yield of each product upon LH and ER mechanisms is also modelled. The data was fitted to the experimental value through variation of the desorption energies of the reactants and the activation energies for k_{LH}, k_{ER1} and k_{ER2}. The average absolute experimental values for the yield of $C_3H_4O_2$ and O_3 are also visible in Figure 4.5a & 4.5b. The reaction between acrolein and atomic oxygen was conducted three times at each surface temperature. The absolute yields of the products were calculated for each set of experiments and then averaged at each temperature. The error bars in Figure 4.5a and 4.5b represent the standard deviation of the calculated yield at each temperature.

The plot in Figure 4.5a highlights that formation of the organic product, $C_3H_4O_2$, does not occur until temperatures greater that 40 K. This is in agreement with what we observed experimentally. Examination of Figure 4.5b indicates that at temperatures below 40 K, atomic oxygen is reacting with molecular oxygen to form ozone. Above temperatures of 40 K, the molecular oxygen has desorbed from the surface so it is no longer able to react with the oxygen atoms.

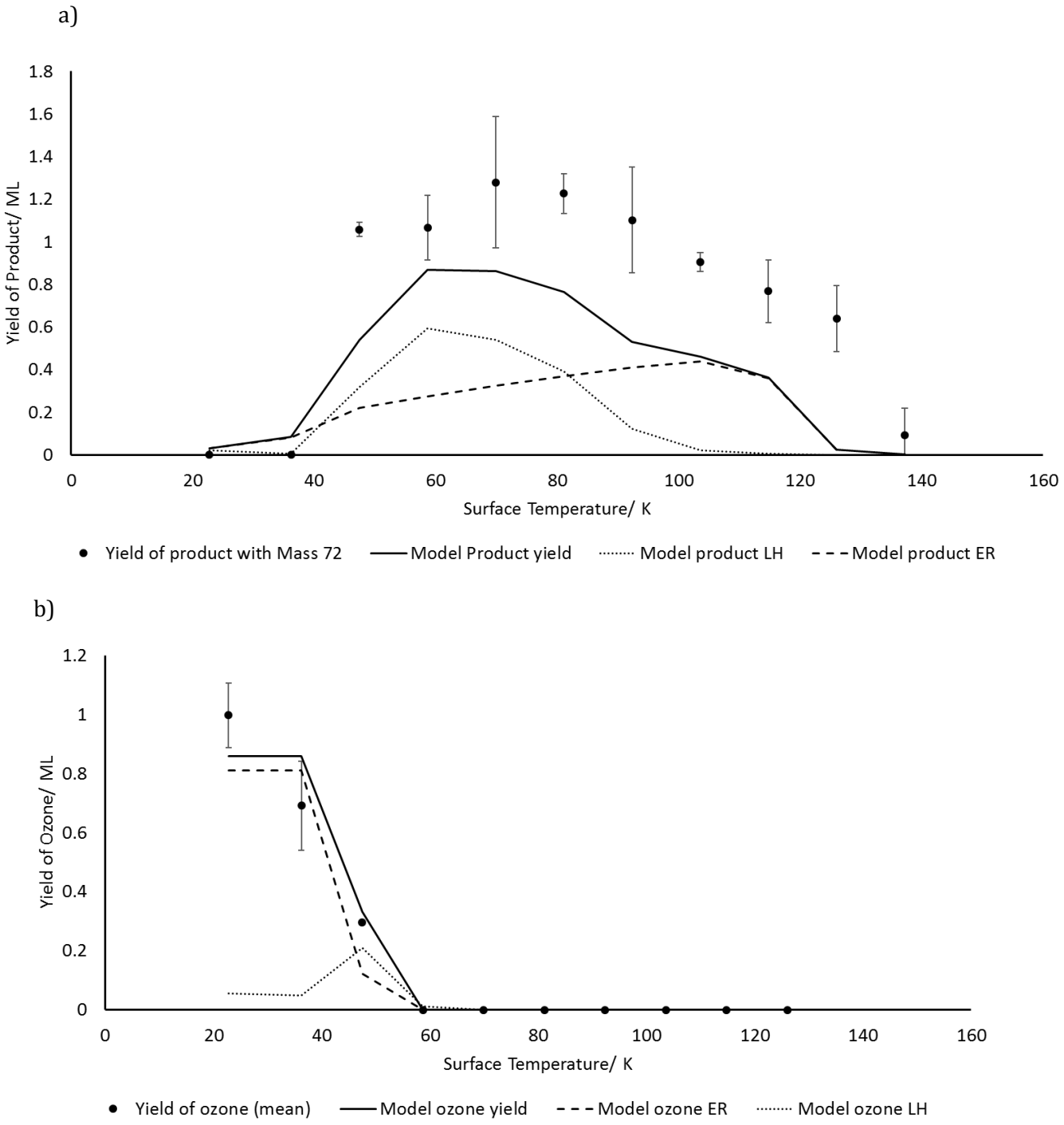

Figure 4.5: Average yield of a) the organic product m/z 72, and b) ozone at different surface temperatures. The experimental data and modelled data are compared and the LH and ER contributions to each yield are outlined in each graph.

In Figure 4.5b, we can see that the experimental data and the fitted data are in excellent agreement with each other. The formation of ozone occurs preferentially on the surface via the ER mechanism at these low temperatures. This is to be expected as the O atoms likely do not possess enough energy to overcome the diffusion barrier to move across the surface at such low temperatures. However, as the surface temperature increases, so too does the extent of the Langmuir-Hinshelwood mechanism, as at warmer surface temperatures the O atoms have enough energy to become mobile across the surface. As mentioned above, the yield of ozone decreases with increasing surface temperature as the oxygen begins to desorb from the surface. The energy extracted for the desorption energy of oxygen was 10.4 kJ mol^{-1}, which is in good agreement with the value observed previously within the group.[1]

Comparison between the fitted data and the experimental data in Figure 4.5a, show that the general shape of the fit is good, however the yield of product falls short of the yield achieved experimentally. Figure 4.6 shows the experimental data compared to the fitted $C_3H_4O_2$ yield, which has been normalised by a factor of approximately 1.5. From this fit we can see that both Langmuir Hinshelwood and Eley-Rideal mechanism are taking place on the surface for the reaction between atomic oxygen and acrolein. At lower surface temperatures (> 40 K) the LH mechanism dominates, increasing to a maximum at approximately 60 K. At temperatures above 60 K, the extent to which the LH mechanism occurs on the surface begins to fall, while the ER mechanism increases steadily. The drop in the reaction proceeding via the LH mechanism at temperatures great than 60 K can be attributed to the desorption of atomic oxygen. The desorption energy of O atoms was extracted from the model and found to be 15.7 kJ mol^{-1}, in excellent agreement with the energy extracted by Kimber *et al.*[1]

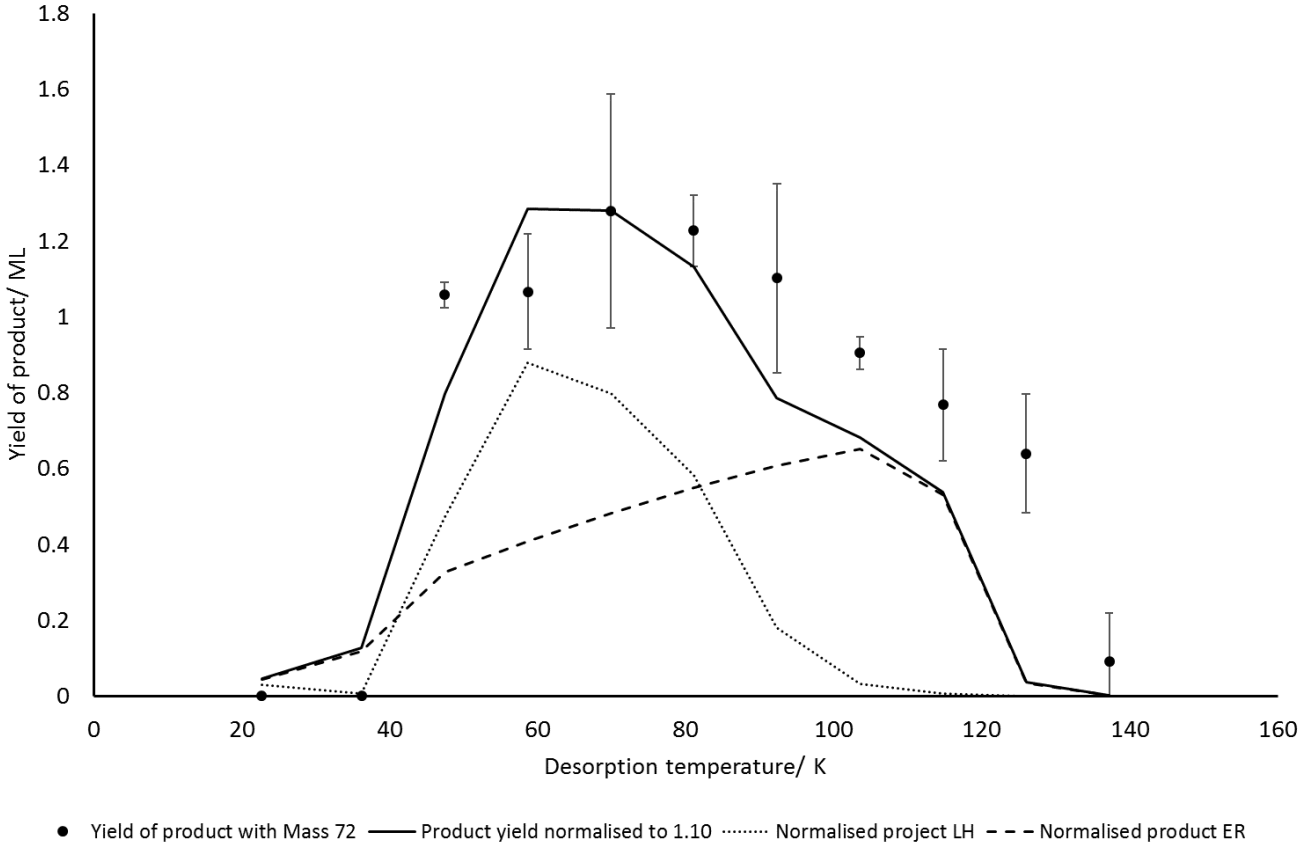

Figure 4.6: Plot showing the average experimental yield of the organic product m/z 72, $C_3H_4O_2$ and the fitted data for the yield of product from the model (normalised by approximately 1.5).

The difference between the fitted data and the experimental data could be due to a number of reasons. A difference in flux could be used to account for the difference, however the experimental values for the flux were used in the model so this is unlikely as the cause. As the difference between the observed and modelled data is greatest at higher temperatures, the modelled desorption energy of acrolein might be underestimated. However, the desorption energy for acrolein extracted from the model was found to be 28.1 kJ mol^{-1}, in excellent agreement with the experimental values obtained (27 ± 0.26 kJ mol^{-1}). As mentioned, many assumptions were made when writing the model. For example, the pre-exponential factor for the desorption of acrolein and oxygen are assumed to be the same. Given the vast difference in structure, this is perhaps unlikely to be the case. Furthermore, the assumption that the pre exponential factors for the rate of LH and ER mechanisms are the same, may affect the shape of the spectra. However, owing to the fact that the modelled values for the yield of $C_3H_4O_2$ is too low across the entire temperature range, the most likely source of error is actually in the conversion of the experimental yields into absolute yields. The estimation of the detection efficiency of the mass spectrometer for the

product may be less than ideal as discussed above, resulting in an overestimation of the absolute yield as observed in Figure 4.6. The error caused by the assumptions previously discussed, namely with the estimation of the fragmentation pattern of the product and the calculation of the overall detection efficiency cannot be quantified, but as mentioned, it should have little effect on the shape of the yield plots shown above. Therefore, the kinetic parameters extracted from the model, including the information about the LH and ER mechanisms of the reaction at different temperatures, can be considered valid.

In summary, the model indicates that the addition reaction of O across the unsaturated bond in acrolein is a possible reaction pathway above surface temperatures of 40 K. Whilst the model may not be entirely accurate at higher temperatures, is does confirm that the addition reaction is a viable process that could occur in the interstellar medium. The actual yield of the product observed in the ISM would be much less, owing to the low flux of the reactants within the interstellar dust clouds evidenced through the low pressures and column densities observed. Furthermore, the oxygen incorporation into the organic species, as well as the formation of ozone at lower temperatures could help account for the depletion of oxygen observed along many lines of sight in the interstellar medium, as the oxygen is being used in the formation of more complex chemical species.

4.5 Conclusion

In this chapter, the reactivity of an unsaturated aldehyde with atomic oxygen under interstellar conditions was investigated. Addition of atomic oxygen across the double bond in acrolein was observed at surface temperature higher than 40 K, consistent with results observed previously with the addition reaction involving O atoms and unsaturated species. The reaction was successfully modelled to indicate the degree of ER and LH mechanisms taking place at these surface temperatures, and relatively good agreement was observed between the experimental and modelled data for the desorption of acrolein and atomic and molecular oxygen.

4.6 References

1 H. J. Kimber, C. P. Ennis and S. D. Price, *Faraday Discuss.*, 2014, **168**, 167–184.

2 M. D. Ward and S. D. Price, *Astrophys. J.*

3 M. Minissale, E. Congiu and F. Dulieu, *J. Chem. Phys.*, , DOI:10.1063/1.4864657.

4 S. Wang, A. Li and B. W. Jiang, *Mon. Not. R. Astron. Soc.*, 2015, **454**, 569–575.

5 S. Ioppolo, H. M. Cuppen, C. Romanzin, E. F. van Dishoeck and H. Linnartz, *Astrophys. J.*, 2008, **686**, 1474.

6 H. M. Cuppen, S. Ioppolo, C. Romanzin and H. Linnartz, *Phys. Chem. Chem. Phys.*, 2010, **12**, 12077–12088.

7 M. D. Ward, I. A. Hogg and S. D. Price, *Mon. Not. R. Astron. Soc.*, 2012, **425**, 1264–1269.

8 J. E. Chiar, Y. J. Pendleton, L. J. Allamandola, A. C. A. Boogert, K. Ennico, T. P. Greene, T. R. Geballe, J. V. Keane, C. J. Lada, R. E. Mason, T. L. Roellig, S. A. Sandford, A. G. G. M. Tielens, M. W. Werner, D. C. B. Whittet, L. Decin and K. Eriksson, *Astrophys. J.*, , DOI:10.1088/0004-637X/731/1/9.

9 H. Mokrane, H. Chaabouni, M. Accolla, E. Congiu, F. Dulieu, M. Chehrouri and J. L. Lemaire, *Astrophys. J.*, 2009, **705**, 1–16.

10 A. M. Daly, C. Bermúdez, L. Kolesniková and J. L. Alonso, *Astrophys. Journal, Suppl. Ser.*, 2015, **218**, 30.

11 J. M. Hollis, P. R. Jewell, F. J. Lovas, A. Remijan and H. Møllendal, *Astrophys. J.*, 2004, **610**, L21–L24.

Chapter 5: Desorption of Small Astrochemically Relevant Molecules from a Graphitic Surface

5.1 Overview

In this chapter, the desorption of small astrochemically relevant species from graphite will be investigated. The gases will be introduced individually before the particular desorption characteristics of each gas is discussed. Additionally, kinetic parameters will be calculated from the desorption spectra, where possible. The aim of this chapter is to validate the TPD methodology through comparison of the desorption characteristics observed experimentally with previous work.

5.2 Introduction

In the dense cores of interstellar dust clouds, the temperature of the gas and dust grains in approximately 10 K. At these low temperatures, the gases will "freeze-out" onto the surfaces of the grains forming icy mantles. These ices enable gases to interact together and allow a rich chemistry to take place on the grain surfaces. The chemistry taking place within these dense cores is of particular interest owing to the fact that the dense cores are shielded from the destructive photoionization processes observed in diffuse interstellar clouds; this allows for the formation of more complex molecules, as discussed in Chapter 1. In order to fully understand the processes occurring within the dense cores of the ISM, it is important to first comprehend what effect the underlying surface could have on the desorption and interaction of key interstellar molecules. Analysis of mass spectra obtained after temperature programmed desorption experiments involving gases adsorbed to interstellar dust grain analogues can help to illuminate adsorbate-substrate interactions and can also allow for the determination of kinetic data characterising the desorption of each molecule. The kinetic data obtained from such experiments can then be incorporated into astrophysical models which will simulate the desorption of molecular ices from surfaces under more interstellar relevant time scales. The desorption characteristics of a number of different molecules have been examined in the course of this research. In this chapter, the desorption of ammonia, methanol, carbon monoxide and carbon dioxide from graphite will be outlined. The desorption of oxygen, acrolein and propene will be discussed in other Chapters.

5.2.1 Ammonia

Ammonia (NH_3) is an important molecule within the ISM as a carrier of nitrogen and is often involved in nitrogen related chemistry.[1] Hagen modelled the icy mantles on dust grains and concluded that the majority of atomic nitrogen present in the ISM is quickly abstracted by hydrogen into ammonia.[2] Ammonia has also been identified as a vital prebiotic molecule.[3] Specifically, ammonia has been linked to the formation of the nucleobases adenine and guanine within molecular ices, suggesting that life on Earth could have interstellar origins.[4] It is therefore important that we understand how ammonia interacts with the grain surfaces within the cold, dense regions of the ISM. Terrestrially, ammonia is a well-known substance within the chemicals industry. As a result, there have been many studies into the adsorption of ammonia onto metallic surfaces, such as Au (111), Al(111) and Ag(111). [1] Ammonia acts as a weak donor ligand on metallic surfaces, chemisorbing to the metal through the donation of a lone pair of electrons. However, multilayer desorption of ammonia has also been observed from these metallic surfaces, with a desorption peak of approximately 110 K.[1]

Ammonia has been observed in a variety of stellar and interstellar environments. Radio observations of ammonia are often used to identify properties within dense molecular clouds as it constitutes a relatively high percentage of interstellar molecular ices with 5-30 % abundance relative to the most abundant molecular ice, water.[1,5] For example, ammonia ice has been detected in the dark cloud L134N with a column density of approximately 1×10^{-7} relative to molecular hydrogen.[6] Interestingly, ammonia is also an active participant in interstellar acid and base reactions, specifically the reaction with methanol (5.1) as studied by Bergner et al. [5]

$$NH_3 + HCOOH \rightarrow NH_4^+ + HCOO^- \qquad 5.1$$

Bolina and Brown investigated the desorption of ammonia from HOPG surfaces at 90 K.[1] Previous studies into the desorption of ammonia from a gold surface under interstellar conditions indicated that multilayer ammonia ices did not desorb below 90 K. [7] In the study by Bolina and Brown, the multilayer desorption of ammonia from graphite was consistent with the desorption of multilayer ices from metallic surfaces. Additionally, the investigation indicated that the adsorption of ammonia on graphite underwent a Volmer-Weber growth mechanism where NH_3 molecules cluster together on the surface and form 3D crystallites which later extend into 3D multilayers with continued exposure.[1] The multilayer desorption of ammonia was observed to take place at a temperature higher than that of monolayer ammonia ice, with a multilayer desorption energy of 23.2 ± 1.2 kJ mol^{-1}. This behaviour is in direct contrast to the desorption of

ices from metallic surfaces, likely owing to the organometallic chemisorption of ammonia to metal surfaces as previously described. Physisorption of ammonia is observed on HOPG surfaces and Bolina and Brown concluded the island growth observed was characteristic of the preferential formation of hydrogen bonds between ammonia molecules over formation of bonds between the adsorbate and the substrate.[1]

5.2.2 Methanol

Methanol (CH_3OH) has been detected in multiple different environments across the Universe. The formation mechanisms of methanol in interstellar environments have previously been discussed in Chapter 1. Briefly, methanol is believed to form through successive hydrogenation of carbon monoxide on the cold grain surfaces within the ISM.[8–11] Gas-phase methanol has been detected in hot cores (10^{-6}-10^{-7} abundance relative to hydrogen), dark clouds (10^{-9} abundance relative to hydrogen) and diffuse clouds (<10^{-9} abundance relative to hydrogen) in the ISM. However, the cold temperatures within the dense cores of interstellar clouds will likely lead to the "freeze-out" of molecules onto the surface of the dust grains.[1] Consequently, methanol ices have been readily observed towards high and low mass protostars, in proto-planetary disks and have even been identified as the second most abundant ice in certain environments. [12]

Ulbricht et al. have previously investigated the thermal desorption of methanol from a graphite surface. They found that methanol has a multilayer desorption peak at approximately 140 K, with a desorption energy of 46 ± 3 kJ mol^{-1}. [13] The thermal desorption of multilayer methanol was also studied by Collings et al. who observed the methanol multilayer desorption peak at approximately 150 K.[7] Sandford and Allamandola also studied the CH_3OH-CH_3OH binding energy and found the energy of desorption of multilayer methanol to be 35 ± 15 kJ mol^{-1}. [13–15] Bolina et al. investigated the desorption of methanol from graphite under interstellar conditions. Specifically, methanol was dosed onto a HOPG surface at 105 K; the graphite surface was linearly heated causing the desorption of the methanol over a particular temperature range.[16] Three different environments were observed for the desorption of methanol; monolayer and amorphous or crystalline multilayer desorption. Through data analysis and manipulation of the Polanyi-Wigner equation the desorption energy for methanol ices from graphite ranges from 31-40 kJ mol^{-1} for multilayer ices and 33-48 kJ mol^{-1} from monolayer coverages. The experiments conducted by Bolina et al. indicate that the desorption energy of methanol is coverage dependent due to the formation of hydrogen bonds between the molecules of methanol. [16]

5.2.3 Carbon Monoxide

Carbon monoxide (CO) is the second most abundant molecule in interstellar space.[17] Gaseous CO has been detected with an abundance 2.7 x 10^{-4} with respect to hydrogen in warm regions, as well

as an abundance as high as 10^{-4} with respect to hydrogen in the coldest cores. [18] Due to its high abundance, carbon monoxide is a particularly important molecule for astronomers. Whilst H_2 is the most abundant molecule in the ISM, it has no transitions that can be excited at low temperatures so can provide little insight into the structural characterisation and star formation in cold dense cores.[19,20] Carbon monoxide has bright rotation transitions in the submillimetre and millimetre range and the ^{12}C ($J = 1 \rightarrow 0$) emission is used to determine the total column density of molecular gases in different environments.[20,21] CO is also an important molecule in the reactions taking place upon the surface of the interstellar dust grains. Analysis of submillimetre and continuum data has indicated that more than 90% of carbon monoxide is frozen out onto the surface of the dust grains, for example selective depletion of CO was observed in the pre-stellar core L183, where carbon monoxide was depleted 300 times more than nitrogen.[18,21]

The formation of carbon monoxide in the interstellar medium is as a result of the reactions of carbon, both gaseous carbon and carbon trapped in carbonaceous dust grains (C^+/C/CO). In more diffuse regions, within a strong UV field, carbon is photoionized to C^+. This ionized carbon will react with hydrogen ions in the diffuse medium forming CH and CH_2, which later react with oxygen to form CO. In the dense cores, the radiation field is weaker and any C^+ formed will revert back to atomic carbon via radiative recombination. The formation of CO in dense cores is therefore likely a result of the reaction of carbon with atomic oxygen.[22]

Studies into the behaviour of carbon monoxide on astrochemically relevant surfaces have shown that CO is an interesting molecule. Carbon monoxide possesses a small dipole moment and as a result has a poor affinity for water. [23] Collings *et al.* state that owing to its unique properties, it is likely present in two different environments within the interstellar medium.[17] In particular, CO is likely to exist as pure CO ice with only minor contaminants of N_2, O_2 and CO_2, or in polar environments in mixed ices with hydrogen bonding species.[17] The orientation of the CO molecule as it binds to the surface can affect the desorption characteristics, as CO can bind to the surface via the carbon atom or the oxygen atom. Muñoz Caro *et al*. observed different behaviour when CO was deposited on a surface at temperatures below 20K to deposition above 20 K.[24] They concluded that the difference was as a result of polarization, where at higher deposition temperatures CO could reorient itself on the surface to accommodate the dipole moments and that it would transition from an amorphous ice to crystalline.[24] The polarisation of CO on surfaces was confirmed by Rosu-Finsen *et al.,* who deposited CO on ASW surfaces at temperatures of >20 K and observed the spontaneous polarisation of the CO ice, indicating that CO ices are spontelectric.[25]

The importance of carbon monoxide in icy mantles has already been discussed with regards to the formation of methanol. It is estimated that there is a particularly high abundance of not only CO ice, but CO-bearing species within the ISM.[21] It is therefore important to understand the desorption characteristics of CO as it is instrumental in the formation of complex species in interstellar clouds. Bisschop *et al.* investigated the desorption of pure CO from a gold coated Cu substrate at 14 K. Island growth of CO was observed at low coverages with desorption beginning at approximately 26 K. Multilayer coverages were noted at higher exposures and a desorption energy of approximately 7 ± 0.2 kJ mol^{-1} was obtained, which is in good agreement with the IUPAC sublimation enthalpy of CO ice (6.8 kJ mol^{-1}).[18] Noble *et al.* studied the thermal desorption characteristics of carbon monoxide from silicate and water ice surfaces at low temperatures under UHV conditions. [26] Multilayer desorption energy of CO from the surfaces was in good agreement with the values already discussed. The desorption of CO was also studied by Ulbricht *et al.*, who investigated the desorption of CO from graphite. [13] Ulbricht *et al.* obtained a desorption energy of 13 ± 1 kJ mol^{-1} for monolayer CO.

5.2.4 Carbon Dioxide

Observations of the ISM have shown that carbon dioxide (CO_2) has a very low abundance in the gas phase, with the number of CO_2 molecules at approximately 6.3 x 10^{-11} relative to hydrogen.[27] However, solid phase carbon dioxide is very abundant within the ISM. Infrared observations from the Spitzer Telescope and the Infrared Space Observatory (ISO) have indicated that carbon dioxide is a major component of the interstellar ices that form when molecules condense out onto the cold dust grain surfaces.[28] In fact, carbon dioxide is a ubiquitous species throughout the interstellar medium, having been detected in high mass protostars, low mass young stellar objects, galactic centre sources and other galaxies.[29] Carbon dioxide is also present in comets and, as comets are formed through accretion of dust grains bearing interstellar ices in the early stages of a star lifecycle, many believe that comets could provide an insight into the conditions under which our Solar System was formed.[30,31] As CO_2 is present throughout the galaxy, it is often used as a tracer molecule to investigate the thermal history of interstellar ices. The formation of CO_2 has been studied in great detail as it, along with CO, is believed to be a major store of carbon and oxygen within the ISM and therefore a vital component in the formation of more complex carbon bearing species.[28,30] Energetically, CO_2 is believed to form due to irradiation of CO with photons, charged particles or electrons, however, in the dense clouds in the ISM, formation must take place through a non-energetic process. The exact process of formation of CO_2 in dense cores is still debated and possible formation pathways are listed below (5.2 – 5.4). [27,32]

$$CO + O \rightarrow CO_2 \qquad 5.2$$

$$CO + OH \rightarrow CO_2 + H \quad 5.3$$

$$H_2CO + O \rightarrow CO_2 + H_2 \quad 5.4$$

The desorption characteristics of CO_2 have also previously been investigated. Noble et al. studied the desorption of CO_2 from a variety of different surfaces and noted that CO_2 exhibited intermediate wetting behaviour upon all the surfaces, indicating that it favoured the formation of islands before fully wetting the surface in a thin monolayer. [26] Edridge *et al.* also observed this behaviour in their experiments examining the desorption of CO_2 from HOPG. They noted that a sub-monolayer desorption peak was observed at 83 K, with the additionally observation of a low temperature shoulder at 77 K corresponding to the formation of multilayer CO_2 ices. The temperature of desorption of this multilayer shoulder increased with increased exposure and could not be saturated, which is consistent with multilayer desorption. [28] This lower temperature peak is consistent with the formation of islands, where CO_2 preferentially binds to other CO_2 molecules instead of to the surface. Edridge *et al.* also extracted desorption energies for monolayer CO_2 from graphite (20.2 ± 2.3 kJ mol^{-1}) as well as multilayer CO_2 (24.8 ± 1.6 kJ mol^{-1}), which were in good agreement with previously studies. [13,28,29]

5.3 Experimental methodology

The apparatus used in the experiments discussed here has been outlined in detail in Chapter 2. In this study, ammonia, methanol, carbon monoxide and carbon dioxide (99.9% purity) were dosed separately onto a HOPG surface with fluxes of 4.58 x 10^{-3} ML s^{-1}, 2.78 x 10^{-3} ML s^{-1}, 3.1 x 10^{-2} ML s^{-1} and 2.1 x 10^{-3} ML s^{-1} respectively, where for our surfaces 1 ML = 2 x 10^{15} molecules based upon the assumption by Amiaud *et al.* that 1 ML = 10^{15} molecules cm^{-2}, where the surface area of the graphite substrate is 2 cm^2.[33] The surface temperature during deposition was held constant for each gas. The gases were dosed onto the surface of the graphite for specific lengths of time, before the surface was heated linearly and TPD spectra were recorded for each dose. The surface was cleaned to 250 K between experiments. The scotch-tape method was used to initially clean the surface prior to insertion into the Cosmic Dust apparatus. The gases were individually plumbed into the apparatus, and the system was purged and then flushed with the gas prior to experiment. Liquid methanol was plumbed into the system and then degassed via three consecutive freeze-pump-thaw cycles to remove dissolved gas impurities.

5.4 Results and Discussion

In this section the desorption characteristics of each gas from graphite will be discussed individually. The TPD profiles of each gas were used to derive kinetic parameters as discussed in detail in Chapter 3.

5.4.1 Desorption of Ammonia from Graphite

The desorption spectra for a range of doses of ammonia from the graphite surfaces are shown below (Figure 5.1a and 5.1b). Ammonia gas (99.9% purity) was dosed onto the graphite surface held at 22 K. The dosing period was varied from 2 mins to 1hr. While the major ion observed for ammonia in the mass spectrometer is the mass 17 ion (NH_3^+), the spectra detailed below show the data for the mass 16 ion. The data was analysed using *m/z* 16 to the prevent any contaminants in the spectra from the mass 17 water fragment ion (OH^+) that is present owing to the small amount of water ice present within the main chamber. The ratio of the areas under the peaks for mass 17 and mass 16 were compared for each experiment to ensure it remained constant.

As can be seen in Figure 5.1a, the sub- monolayer desorption of ammonia from the graphite surface peaks at 94 K (Peak A). However, even in the lowest doses, a small shoulder is observed to the right of the monolayer desorption peak (Peak B). This higher temperature peak can be assigned to the desorption of NH_3 multilayer ices. As the dose is gradually increased the intensity of Peak B also increases, while shifting to higher temperatures. At a dose of 8 mins (2.4 ML), the intensities of Peak A and Peak B are approximately equal. Further increase of exposure shows that Peak A has saturated whereas Peak B continues to grow in intensity, until Peak B dominates the spectrum, as shown in Figure 5.1b.

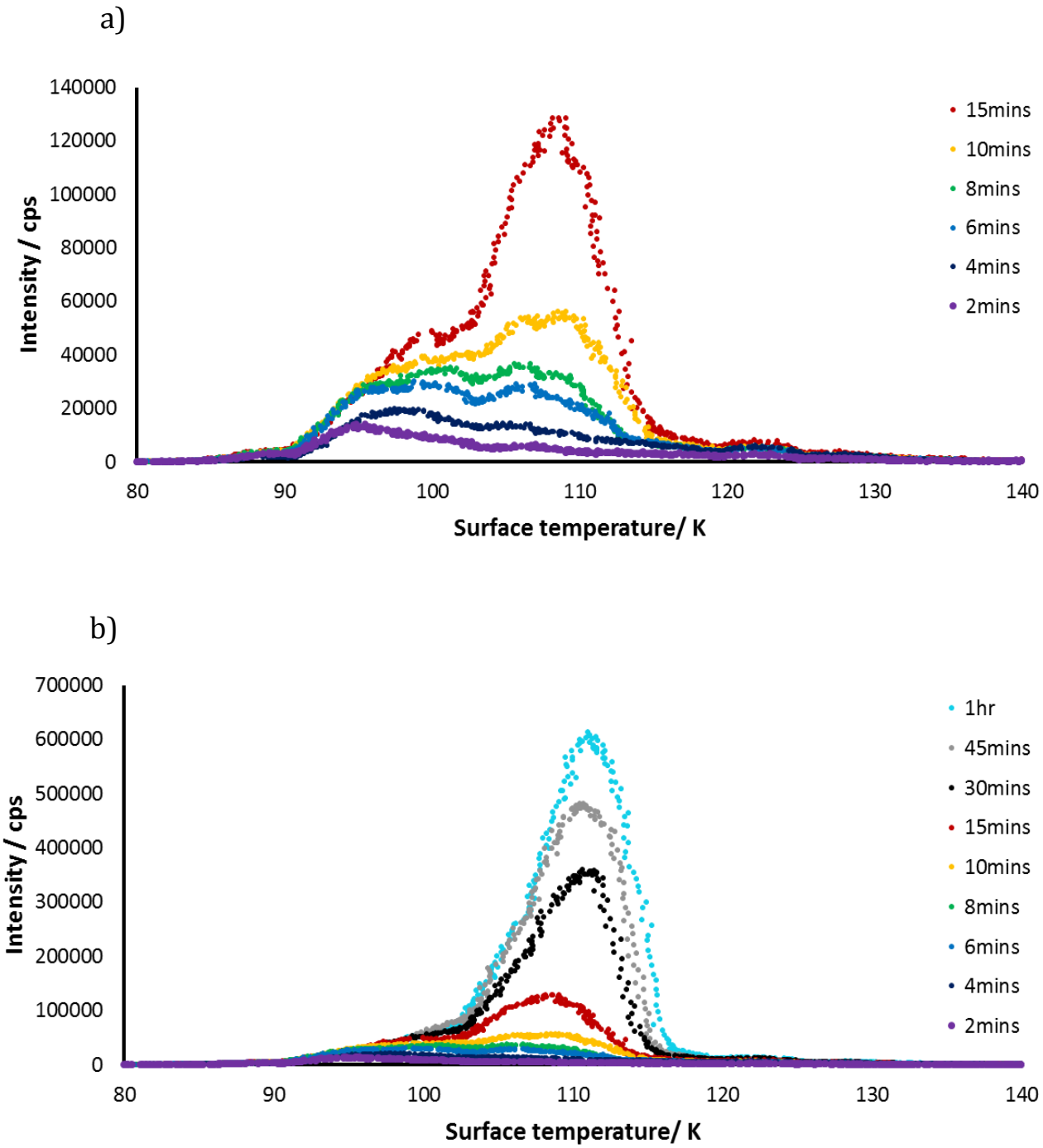

Figure 5.1: Desorption spectra of ammonia from the graphite surface dosed at 22K, a) desorption spectra of ammonia for lower doses, from 2 mins to 15 mins and b) desorption spectra of ammonia showing all doses, including high doses (30mins, 45mins and 1hr) where the multilayer desorption peaks dominate.

The desorption characteristics shown here are consistent with those observed by Bolina and Brown.[1] They noted that multilayer desorption of ammonia from graphite occurred simultaneously with monolayer or sub-monolayer desorption. With increased exposure, Bolina

and Brown also observed the dominance of Peak B, which continually shifted to higher temperature and so they classified the desorption here as multilayer. As outlined above, Peak B is due to the formation of islands of NH_3. This island formation occurs as the ammonia molecules preferentially bind to each other rather than to the surface. The ammonia molecules bind through hydrogen bonding, which is marginally stronger than the binding energy of the molecules to the surface. Hence, the multilayer Peak B is observed to desorb at higher temperatures, as more energy is required to break the hydrogen bonds between molecules than the weak bonds between the ammonia and the surface.

Analysis of the desorption spectra of ammonia was conducted via manipulation of the Polanyi-Wigner equation as discussed in Chapter 3. The TPD profiles of ammonia desorption for longer doses were examined and calculations revealed the order of desorption for multilayer ammonia to be 0.57 ± 0.05 which is a fractional desorption order. Bolina and Brown also calculate a fractional desorption order (0.25 ± 0.05) for multilayer ammonia.[1] Fractional orders of desorption, as opposed to zeroth orders, are expected for ammonia due to the formation of strong hydrogen bonds with other ammonia molecules. Further calculations allowed for the determination of the desorption energy of ammonia, which was found to be 25.13 ± 0.59 kJ mol^{-1}. This value is in good agreement with the values previously obtained for the desorption of multilayer ammonia, such as 23.3 kJ mol^{-1} and 25 kJ mol^{-1}.[1,13]

5.4.2 Desorption of Methanol from Graphite

The desorption spectra of methanol from graphite at different exposures are shown below (Figures 5.2 & 5.3). Methanol was dosed onto graphite held at 18 K for doses ranging from 2 mins to 1 hr. As the major fragmentation ion for methanol in the mass spectrometer is CH_3O^+, the desorption spectra analysed for methanol were the spectra of the mass 31 ion. The molecular ion peak at mass 32 was also continuously monitored throughout each experiment to ensure the ratio of fragment ion and parent ion remained the same for each experiment.

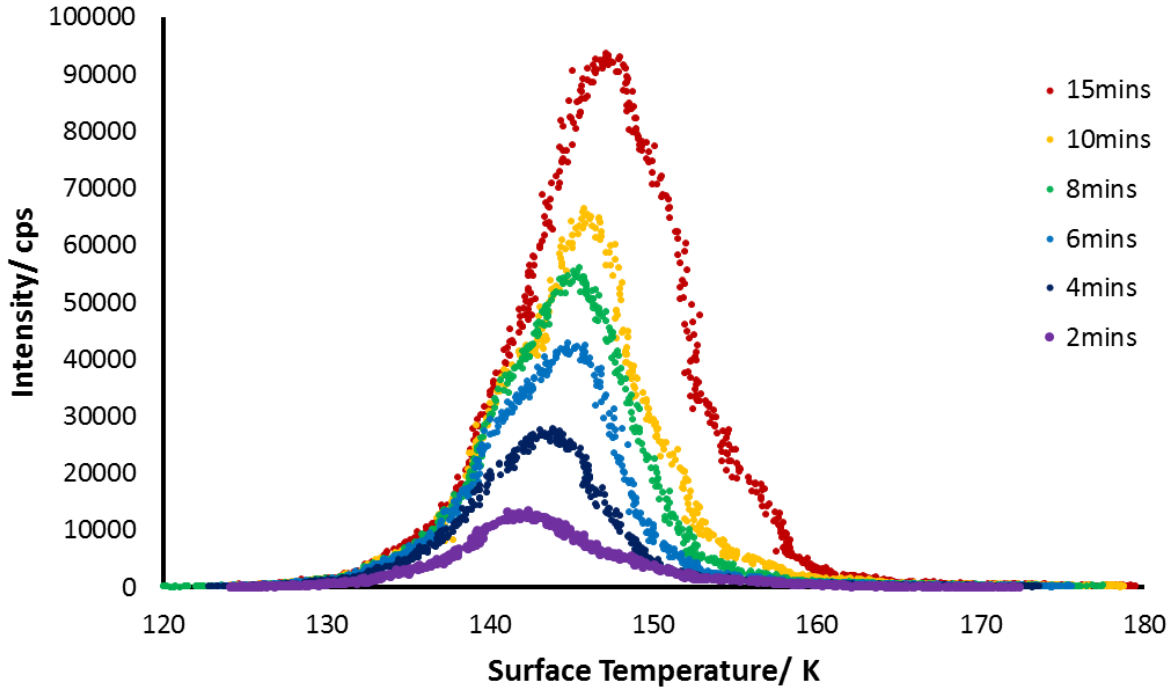

Figure 5.2: Desorption spectra of methanol from the graphite surface, dosed at 22K, for doses from 2 mins to 15 mins.

At the lowest dose, a peak is observed on the desorption spectrum at 143 K (Peak A). This peak has a slight shoulder at 139 K (Peak B). As the length of dose is increased, the intensity of Peak A increases. Peak B also increases in intensity with longer exposures, whilst also shifting to higher peak temperatures. In the spectra shown in Figure 5.2, the lower temperature shoulder moves to higher temperatures with increasing dose until it can no longer be seen. At this point Peaks A and B have merged. Within increased exposure Peak A saturates, while Peak B continues to grow and shift to higher temperatures.

As the dose is increased further, an additional peak (Peak C) forms at 155 K, as shown in Figure 5.3. If the dose is increased both Peak B and Peak C continue to grow with increasing exposure and shift to higher temperature.

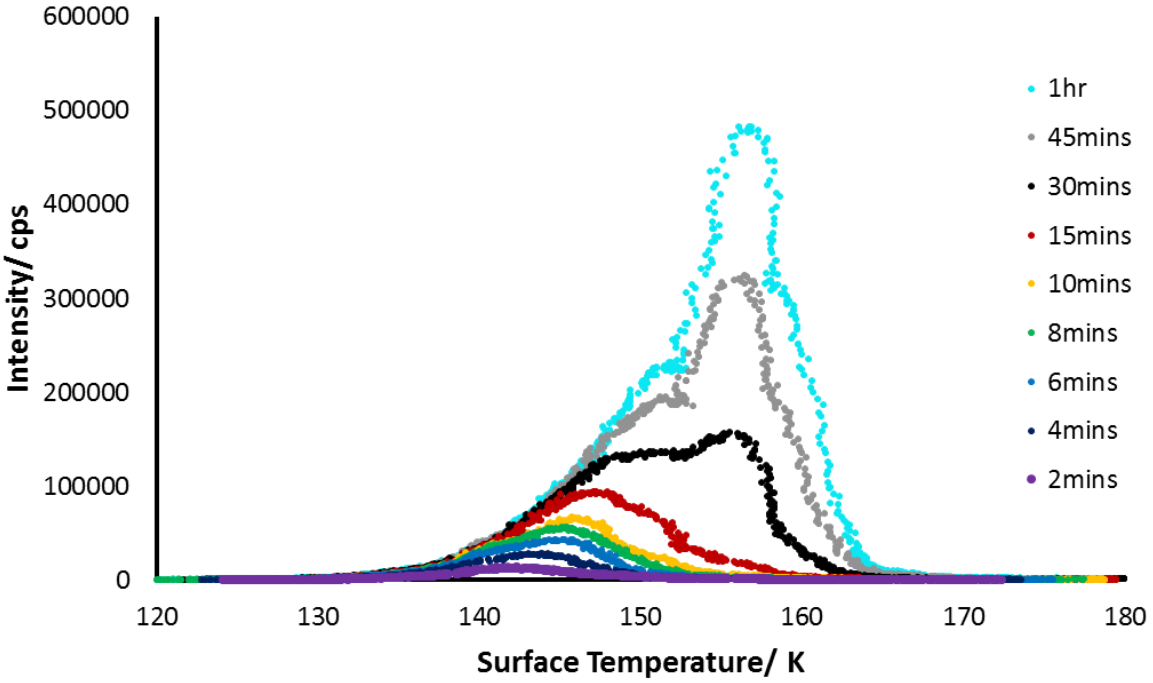

Figure 5.3: Desorption spectra of methanol from the graphite surface at 22 K for doses from 2 mins to 1hr. An additional peak (Peak C) is observed for higher doses at 155 K.

The spectra observed in these experiments are consistent with the spectra observed from previous studies of the desorption characteristics of methanol from a graphitic surface.[7,16] Peak A can be assigned to the monolayer peak as it is eventually saturated with increasing dose, consistent with the filling of a complete monolayer on the graphite surface. Peak B can be assigned to multilayer desorption. As is apparent from the growth of both Peak A and Peak B at lower doses, the multilayer ice forms concurrently with the monolayer ice, suggesting the formation of "islands" on the surface as observed above for the formation of ammonia ices. This island growth suggests that methanol molecules can bind together on the surface rather than solely binding with the surface itself. For methanol, this is likely due to the ability of the molecules to hydrogen bond to each other. [16] The final peak, Peak C is assigned to the formation of crystalline methanol ice. This ice was previously observed by Bolina et al. who noted the additional peak when using high exposures of methanol over 130 K. [16] Through analysis of both RAIRS data and TPD, they were able to assign this additional peak to the desorption of multi-layered crystalline methanol ice. Crystalline ice desorbs at higher temperatures than amorphous ice (Peak B) owing to the greater number of hydrogen bonds. [16] A slight artefact is observed for the 1hr dose at approximately 152 K. This is cause by the slight oscillations in the heating ramp, as outlined in

Chapter 2. As discussed below, the data was fitted therefore the effect of this oscillation on the calculation of kinetic parameters was minimal.

In order to gain accurate values for the desorption energy of methanol from the surface of graphite, it is necessary to separate the peaks in the desorption spectra. As a result, the data was peak fitted. Specifically, a Lorentzian peak shape was used, in line with the parameters that that Bolina et al. used in their studies. An example of the fitted data verses the experimental data is shown in Figure 5.4, which shows the fitting of the data at 45min dose. In each case, the integrated area under the experimental data was compared to the integrated are under the fitted data to investigate the accuracy of the fit. The integrated areas were found to be in good agreement.

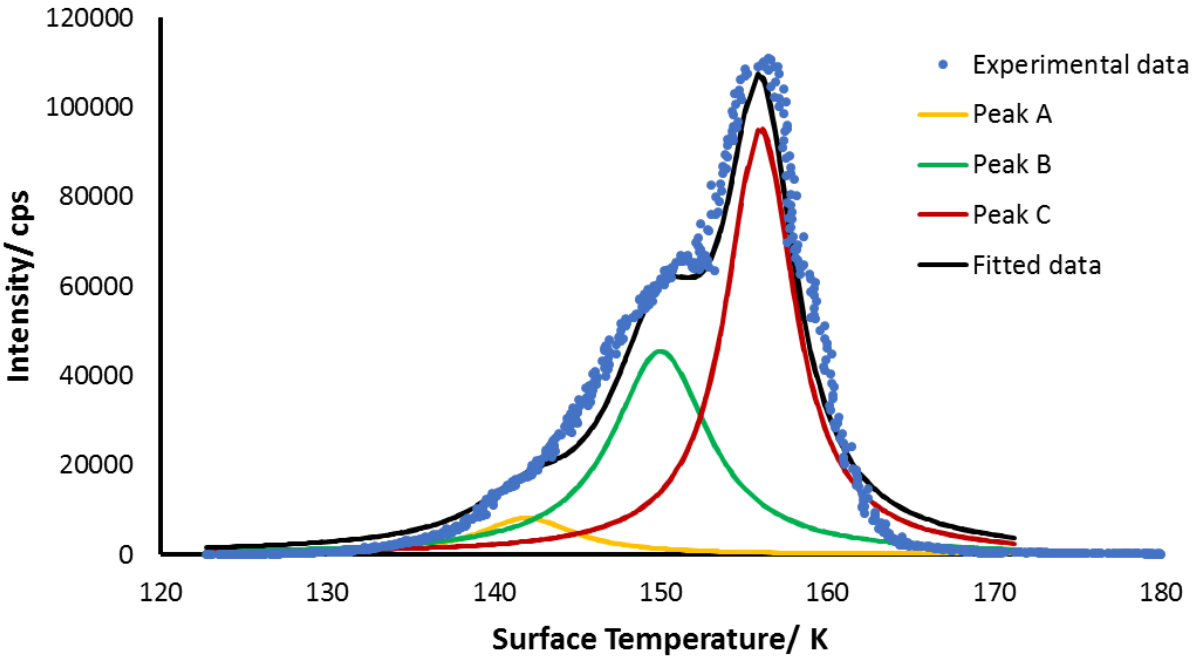

Figure 5.4: Spectra showing the experimental data (blue) versus the overall fit (black). The data is fitted using the desorption characteristics of Peak A (yellow), Peak B (green) and Peak C (red), which correspond to the desorption of monolayer, amorphous multilayer and crystalline multilayer ices respectively.

Through analysis of the fitted peaks, the desorption energy of amorphous multilayer methanol from the surface of graphite was found to be 42.7 ± 1.1 kJ mol^{-1}. This value is in relatively good agreement to the values obtained by Bolina et al., although it is slightly higher than what they observed for the multilayer desorption (31 - 40 kJ mol^{-1}).[16] This may be due to differences in the fit of the spectra, causing a slight difference in results.

5.4.3 Desorption of Carbon Monoxide from Graphite

The desorption profile of carbon monoxide from the graphitic surface is shown in Figure 5.5. This figure shows the profile for various different doses of CO ranging from 4 mins to 30 mins. However, owing to the high flux of CO employed in these experiments all the desorption behaviour observed was for multilayer ice. The HOPG surface was maintained at 18 K during deposition. The mass monitored throughout the experiments with carbon monoxide was mass 28. Mass 28 is also the mass of molecular nitrogen, so there is slight contamination in the spectra from N_2 desorption at approximately the same temperature. However, as multilayer doses of CO have been used this should have little effect on the desorption profile, as only a small amount of background N_2 is present within the ultra-high vacuum chamber.

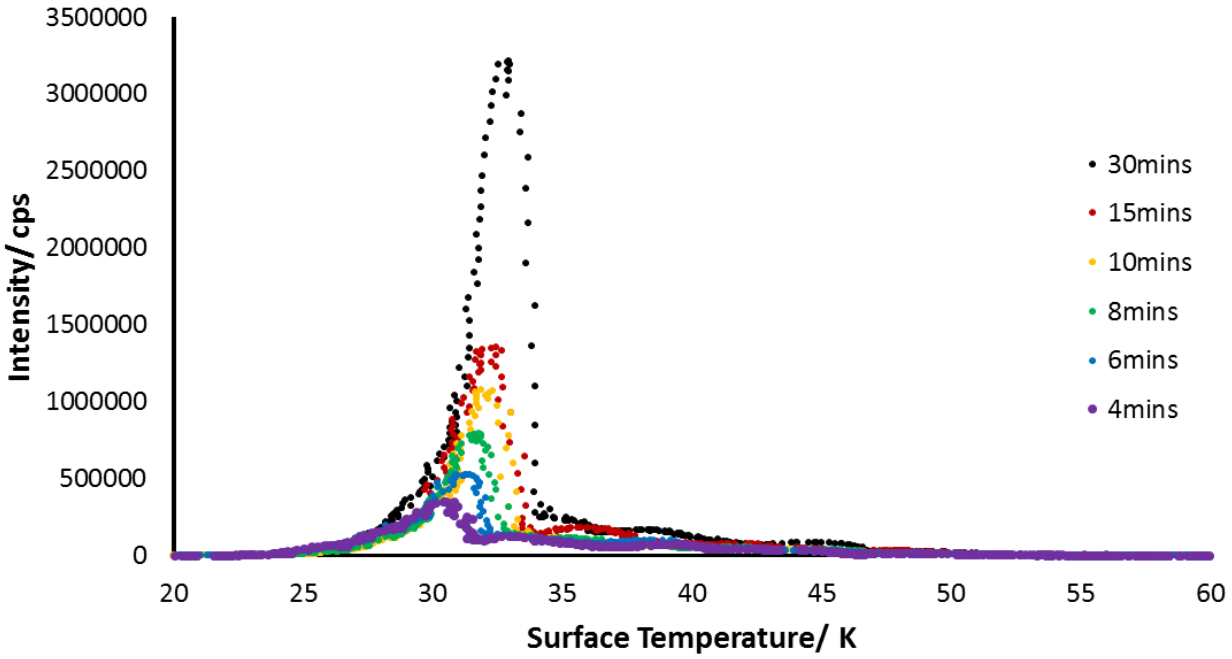

Figure 5.5: Desorption spectra of carbon monoxide from the HOPG surface. The profiles of different doses, increasing from 4 mins to 30 mins, are shown.

The intensity of the peak and temperature of maximum desorption increases with increasing dose (Figure 5.5), from 30 K to 33 K. This is consistent with the desorption characteristics observed in previous studies into the desorption of multilayer CO.[18,26] The multilayer desorption energy of carbon monoxide was found to be 5.17 ± 0.73 kJ mol^{-1}. This value is slightly lower than the values obtained by Bisschop *et al.,* who found the multilayer desorption energy of CO to be 7.11 ± 0.21 kJ mol^{-1}.[18] The discrepancy here is likely due to the quality of the data obtained during the course

of our experiments. The particular temperature range over which carbon monoxide desorbs, is prone to experimental issues concerning the heating rate. The heating rate is not perfectly linear in these regions, and the slight deviation in temperature from linear behaviour causes small "wiggles" in the spectra, specifically the leading edge, as outlined in Chapter 2 This can lead to inaccuracies with the desorption energy calculations as the oscillations in the temperature cause premature desorption with regards to the heating rate. For calculations, the data was fitted, to reduce the errors caused by these spectral artefacts as discussed in Chapter 2.

5.4.4 Desorption of Carbon Dioxide from Graphite

The desorption spectra of carbon dioxide from the graphite surface are shown in Figures 5.6 and 5.7. Carbon dioxide was dosed onto the surface for various lengths of time ranging from 2 minutes to 1 hour. The temperature of the surface was held constant at 22 K during deposition. The surface was then linearly heated to cause desorption of the CO_2 ice over a particular range (Figure 5.6 & 5.7). During the desorption experiments the ion of mass 44 was monitored, corresponding to the molecular ion peak of CO_2.

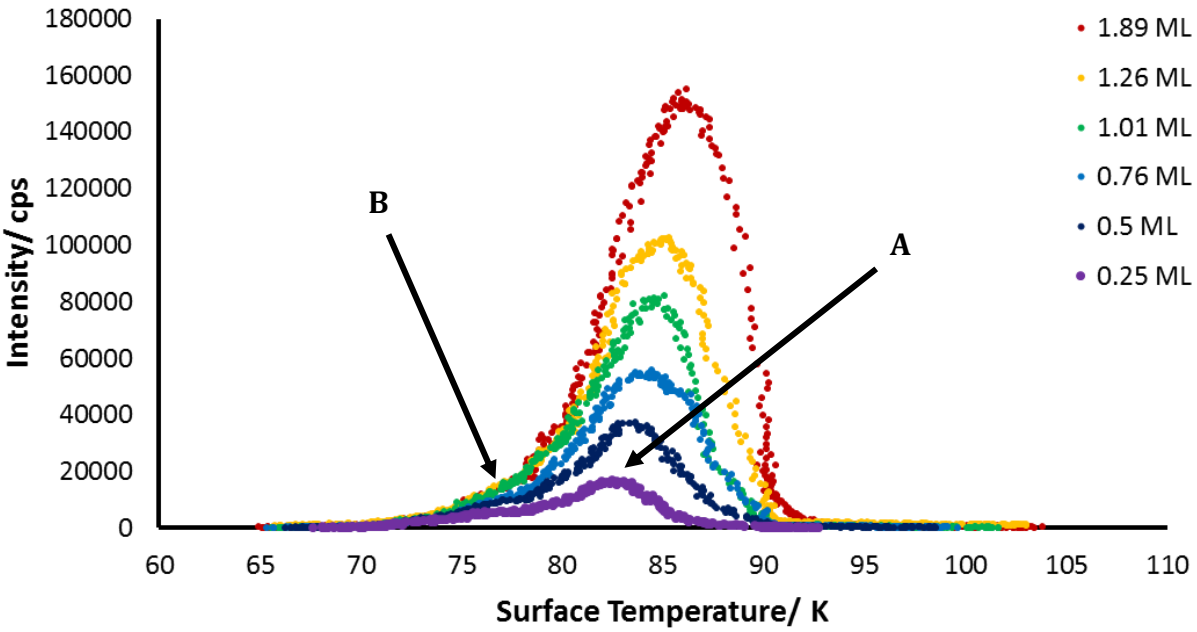

Figure 5.6: Desorption spectra of carbon dioxide from the HOPG surface. The profiles of different doses, increasing from approximately 0.25 ML to 1.9 ML, are shown. Peaks A and B are labelled.

At the lowest dose of CO_2, a single peak is observed on the desorption spectrum at 83 K (Peak A). This peak has a small shoulder to the left at approximately 77 K (Peak B). As the dose is increased

both Peak A and Peak B increase in intensity. Peak B also increases in temperature, shifting to the right so that it merges with Peak A. With increasing dose Peak A saturates and Peak B continues to grow and cannot be saturated.

The desorption profile of carbon dioxide from graphite observed here is consistent with the desorption characteristics observed in previous studies. [28] The peak at 83 K can be assigned to monolayer desorption of CO_2 from graphite. The low temperature peak can be assigned to the desorption of multilayer CO_2 ice as Peak B continues to grow with increasing dose, which is characteristic of the desorption profiles of multi-layered ice. Due to the formation of multilayer ice before the monolayer peak has saturated, it is clear that CO_2 also exhibits "island" formation before it covers a full monolayer, indicating the preferential formation of CO_2-CO_2 bonds as opposed to substrate-adsorbate bonds. The desorption energy of the multi-layered ice was calculated to be 19.75 ± 2.80 kJ mol^{-1}, in relatively good agreement with values observed in previous studies.[28] The slight discrepancy observed is likely due to errors in extraction of the monolayer and multilayer peaks through peak fitting.

The desorption profiles of longer CO_2 doses have been added to the plot below (Figure 5.7). As can be seen from this figure, longer exposure of the surface to CO_2 leads to the formation of an additional peak (peak C) at 92 K. The peak was not observed by Edridge *et al*. who did not dose to the same high coverages. However, Edridge *et al*, observed that the desorption order of CO_2 from multilayer ices was not zeroth order, as the spectra did not share a leading edge. They surmised that this was likely due to the formation of crystalline CO_2 ice at temperature over 87 K.[28] It is, therefore, likely that the peak observed at 92 K can be assigned to desorption of multilayer crystalline CO_2 ice.

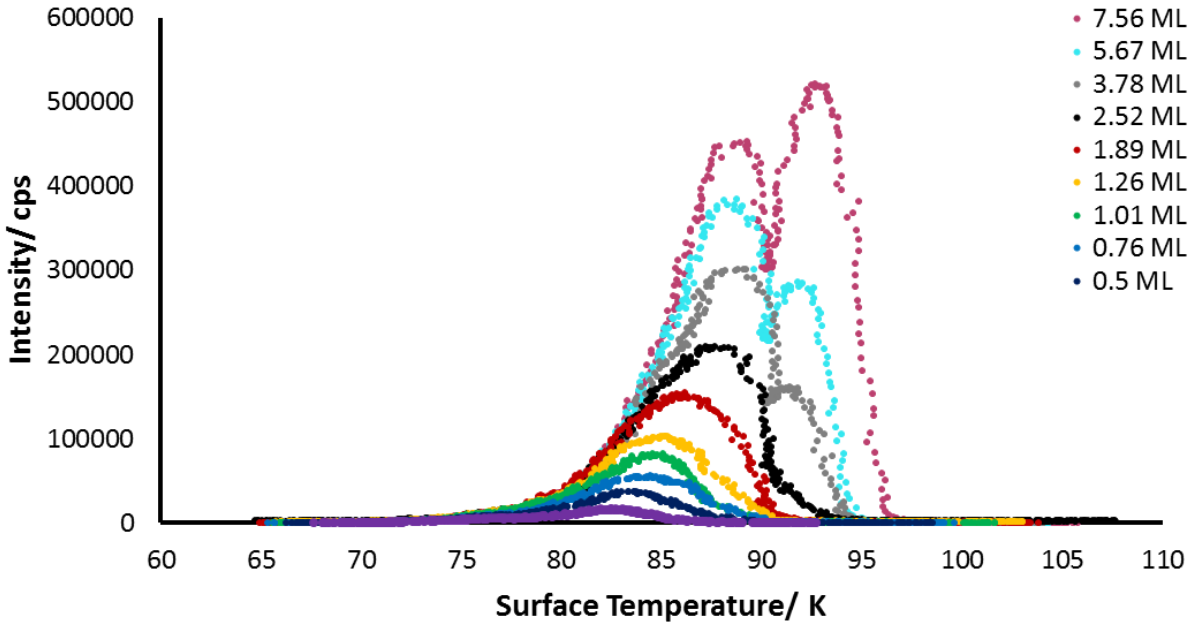

Figure 5.7: Desorption spectra of carbon dioxide from the HOPG surface showing longer doses. The additional peak (Peak C) is observed at 92 K is tentatively assigned to crystalline CO_2 ice.

5.5 Summary

In this Chapter the desorption characteristics of several molecules were analysed. The molecules; ammonia, methanol, carbon monoxide and carbon dioxide have all been observed in the interstellar medium and are thought to contribute significantly to the chemistry taking place within the dense cores

The desorption characteristics of each gas were analysed using the Cosmic Dust apparatus discussed in Chapter 2. The multilayer desorption energy of each of the ices were calculated through manipulation of the TPD data and the Polanyi-Wigner equation as detailed in Chapter 3. For the majority of the species, the desorption characteristics observed were in good agreement with the values previously observed in the literature, excepting carbon monoxide, which was a little low and likely the result of experimental issues as outlined above. Interestingly, an additional peak was observed in the desorption profile of CO_2 ices, at higher temperatures. This was only visible at higher doses and has tentatively been assigned to the desorption of crystalline CO_2 ice.

In summary, the good agreement between the characteristics we observe for the desorption experiments for each gas, and the desorption characteristics observed in the literature indicates that we can believe our TPD methodology and apply it to new systems.

5.6 References

1. A. S. Bolina and W. A. Brown, *Surf. Sci.*, 2005, **598**, 45–56.

2. W. Hagen, *Astron. Astrophys.*, 1982, **114**, 245–260.

3. H. G. M. Hill and J. A. Nuth, *Astrobiology*, 2003, **3**, 291–304.

4. P. P. Bera, T. Stein, M. Head-Gordon and T. J. Lee, *Astrobiology*, 2017, **17**, ast.2016.1614.

5. J. B. Bergner, K. I. Öberg, M. Rajappan and E. C. Fayolle, *Astrophys. J.*, 2016, **829**, 85.

6. J. Le Bourlot, *Astron. Astrophys.*, 1991, **242**, 235.

7. M. P. Collings, M. A. Anderson, R. Chen, J. W. Dever, S. Viti, D. A. Williams and M. R. S. McCoustra, *Mon. Not. R. Astron. Soc.*, 2004, **354**, 1133–1140.

8. D. E. Woon, *Astrophys. J.*, 2002, **569**, 541–548.

9. N. Watanabe, A. Nagaoka, T. Shiraki and A. Kouchi, *Astrophys. J.*, 2004, **616**, 638–642.

10. S. B. Charnley, A. G. G. M. Tielens and S. D. Rodgers, *Astrophys. J.*, 1997, **482**, L203–L206.

11. O. M. Shalabiea and J. M. Greenberg, *Astron. Astrophys.*, 1994, **290**, 266–278.

12. E. S. Wirström, W. D. Geppert, Å. Hjalmarson, C. M. Persson, J. H. Black, P. Bergman, T. J. Millar, M. Hamberg and E. Vigren, *Astron. Astrophys.*, 2011, **533**, 1–11.

13. H. Ulbricht, R. Zacharia, N. Cindir and T. Hertel, *Carbon N. Y.*, 2006, **44**, 2931–2942.

14. L. J. Sandford, Scott A.; Allamandola, *Astrophys. J.*, 1993, **417**, 815.

15. H. M. Cuppen, C. Walsh, T. Lamberts, D. Semenov, R. T. Garrod, E. M. Penteado and S. Ioppolo, *Space Sci. Rev.*, 2017, **212**, 1–58.

16. A. S. Bolina, A. J. Wolff and W. A. Brown, *J. Chem. Phys.*, 2005, **122**, 044713..

17. M. P. Collings, J. W. Dever and M. R. S. S. McCoustra, *Phys. Chem. Chem. Phys.*, 2014, **16**, 3479–3492.

18. S. E. Bisschop, H. J. Fraser, K. I. Öberg, E. F. van Dishoeck and S. Schlemmer, *Astron. Astrophys.*, 2006, **449**, 1297–1309.

19. K. Joachimi, E. Gatuzz, J. A. García and T. R. Kallman, *Mon. Not. R. Astron. Soc.*, 2016, **461**, 352–357.

20. T. G. Bisbas, E. F. van Dishoeck, P. P. Papadopoulos, L. Szűcs, S. Bialy and Z.-Y. Zhang, *Astrophys. J.*, 2017, **839**, 90.

21. M. Minissale, A. Moudens, S. Baouche, H. Chaabouni and F. Dulieu, *Mon. Not. R. Astron. Soc.*, 2016, **458**, 2953–2961.

22. C. Cecchi-Pestellini, S. Casu and F. Scappini, *Mon. Not. R. Astron. Soc.*, 2001, **326**, 1255–1260.

23. E. Escamilla-Roa, F. Moreno, J. J. López-Moreno and C. I. Sainz-Díaz, *Planet. Space Sci.*, 2017, **135**, 17–26.

24. G. M. Muñoz Caro, Y.-J. Chen, S. Aparicio, A. Jiménez-Escobar, A. Rosu-Finsen, J. Lasne and M. R. S. McCoustra, *Astron. Astrophys.*, 2016, **589**, A19.

25. A. Rosu-Finsen, J. Lasne, A. Cassidy, M. R. S. McCoustra and D. Field, *Phys. Chem. Chem. Phys.*, 2016, **18**, 5159–5171.

26. J. A. Noble, E. Congiu, F. Dulieu and H. J. Fraser, *Mon. Not. R. Astron. Soc.*, 2012, **421**, 768–779.

27. M. Minissale, E. Congiu, G. Manicò, V. Pirronello and F. Dulieu, *Astron. Astrophys.*, 2013, **559**, A49.

28. J. L. Edridge, K. Freimann, D. J. Burke and W. A. Brown, *Philos. Trans. R. Soc. A Math. Phys. Eng. Sci.*, 2013, **371**, 20110578–20110578.

29. J. A. Noble, F. Dulieu, E. Congiu and H. J. Fraser, *EAS Publ. Ser.*, 2012, **58**, 353–356.

30. S. A. Sandford and L. J. Allamandola, *Astrophys. J.*, 1990, **355**, 357.

31. O. Gálvez, I. K. Ortega, B. Maté, M. A. Moreno, B. Martín-Llorente, V. J. Herrero, R. Escribano and P. J. Gutiérrez, *Astron. Astrophys.*, 2007, **472**, 691–698.

32. M. Minissale, J.-C. Loison, S. Baouche, H. Chaabouni, E. Congiu and F. Dulieu, *Astron. Astrophys.*, 2015, **577**, A2.

33. L. Amiaud, F. Dulieu, J. H. Fillion, A. Momeni and J. L. Lemaire, *J. Chem. Phys.*, 2007, **127**, 144709.

Chapter 6: The Desorption Characteristics of Astrochemically Relevant Molecules from an Amorphous Carbonaceous Surface (ACS)

6.1 Overview

In this chapter, desorption from an amorphous carbonaceous dust grain analogue will be assessed. In particular, the desorption profiles of various molecules from an amorphous carbonaceous surface composed of broken fullerene-like structures will be investigated. The previous studies into amorphous surfaces similar to the one examined in this chapter will also be reviewed.

6.2 Introduction

6.2.1 Carbonaceous Dust Grains

Rich chemistry is taking place within the ISM, however, gas-phase reactions alone cannot account for the observed abundance of some molecules.[1] Therefore, it is likely that surface reactions are significant within the ISM, particularly within the colder, dense areas of the interstellar dust clouds. In these dense clouds the gases will adsorb onto the cold surfaces of the dust grains as molecular or atomic ices.[2] The formation of ices on the surface of dust grains provides a pathway through which different molecules can interact, and then, react together. Consequently, it is believed that the majority of complex organic molecules (COMs) that have been detected in the ISM are most likely the result of the reactions upon the surfaces.[3,4] As a result, it is vital that one understands the nature of the dust grains present within the ISM and how the gaseous atoms or molecules will interact with the surfaces of these grains. As previously discussed in Chapter 1, the dust grains are mostly amorphous carbonaceous or silicate-based materials.[5,6] This Chapter will focus on the carbonaceous materials, as very little is known about the actual structures and catalytic properties of this class of dust grains in the ISM.

The main laboratory analogue for carbonaceous dust grains is graphite.[7] However, it is unlikely that the graphitic surfaces are an accurate representation of the surfaces found within the ISM. Solid carbon can exist as many different allotropes including diamond, graphite, graphene, polyynes, carbon nanotubes and fullerenes.[8] As carbon can exist in these numerous forms, it is difficult to elucidate the exact structure of the grains in the ISM, particularly because the dust grains will also likely be subject to extreme processing by UV radiation and cosmic rays.[4,9] Previous studies have suggested possible structures for the amorphous carbon-based grains within the interstellar medium. Amorphous carbons (ACs) and hydrogenated amorphous carbons

(HAC) have previously been presented as possible dust grain analogues.[10] ACs and HACs can refer to hydrogen-poor or highly hydrogenated amorphous carbonaceous grains respectively, with mixed sp, sp^2 and sp^3 bonding and varying C:H ratios, all of which ultimately show no long-range order.[8] These surfaces are normally characterized by aromatic islands, of different sizes, which are linked by aliphatic structures with numerous degrees of hybridisation. However, there is currently no clear discrimination between ACs and HACs based upon the size of their aromatic and aliphatic areas, or based upon the C:H ratio.[8] Consequently, AC and HAC structures provides only a broad view into the possible structures of the carbonaceous interstellar dust grains.

Sakata *et al.* proposed that HACs with clusters of aliphatic and aromatic structures could be used as suitable dust grain analogues.[11] This type of HAC is generated in hydrocarbon plasmas and is known as a quenched carbonaceous composite (QCC).[12] Another class of carbonaceous structure that has been suggested are nanosized onion-like or fullerene-like grains including nested buckyonions generated from gas-phase condensation reactions.[8] In this chapter these fullerene-like grains will be examined in more detail and their relevance to the interstellar medium will be assessed.

6.2.2 Fullerenes in Space

Fullerenes are well-known macromolecules that have been detected throughout the interstellar medium. In 1985, Kroto *et al.* investigated the mechanism of formation of carbon chains in circumstellar envelopes and interstellar environments and noticed the formation of buckminsterfullerene (C_{60}), a cage-like macromolecule made of carbon.[13] Kroto *et al.* argued that C_{60} and fullerene analogues should be considered as possible carriers of the diffuse absorption features observed along various lines-of-sight in space, known as diffuse interstellar bands (DIBs).[13] The DIBs refer to a set of optical absorption features observed in the spectra of starlight that has travelled through interstellar dust clouds.[14] These absorption features are broad peaks (when compared to the relative sharpness observed from atomic transitions) and, until recently, they remained unidentified. To date, over 500 DIBs have been detected along various lines of sight.[14] As they are consistently observed along these sightlines with little variation in the broadness of the peaks despite different environmental conditions, it is believed that the absorption peaks are caused by intrinsic properties of the DIB carriers and not environmental factors.[14,15] Furthermore, as they are observed throughout the interstellar medium, it was deduced that these carriers must be formed readily in a number of different environments, and that the structures are stable in the harsh conditions of the ISM.[8,14] Kroto *et al.* argued that as both the DIB carriers and fullerenes form spontaneously from carbon dust and both species are stable under intense radiation, such as would be observed in the diffuse clouds of the interstellar medium, that it was highly likely that fullerenes represented some of the DIB carriers.[16] This

theory was further substantiated by numerous studies that indicated fullerenes formed readily in both random nucleation processes and in the presence of hydrogen and oxygen, both of which could coincide with the formation of fullerenes (C_{60}, C_{60}^+, C_{70} etc.) in interstellar environments.[17–19]

Neutral C_{60} was first detected in the gas-phase in the planetary nebula Tc-1.[14,20] Since then it has been detected along many more lines of sight including in the reflection nebulae NGC 7023 and NGC 2023, the proto-planetary nebula IRAS 01005+7910, the circumstellar envelopes of post-asymptotic giant branch stars, molecular outflows from young stellar objects (YSOs), and in a large number of planetary nebulae in the Milky Way and the Magellanic Clouds.[15] The first DIB was successful identified by Campbell *et al.* who used gas-phase experiments to obtain an accurate wavelength of the electronic transition of C_{60}^+.[21] The transitions were consistent with DIBs observed at 9577 Å and 9632 Å.[14,22] However, to date the vast majority of the DIBs remain unidentified and could be caused by fullerene-like structures in the interstellar clouds. As the detection of C_{60} and C_{60}^+ have shown that fullerenes are present in the gas phase in diffuse interstellar clouds, it is highly likely that the fullerenes are also present as solid nanoparticles within the dense regions of the ISM owing to their stability under harsh conditions.[16] In fact, it is estimated that >1% of the available carbon in some astronomical objects are contained within fullerenes.[15] Therefore, it is important to understand how fullerene-like structures can form and how the gas molecules will interact with them.

6.2.3 The Lifecycle of Cosmic Dust

The lifecycle of cosmic dust grains is outlined in Figure 6.1. The dust grains of the ISM are originally formed in supernovae or *via* gas-phase condensation in envelopes of asymptotic giant branch (AGB) stars.[19] Stellar winds and shockwaves distribute the dust from stellar environments, and eventually these dust grains and gas molecules will gravitate together to form interstellar environments.[19] As the density increases, the inner core of the cloud is shielded from UV radiation (from surrounding stars and protostars) by an outer protective layer of gas and dust, as described in Chapter 1. Eventually the densest region of the clouds will collapse to form a star. After this stage, the dust grains can be expelled into molecular clouds to start the star-forming cycle again, dispersed by the formation of the new star or eventually incorporated into planetary matter around the newly formed star. [23]

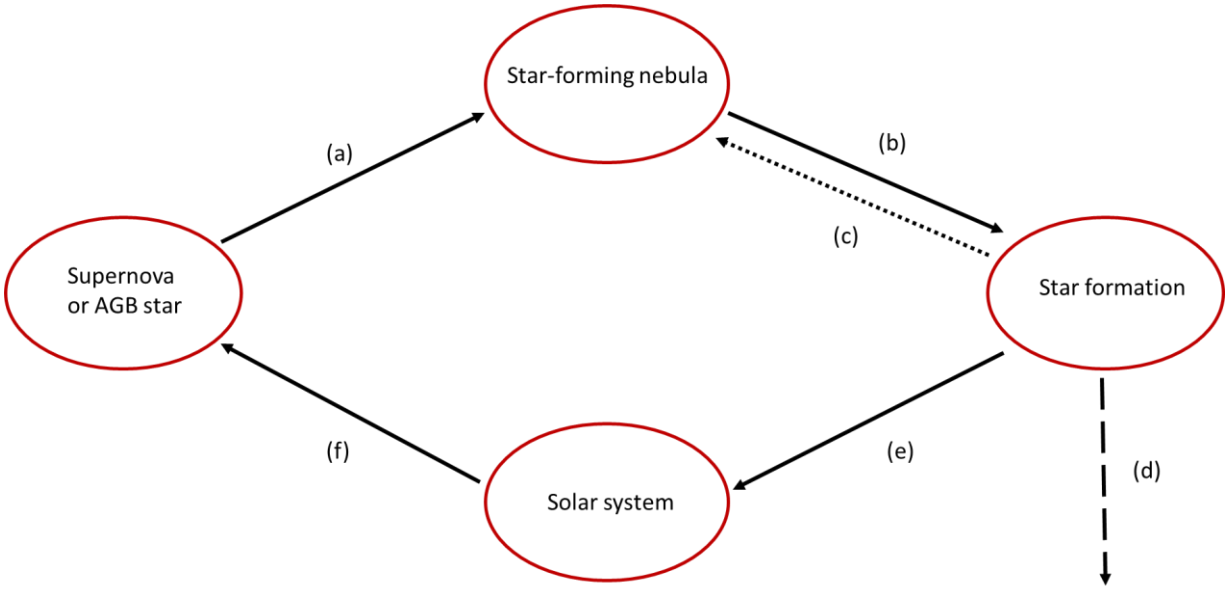

Figure 6.2: Diagram showing the cycle of dust grains in space: a) The dust grains which are formed via supernova or in an AGB star are distributed into interstellar environments (star-forming regions) by shock waves and solar winds, b) the dust grains gravitate together in the dense regions of interstellar clouds until they collapse to form a star, c) the dust remaining after star formation can either be cycled back into the star forming region, d) or it can be dispersed, e) or it can enter into planetary or solar systems where it will eventually accrete together to form planets and moons etc, f) after a significant period of time, the star will die and the cycle starts again.

The structure of carbonaceous cosmic dust can be difficult to elucidate. The structural complexity of a carbonaceous solid can be intricate, as carbon can exist in different classes of hybridisation, such as sp, sp^2 and sp^3.[24] Amorphous carbonaceous solids often contain a mixture of carbon in these different classes of hybridisation, which makes the structure of the dust grains difficult to extract. In addition, it is widely believed that the dust grains undergo extreme processing as they move from the circumstellar to the interstellar environment, meaning it is possible for their structures to evolve. The spectral features observed for cosmic dust grains often change from one environment to the next suggesting that the structure of the grains is changing considerably. Absorption and extinction spectroscopy are used to examine the cosmic dust grains. In particular, features corresponding to π-π^* electronic transitions associated with aromatic carbon can be observed in the ultra-violet (UV) region.[24] Infrared (IR) is also a useful tool in dust grain analysis. The presence of certain IR bands can help to identify the functional groups present within the grains. In particular, the presence of functional groups such as --CH_x, =C-H, -C=O, -C=C-, ≡C-H, -C≡C-, -C-O-C- and -C-OH can help astronomers to understand either the aromatic or aliphatic nature of the dust grains and aid in the prediction of the chemistry that can take place upon the surface of the dust particles.[10]

6.2.4 Gas-phase Condensation Reactions

As discussed above, it is agreed that the carbonaceous grains and siliceous grains are likely formed *via* gas-phase condensation in either carbon-rich or oxygen-rich stars respectively.[25] However, the exact condensation temperatures are not known. Jäger *et al.* used a mixture of laser ablation of graphite in quenching gas atmospheres and laser pyrolysis of hydrocarbons to simulate the gas-phase condensation of carbonaceous material under various conditions.[10] In these experiments by Jäger, laser ablation of graphite and subsequent condensation of carbonaceous material was carried out under He or He/H_2 quenching gases. A pulsed Nd:YAG laser was employed to evaporate carbon from a graphite surface with varying laser power densities from $2 \times 10^8 - 9 \times 10^9$ Wcm^{-2}.[10] A molecular beam technique was used to extract particles from the condensation zone. Simultaneously, the group also conducted laser-induced pyrolysis experiments to simulate the condensation of carbonaceous material using lower laser powers. Specifically, Jäger *et al.* used a pulsed or continuous wave (cw) CO_2 laser to prepare different carbon condensates through laser-induced pyrolysis of small hydrocarbons; ethylene, acetylene and benzene.[10] The carbon nanoparticles formed were either extracted using a particle beam or they were collected in a filter. The experiments were further divided into HT or LT (higher temperature or lower temperature) referring to the condensation temperature based upon the laser powers used.[26] Jäger *et al.* noted the formation of different structures under higher temperature conditions than under lower temperature conditions. In particular, when higher laser powers were used, corresponding to condensation temperatures of ≥3500 K, the condensate formed consisted of a mixture of fullerene-like soots and fullerenes. HRTEM images of the fullerene soot are shown in Figure 6.2, along with a possible structure for the fullerene-like product.[8] The soot particles were composed of strongly bent graphene layers with varying lengths and distances between the layers. Different condensation conditions corresponded to different levels of disorder within the carbonaceous solids. If the soot was produced in a high pressure He atmosphere (with no added hydrogen), then the soot formed consisted of more ordered cage structures and sometimes closed cage fullerenes. In the presence of a mixed He/H_2 atmosphere, the grains that formed were more disordered, with open cages held together by Van der Waals forces or linked by aliphatic chains.[10] The fullerenes are formed from initial polyyne chains, as previously predicted in a molecular dynamics simulation, which was confirmed by *in-situ* IR spectroscopy that indicated the presence of ≡CH and -C≡C- functional groups.[8,10,26]

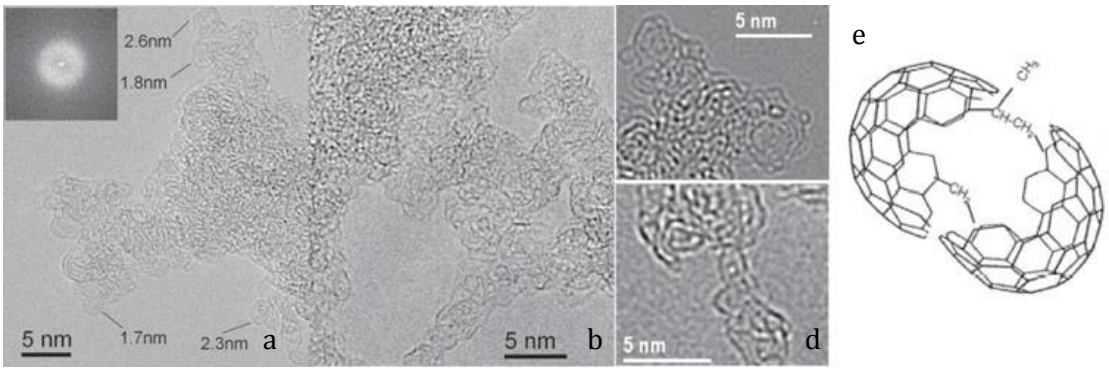

Figure 6.2: a)-d) HRTEM images of the condensate produced from high temperature (HT) laser ablation of graphite showing fullerene-like soots, e) possibly structure of the broken fullerene cage held together by aliphatic linkers. Taken from reference 8.

The LT laser induced pyrolysis experiments were carried out using laser powers corresponding to a condensation zone temperature of ≤1700 K and the condensates consisted of a mixture of Polycyclic Aromatic Hydrocarbons (PAHs) and soot, depending upon the laser power used. Approximately 65 PAHs were identified and particle growth was thought to proceed via condensation of large PAHs on the surface. [8]

This study by Jäger *et al.,* and further studies by the same group indicated that there were two completely different formation mechanisms involved under high or low temperature conditions, specifically the condensation of polyynes lead to the formation of fullerenes which then coagulated together to form larger particles, whereas under low temperature conditions nucleation proceeded *via* a PAH condensation route. No PAHs were detected under HT conditions. Therefore, condensation products in cool and hot astrophysical environments, for example cool and hot asymptotic giant branch stars or Wolf–Rayet stars should be different and should have distinct spectral properties.[19] Further studies by Jäger *et al.*, concluded that the absorption profile of buckyonion-like fullerenes produced by high power laser ablation of graphite showed good agreement with the observed interstellar absorption profile at 3.4 μm detected within the diffuse interstellar medium (Figure 6.3). This indicates that the buckyonions are viable astrochemical analogues for use in laboratory experiments.[24]

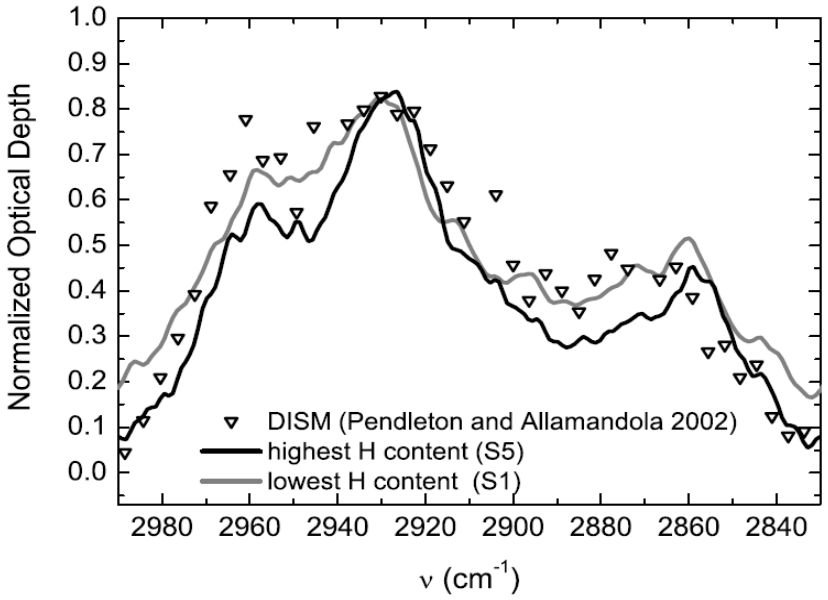

Figure 6.3: Spectra showing the comparison between the adsorption profile detected at 3.4 μm in the diffuse region of the ISM, with the absorption features of two fullerene-like condensates with different H content. Taken from reference 24.

The suggestion that the formation of dust grains could also take place in low temperature environments (such as the ISM) and not solely in AGB stars and supernovae, was first proposed to account for the fact that, despite a vast amount of destructive processing of the dust within the ISM, stardust was still detected in these regions.[19] These observations of refractory material (cosmic dust) within the ISM, suggests there must also be a low temperature pathway for the reformation of dust within the ISM. [19]Therefore, there must be reformation processes taking place within the ISM at a rate equal to, or greater than, the rate of destruction of cosmic dust. Although previous studies into the formation of silicates have proved that low temperature routes are viable pathways for the production of interstellar grains, there have been comparatively few studies into such low temperate formation of carbonaceous dust. Recently, Fulvio *et al.* and Krasnokutski *et al.* investigated low temperature condensation of carbon within the ISM.[19,26] Krasnokutski *et al.* used an Nd:YAG laser to vaporise a graphite target, which was mounted in bulk liquid helium and maintained at a temperature of approximately 1.7 K. The majority of fragments formed were C_3, which condensed inside the liquid helium and formed a precipitate at the bottom of the cryostat on TEM grids. The TEM grids were extracted and HRTEM was performed on the condensate. The structure of the carbonaceous material was found to be similar to the fullerene-like structures observed in previous experiments by Jäger *et al.* (discussed above) for high temperature condensation within AGB stars (≥3500 K).[8,26] Krasnokutski *et al.* also investigated the low temperature condensation of carbon in the presence of the most common

interstellar molecules present within dense regions of the ISM (H_2O, CO_2 and H_2) and noted the preferential formation of complex organic molecules (COMs). [26]

Fulvio *et al.* investigated the gas-phase condensation of carbon onto cold surfaces (maintained at a temperature of approximately 10 K), to represent remaining dust grains in the ISM.[19] An Nd:YAG laser was used to vaporise graphite pellet targets and the vaporised species were either condensed onto a KBr disk or isolated in an Ar matrix. Condensation onto the KBr disc allowed IR spectra to be taken under vacuum. The substrate was maintained at 10 K during condensation, then warmed in intervals so the structure of the new grains could be monitored with temperature and changes to the Mid-IR (MIR) spectra could be noted. The experimental set-up allowed MIR and UV transmittance spectra to be acquired from the substrate under vacuum. Fulvio *et al.* and Krasnokutski *et al*. both concluded that low temperature condensation of carbon into carbonaceous materials at approximately 10 K, is a barrierless process that should occur readily in the ISM.[19,26] These findings coincide with previous experiments investigating condensation reactions forming silicates at low temperatures in the ISM.[26] As the vaporised carbon materials reach the cold substrate they react together or with the substrate, to form carbonaceous refractory material. In experimental simulations of processing by VUV and cosmic ray radiation within the interstellar medium, the carbonaceous refractory material formed on the surface of the substrate was exposed to VUV radiation.[19] Partial degradation of the C-chains was observed, which lead to the reaction of the fragments to form fullerene-like solids similar to those observed in high temperature condensation reactions, at temperatures of approximately 3500 K.[19] The fragments also reacted with H_2O under VUV irradiation to form new precursor species: CO, C_3O and HCO.[19] Gradual heating of the surface lead to diffusion of these molecules, where they subsequently reacted together to form oligomers and eventually carbonaceous refractory material. Fullerene-like structures were detected among these materials, suggesting a formation pathway *via* long, branched carbon chains as predicted in higher temperature condensation experiments.[19]

In this chapter, the desorption characteristics of various molecules from a fullerene-like structure are investigated. The experiments previously discussed show that such onion-like structures are viable dust grain analogues. Fullerenes have been detected throughout the interstellar medium and as shown above, can form in multiple different environments via different pathways. It is therefore important to understand how gaseous species will interact with these new amorphous carbonaceous surfaces in cold and dense regions of interstellar space, where the gases will freeze out onto these surfaces as ices. To date, the desorption characteristics of gases from these types of surfaces have not yet been examined.

6.2.5 Desorption from Single Walled Carbon Nanotubes

The thermal desorption of gases from single walled carbon nanotubes (SWCNTs) has been previously examined and compared to the thermal desorption of the same gases from graphite.[27] SWCNTs are in some ways similar to the amorphous carbonaceous surface studied in this chapter. Both the fullerene-like soots and SWCNTs consist of sp^2 hybridised carbon sheets with high curvatures. Fullerenes are closed shell, spherical structures composed of interlocking heptagonal, hexagonal and pentagonal rings of carbon. SWCNTs are made of a graphene sheet bent into a cylindrical shape, hence they are composed of interlocking hexagonally arranged carbons. The interaction energies of oxygen, nitrogen, methane, xenon, carbon dioxide, methanol, ethanol, ammonia and water were studied on the surface of SWCNTs.[27] Prior to this literature study, each gas was first dosed onto graphite. Mass spectrometry coupled with temperature programmed desorption was used to analyse the gases as they desorbed from the surfaces. Comparison between the desorption of gases from graphite and the desorption of the same gases from SWCNTs revealed higher desorption temperatures and broader features in the TPD spectra.[27] The increase in broadness was attributed to stronger binding at higher coordinated sites/ higher energy sites and the possibility that the adsorbates may diffuse through the porous surface.[27]

As demonstrated above, the structure of the carbonaceous dust grain analogue can greatly affect the desorption characteristics of gases from the surface of the grain itself. Moreover, due to this discrepancy in binding behaviour, it is possible that the standard dust grain analogue used in the laboratory is an inaccurate representation of the properties of the dust grains present in the ISM. As with SWCNTs, one would expect enhanced binding to the surface of the fullerene-like solids, as there should be a number of higher coordinated sites/higher energy sites) available and the fullerenes or buckyonions are porous in nature.

In this chapter, the synthesis of the amorphous fullerene-like carbonaceous surfaces for desorption experiments, (henceforth known as the Amorphous Carbonaceous Surfaces (ACSs)) will be examined. Desorption profiles of various gases from ACSs will be compared to the desorption of the same gases from graphite.

6.2 Experimental

6.2.1 Formation of the Amorphous Carbonaceous Surfaces

The Amorphous Carbonaceous Surfaces were created by Dr Helen Kimber in collaboration with Dr Cornelia Jäger and the Max-Plank Institute for Astronomy at the Friedrich-Schiller-University in Jena, *via* the methods outlined in by Jager et al.[24] In this thesis, desorption characteristics of various gases from 2 surfaces are examined. The surfaces are the same, having been made under the same conditions (as discussed below) only with varying thicknesses. Initial experiments were

carried out on the thicker surface (ACS 1), while more recent studies have taken place on the thinner surface (ACS 2).

The experimental setup for the generation of the carbonaceous dust grains in shown in Figure 6.4. The apparatus consists of 3 differentially pumped stainless-steel high vacuum chambers, at base pressures of 1 x 10^{-6} Torr. The ablation target is housed in the ablation chamber. In the case of these experiments a ^{13}C target was used as it would allow for easier analysis of the degree of surface incorporation in later TPD experiments. The second harmonic of a pulsed Nd:YAG laser was used to ablate the surface of the carbonaceous target, with pulse lengths of 10 ns (250 mJ). As a result of the ablation of the surface of the target, a laser-induced plasma is generated above the target surface. As mentioned above, the temperature of this plasma was estimated to be approximately 4000 K, corresponding to the High Temperature condensation experiments carried out previously by the same group. The use of varying mixtures of He/H_2 as quenching gases have previously been investigated. The results of these investigations showed that the greater the hydrogen content of this gaseous mixture then the greater the incorporation of hydrogen into the condensed product. In the case of the formation of our ACSs, a quenching gas pressure of 10 Torr He was used, resulting in a low degree of hydrogenation in the grain analogues. A nozzle is fitted above the condensation zone, for extraction of particles into the expansion chamber. The skimmer is used to extract the particles from the expansion chamber into the deposition chamber. The particles are directed as a beam (1 cm OD) onto a 2x1 cm graphite surface. The quartz microbalance present within the deposition chamber is used to monitor the thickness of the deposit. In the case of the surfaces discussed in this chapter, the deposit on ACS 1 was 300 nm thick while the deposit on ACS 2 was 100 nm thick.

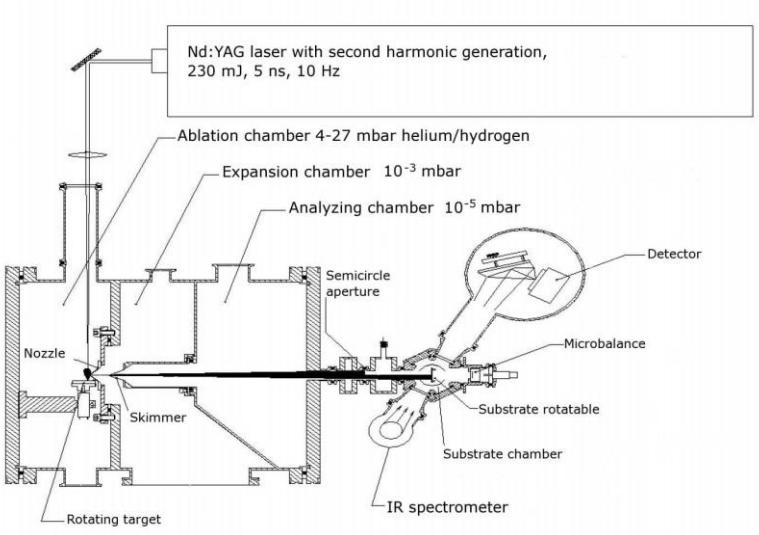

Figure 6.4: Schematic representation of the laser ablation experimental setup used by Dr Kimber and Dr Jäger. This was taken from reference 24.

For the purpose of characterisation, the experiment was repeated with deposition onto a KBr disc instead of graphite. Infrared spectroscopy (IR), Field Emission Scanning Electron Microscopy (FESEM) and High-Resolution Transmission Electron Microscopy (HRTEM) were performed on the surface. Analysis of the HRTEM and FESEM micrographs indicated that the surfaces are composed of dense agglomerates of very small carbon particles that are arranged in an amorphous porous manner on the graphite substrate. As with previous depositions, the structure of the carbon particles is referred to as "fullerene-like", as they consist of strongly bent graphite sheets arranged in symmetrical, or elongated fullerene cages. The cages may be complete closed shell cages or they may be broken and held together by aliphatic linkers or Van der Waals forces. IR spectroscopy was used to confirm the presence of the aliphatic linkers, as bands ranging from 2600 cm^{-1} to 3000 cm^{-1} was observed, which are consistent with C-H stretching.

5.2.2 Temperature Programmed Desorption Experiments of Deposition on the Amorphous Carbonaceous Surfaces

The ACSs were each separately inserted into the Cosmic Dust Apparatus previously described in Chapter 2 (Figure 6.5). Once inside the ultra-high vacuum chamber the surface was heated to 450 K for 90 mins for cleaning. It was necessary to heat the surface to such a high temperature as it was exposed to air *en route*. IR studies revealed an absorption at 1725 cm^{-1} after the sample was first removed from the vacuum chamber in Jena, which was indicative of C=O bonds. Previous work at Jena involved studies into reducing the carbonyl absorption and found that heating to 450 K significantly lowered the intensity of this band.[28] Therefore, it was logical that a similar temperature was needed in order to clean the surface of oxygen bonds formed in the Cosmic Dust experiment. This cleaning process was repeated for ACS 2 when ACS 1 had been removed.

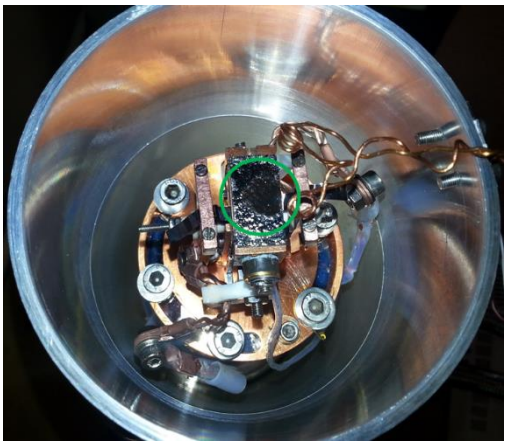

Figure 6.5: Image of the ACS 1 mounted at the end of the coldhead prior to insertion into the Cosmic Dust Apparatus. The green circle is highlighting the area where the amorphous soot was deposited on the graphite surface, it is the slightly darker area within the highlighted area.

After cleaning, various different gases were dosed onto the ACS to investigate the desorption. Initial investigations were focussed on the desorption CO_2 from ACS 1 at 19 K dosing temperature. The flux of CO_2 gas was 4.2 x 10^{12} molecules cm^{-2} s^{-1}. Each gas was separately dosed onto the surface for a specific length of time. After the dosing period was complete, the surface was linearly heated at 10 K min^{-1} in a TPD experiment (as discussed in Chapter 2), and the desorbing species were detected using the QMS. The combination of temperature data and QMS data facilitated the generation of a TPD spectrum, showing the temperature range over-which the molecule desorbs as well as indicating the surface interactions of the gas with the ACS. The desorption of gases from an amorphous carbonaceous surface were also investigated with ACS 2 using the same method. In particular, the desorption characteristics of molecular oxygen and acrolein were examined, with dosing fluxes of 8.3 x 10^{12} and 10.4 x 10^{12} molecules cm^{-2} s^{-1} respectively.

6.3 Results and Discussion

6.3.1 Desorption of gases from the ACS 1

Carbon dioxide was dosed onto the first amorphous carbonaceous surface (ACS 1) at 19 K. The desorption spectra various doses of CO_2 from this novel surface are shown in Figure 6.6.

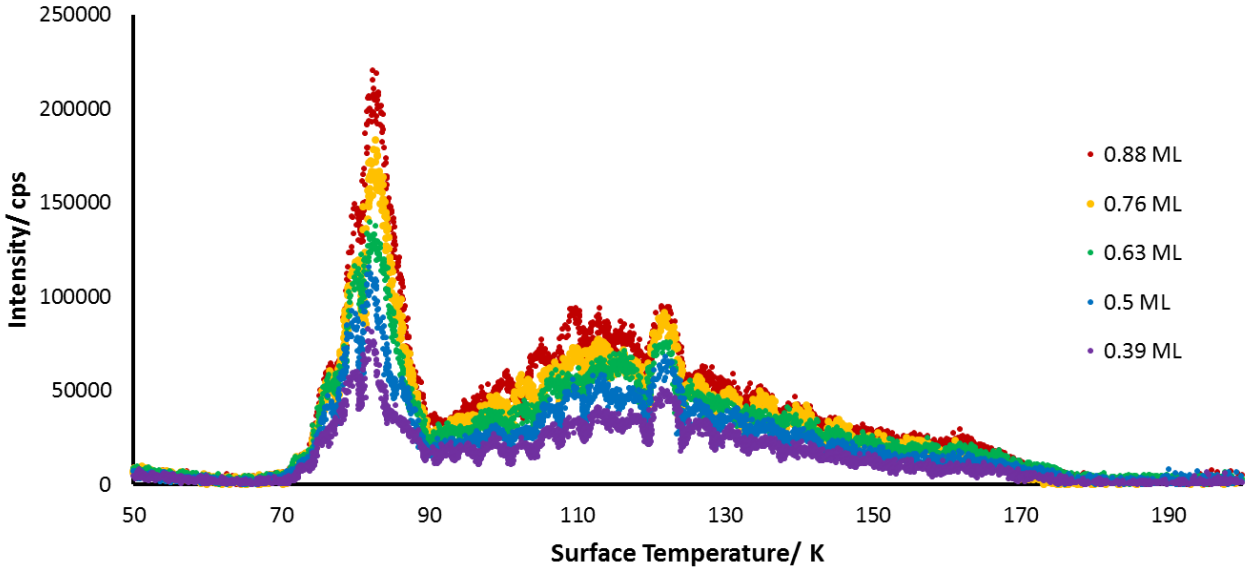

Figure 6.6: Desorption spectra of increasing doses of carbon dioxide from ACS1 held at 19K. Oscillations can be observed throughout the entire spectrum.

The spectral data outlined in Figure 6.6, show that CO_2 exhibits two distinct desorption behaviours from the amorphous surface. A peak (Peak 1) is observed at 82 K, while another broad peak is observed at approximately 118 K (Peak 2). This second peak is not observed for the desorption of carbon dioxide from a graphitic surface, and the assignment and relevance of this peak will be discussed later in the Chapter.

A large number of fluctuations across the temperature range can be observed in the spectral data shown in Figure 6.6. This is due to the fact that the initial investigations into the amorphous carbonaceous surface were conducted prior to the installation of the new heating block, which is outlined in Chapter 2. As stated in Chapter 2, feedback from the heater caused small oscillations in the heating ramp, which in turn caused oscillations in the TPD profiles. The desorption spectra of other species (O_2 and Ar) also showed similar fluctuations so their desorption profiles are not shown. The spectra from experiments with the old heating apparatus were difficult to analyse, owing to the inherent inaccuracy of the data. Therefore, adjustments were made to the heating unit (see Chapter 2) before any desorption investigations were carried out on ACS2.

6.3.2 Desorption of gases from the ACS 2

The desorption profile of oxygen and acrolein from ACS2 were investigated as discussed above. Oxygen and acrolein were dosed in separate experiments, for various different lengths of time, ranging from 2 minutes to 10 minutes. During the TPD experiment masses of m/z 32 and m/z 56 were monitored, corresponding to oxygen and acrolein respectively.

Desorption of Oxygen

The desorption profile of oxygen from the ACS 2 is shown in Figure 6.7a. As previously mentioned in Chapter 2, slight variations in the heating rate can cause artefacts in the TPD spectra. Many of the features that could be construed as peaks are likely a result of this heating rate issue, however at this time, it is currently impossible to tell which features are legitimate peaks. As a result, the data was fitted to Lorentzian curves, assuming only two major desorption features. The fitting of the lowest dose of oxygen (2 mins) is shown in Figure 6.7b. As can be seen from the Figure 6.7b, the first desorption peak for oxygen is observed at approximately 37 K (Peak 1) , while the second feature is observed at approximately 60 K (Peak 2). As can be seen from the spectra in Figure 6.7c, Peak 2 is a broad desorption peak, with the peak shifting from higher temperatures (60 K), to lower temperatures (50 K) with increasing dose.

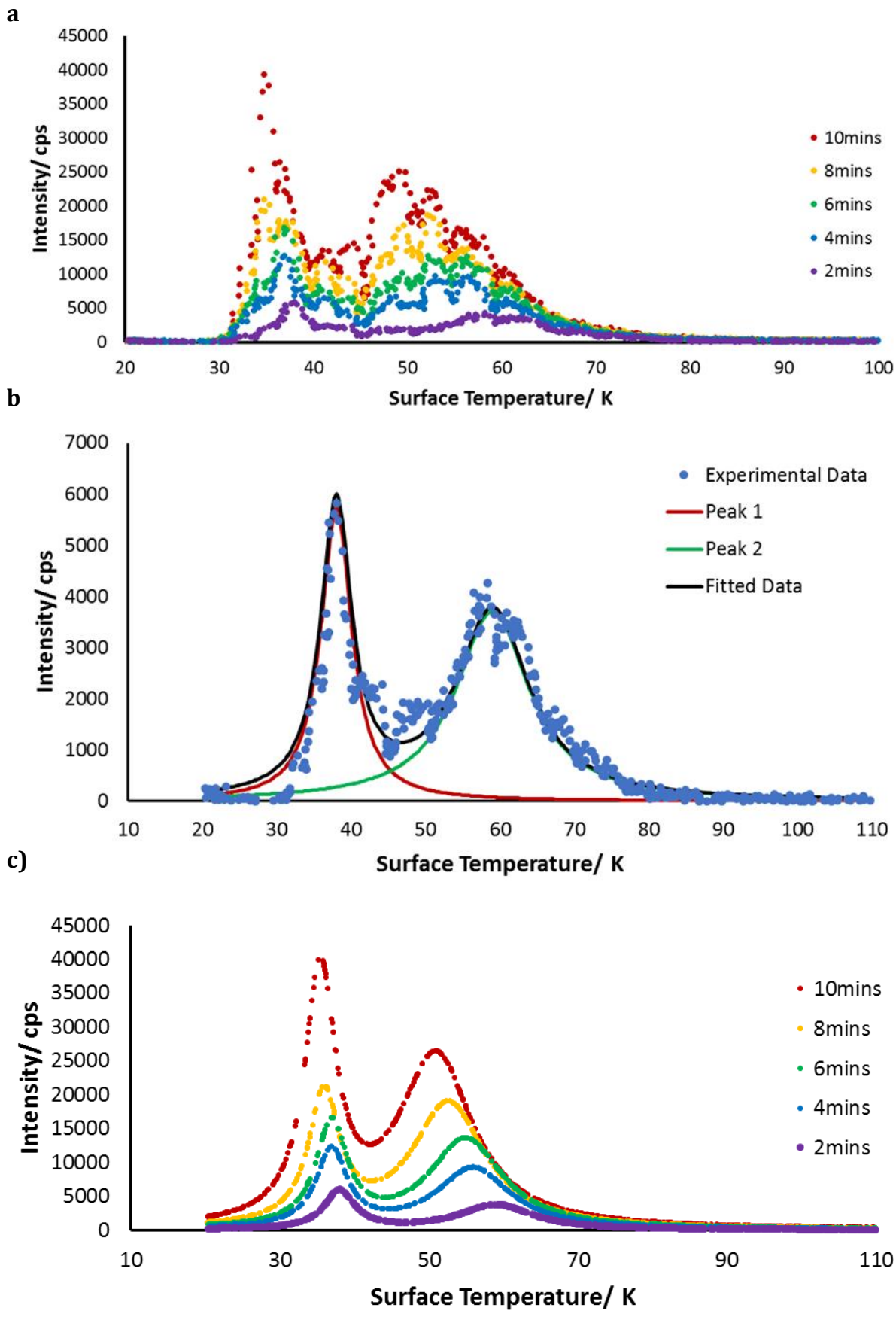

Figure 6.7: a) The experimental data for the desorption of oxygen from ACS2. The desorption profile contains many artefacts from the heating rate, b) fitting of the desorption profile for the 2 minute dose of oxygen on ACS 2 showing 2 major desorption environments, c) the fitted data for the desorption of oxygen from the amorphous carbonaceous surface.

Examination of Peak 1 highlights that the lower temperature desorption peak shifts to lower temperatures with increasing dose. Traditionally, this temperature shift is when sub monolayer doses of a species have been deposited on the surface. When the monolayer is complete the peak temperature will stop shifting to lower temperatures. The occurrence of multilayer desorption is deduced when the temperature of the peak once again shifts to higher temperatures, with profile of each dose now sharing a leading edge, as described in Chapter 2. From the data shown in Figure 6.7, it is clear that the desorption of O_2 from the ACS 2 dose not reach multilayer ice coverages. This is converse to what was observed when the same flux of O_2 was previously dosed on a graphite surface, where the first monolayer was completed within 4 mins.

A desorption spectrum of O_2 from graphite and ACS 2 are compared in Figure 6.8a. This figure highlights that desorption from a graphitic surface takes place from approximately 20-50 K, whereas desorption from the amorphous surface occurs between 30- 80 K. Hence, O_2 is observed to remain on the ACS until much higher temperatures than on graphite. The desorption profiles from the research of Ulbricht *et al.* into the desorption of various gases from carbon nanotubes are shown in Figure 6.8b.[31] The figure shows enhanced binding to the carbon nanotube surfaces, where the gases remains adsorbed onto the surface until higher temperatures than previously observed for graphite, which is consistent with the relationship observed in this work and highlighted in Figure 6.8a.

a)

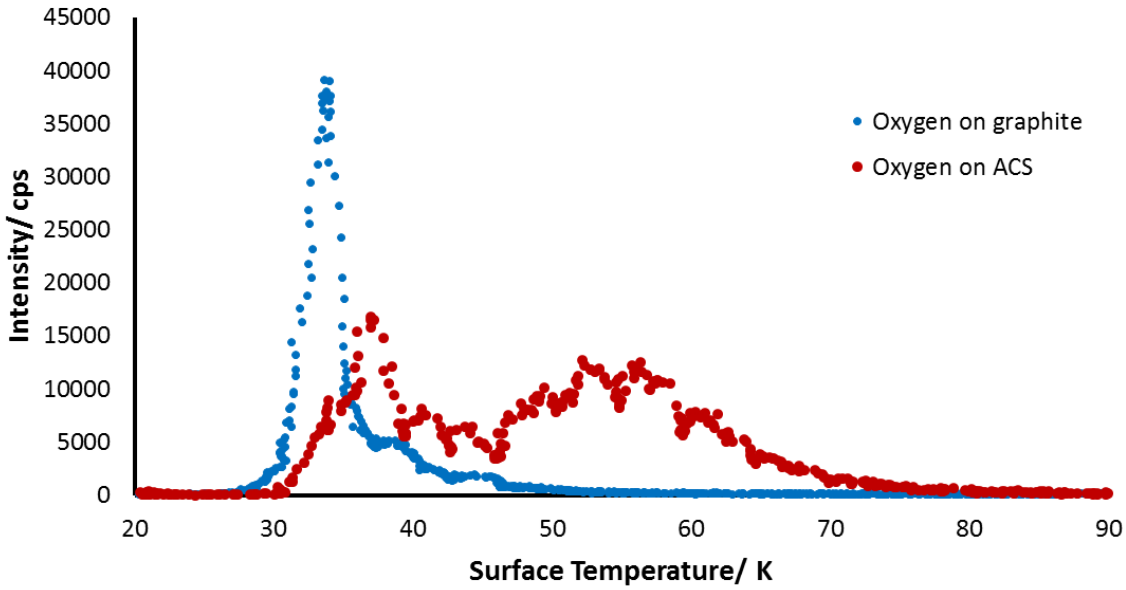

b)

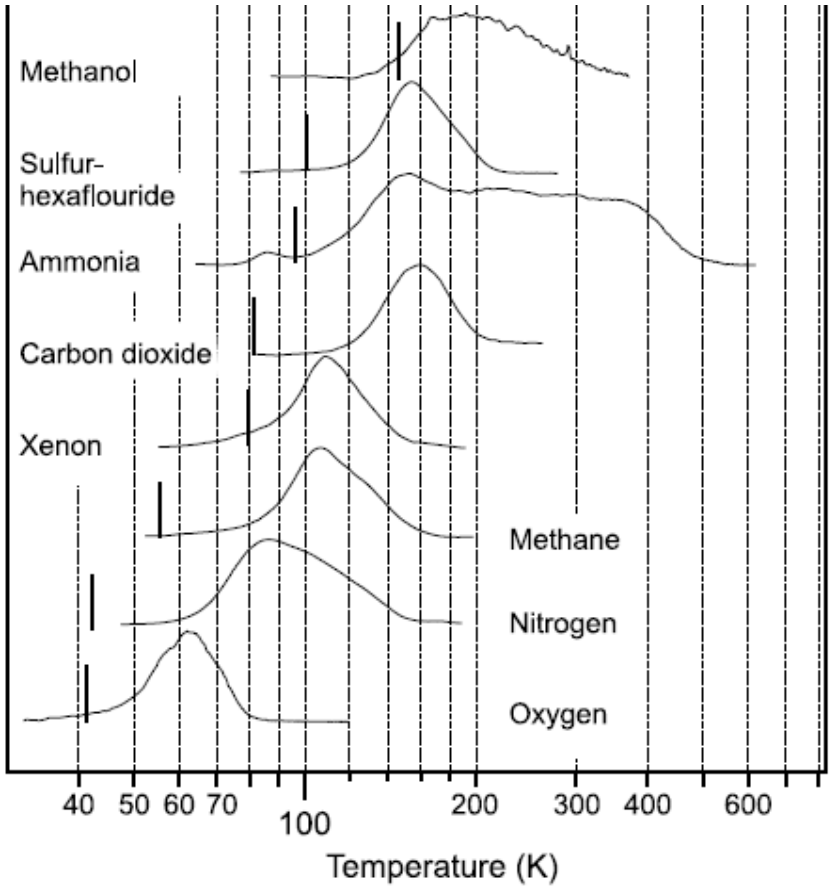

Figure 6.8: a) Spectra showing the desorption profile of oxygen from graphite (blue) and from the ACS (red), b) Spectra taken from reference 31, showing the desorption profiles of various gases from SWCNTs, including oxygen. Desorption profiles shows the gases are still adsorbed onto the surface of the nanotubes at temperatures much higher than on graphite (black line).

The Peak 2 fitted data for the desorption of O_2 from the ACS is shown in Figure 6.9. Peak 2 is a broad desorption peak, which shifts from higher temperatures (60 K) to lower temperatures (50 K) with increasing dose. The transition from monolayer to multilayer desorption of O_2 is also not observed for this higher temperature peak. This indicates that the peak is representative of submonolayer coverages. Increasing the dose as high at 60 mins, which would represent a coverage of 15 ML on the graphitic surface still did not result in the saturation of Peak 1 or Peak 2. This suggests that the surface area of the amorphous carbonaceous surface is much greater than that of graphite, which is to be expected, since the ACS is porous owing to the presence of the cage-like structures.

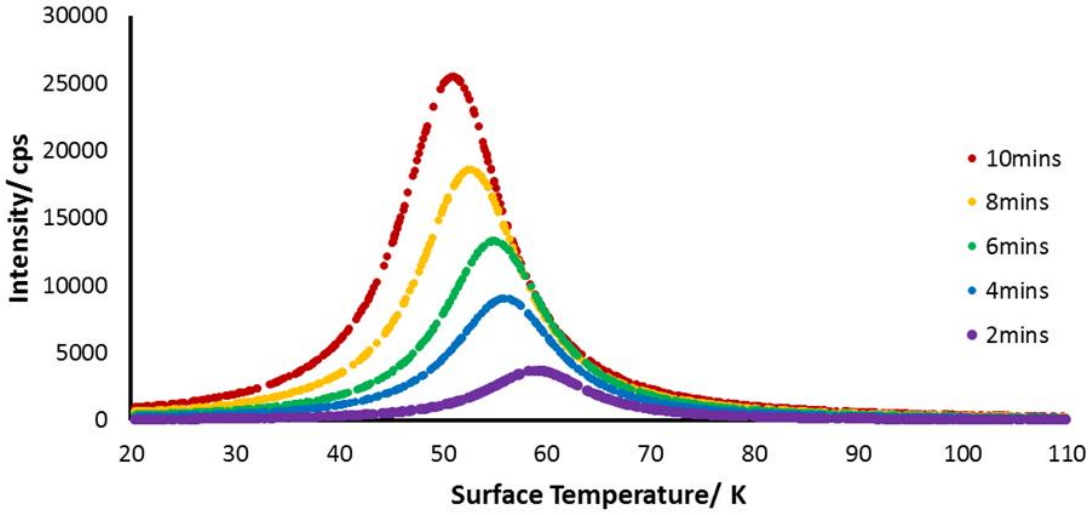

Figure 6.9: Fitted desorption spectra of oxygen desorption form the amorphous carbonaceous surface, showing Peak 2 data. The peak temperature shifts to lower temperatures with increasing dose.

Desorption of Acrolein

The TPD profiles for the desorption of different doses of acrolein on ACS 2 can be seen in Figure 6.10. The experimental data was also fitted to allow for better data analysis and an example of the fitting is shown in Figure 6.10b. The fitted desorption profiles are highlighted in Figure 6.10c. Analysis of figure 6.10, shows that there are two desorption environments for the desorption of acrolein from the ACS 2. The first peak (Peak 1) is actually a double peak at 132 K and 140 K. The intensity of these peaks both increase with longer dosing. The second peak (peak 2) is a broad peak observed at 217 K. An increase in dose causes the intensity of Peak 2 to increase while shifting to lower temperatures.

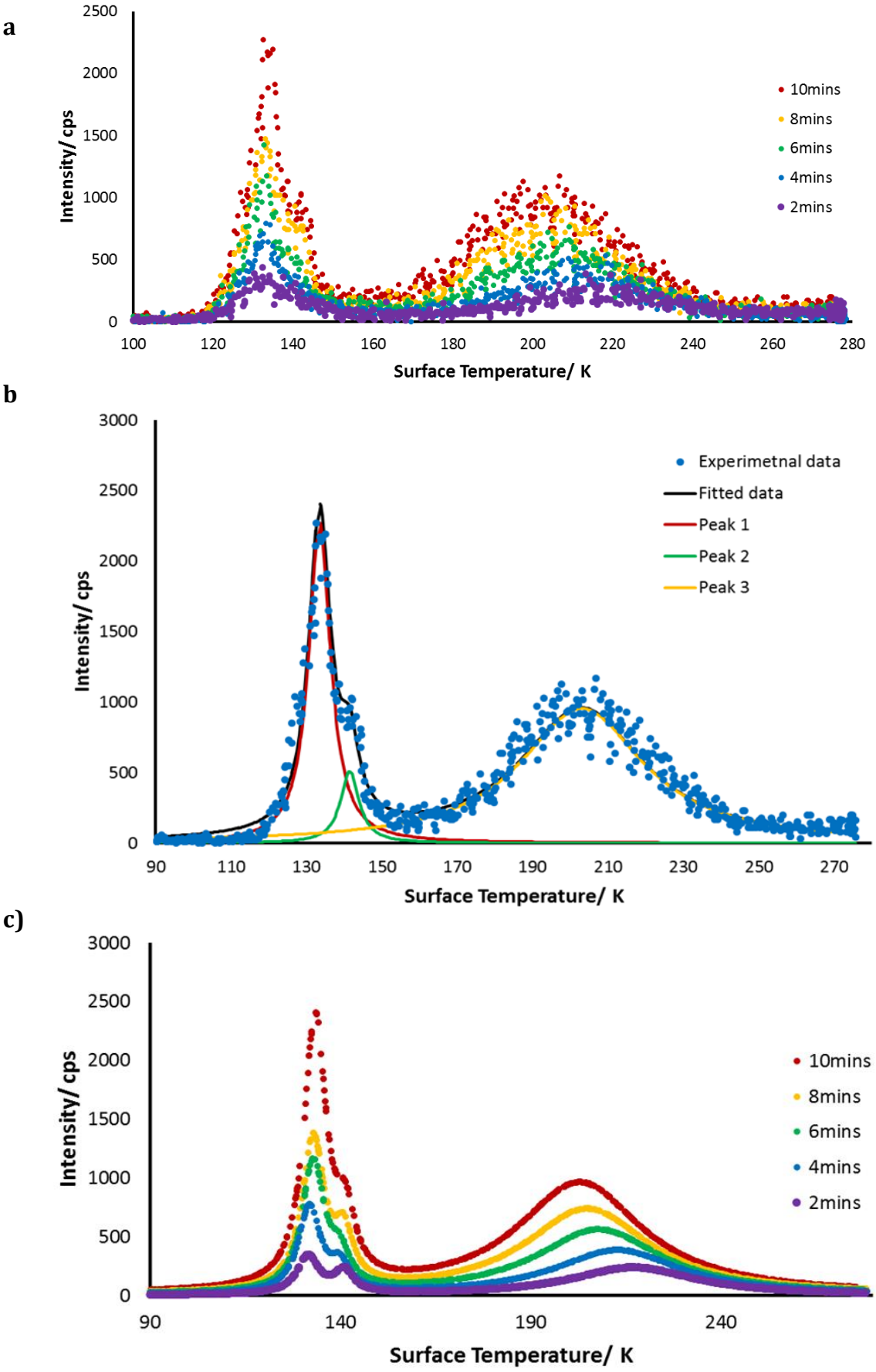

Figure 6.10: a) The experimental data for the desorption of acrolein from ACS 2 at 19K with increasing dose b) fitting of the desorption profile for the 2 minute dose of acrolein on ACS 2 showing 2 major desorption environments, c) the fitted data for the desorption of acrolein from the amorphous carbonaceous surface.

As previously observed for the desorption of oxygen from ACS 2, and the desorption of carbon dioxide from ACS1, we can see that the lower temperature desorption features for acrolein do not saturate with increasing dose. As mentioned above, this indicated that even at high doses, sub monolayer ices are still being formed.

A desorption spectrum of acrolein from graphite and ACS 2 are compared in Figure 6.11. The organic molecule desorbs from graphite from 120-160 K, whereas desorption from the amorphous surface occurs between 120- 260 K. This highlights a distinctly large increase in the residence time of acrolein on the amorphous surface compared to its time on graphite.

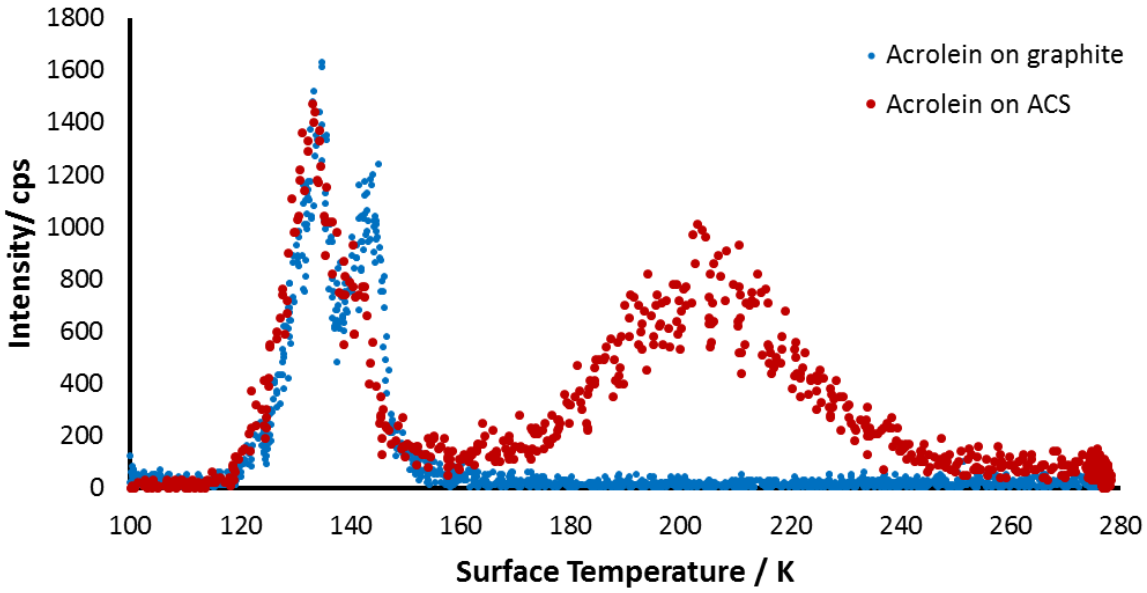

Figure 6.11: Spectra showing the desorption profile of acrolein from graphite (blue) and from the ACS (red).

As Figure 6.11 shows, Peak 2 is an acrolein desorption feature that is unique to the amorphous carbonaceous surface. This high temperature peak is examined in greater detail in Figure 6.12, which shows the fitted Peak 2 data. This higher temperature peak shifts to lower temperatures with increasing dose, as observed for the desorption of O_2 from ACS2. Again, this peak cannot be saturated with increasing dose, indicating that ices are still desorbing from sub-monolayer coverages.

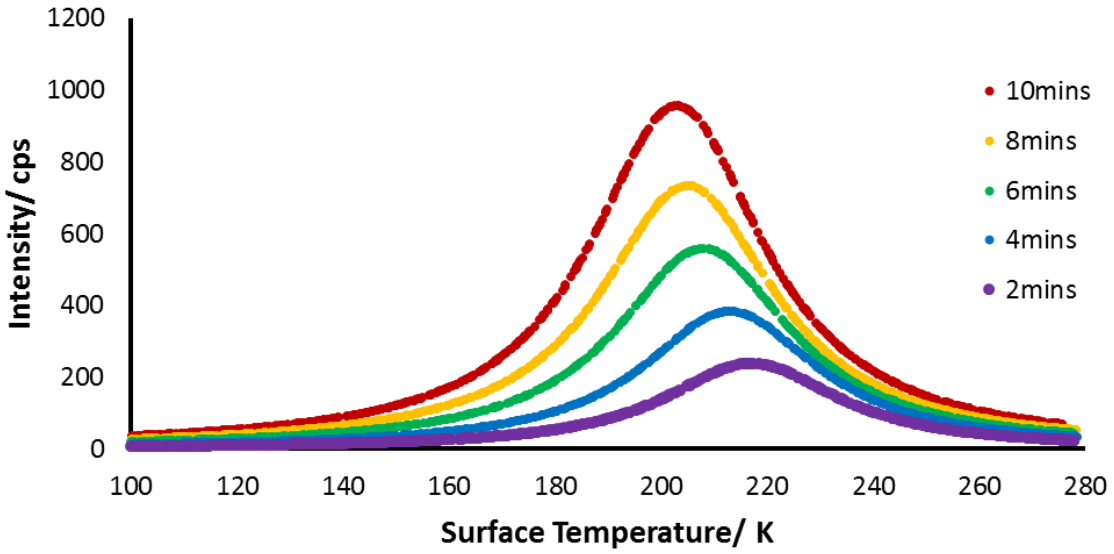

Figure 6.12: Fitted desorption spectra of acrolein desorption form the amorphous carbonaceous surface, showing Peak 2 data. The peak temperature shifts to lower temperatures with increasing dose.

6.3.3 Discussion

As mentioned in Section 6.2.2, the amorphous carbonaceous surfaces consist of a small amorphous deposit on a 1 x 2 cm graphite substrate. Analysis and comparison of the desorption characteristics of the adsorbed ices is complicated by the presence of a graphitic underlying surface. As observed for the desorption of CO_2, O_2 and acrolein from the ACSs, all the spectra contain a low temperature peak whose position is in relatively good agreement with the desorption of the same gas from graphite. Therefore, it is unclear whether these low temperature peaks observed in the spectra are from the amorphous disk or the surrounding graphitic area. However, our inability to saturate this low temperature peak, even at high exposures, suggests that the feature is from the amorphous carbonaceous surface, indicating that desorption is indeed occurring from two different sites. However, in this chapter we will mainly discuss the high temperature desorption peaks observed for all three species, as this desorption behaviour is unique to the new dust grain analogues, and temperature to which all three gases can still be adsorbed on the surfaces is greatly increased compared to graphite.

As was observed in the TPD profiles of the adsorbates, the position of the broad, higher temperature peak was shifted more to high temperature for lower doses of each species. Higher doses caused the peak to shift towards lower temperatures. As the ACS is not crystalline, there

are a distribution of binding sites available on the substrate. As our surfaces are amorphous and porous, there are even more binding sites available than would be on a graphite surface. The binding sites have different binding energies and if they are provided with enough thermal energy, the adsorbed molecules will diffuse across the surface to occupy the highest energy binding sites, which are more energetically favourable. Hence, there will be a peak in the high temperature tail of the TPD spectrum.[29,30] As the dosing period increases, more molecules are deposited on the surface. The highest energy binding sites will fill up, so molecules will then bind to lower energy binding sites, until this too is filled and they must bind to even lower energy sites. The lower the energy of the binding site, then the easier it will be to break the weak bond between the adsorbate and the substrate. Subsequently, at higher doses, desorption will begin to occur at lower temperatures.

The observation of this shift towards lower temperature with increasing dose on the ACS suggests there are a number of different energy binding sites available for each species. In particular, the presence of the high temperature peak in the desorption profiles from the ACS can be attributed to significantly higher and stronger binding energies than observed on graphite. This is in good agreement with Ulbricht *et al.* who investigated the desorption of a range of molecules from a graphite surface and a SWCNT.[27] Ulbricht *et al.* noticed that the desorption features of each species (except water) from the SWCNT were significantly broadened and shifted to higher temperatures. They referred to this observation as "delayed desorption" which occurred due to the presence of stronger binding energies on the SWCNT as well as the porosity of the surface.[27]

Additionally, Ulbricht *et al.,* modelled the desorption of O_2 from graphite and the SWCNT to ensure that the high temperature peak was not the result of chemisorption of the adsorbate onto the substrate.[31] The binding energy for the physisorption of oxygen to graphite was predicted to be 8.1 kJ mol^{-1}, whereas the binding energies of oxygen to SWCNTs was found to range from 12.9-15.4 kJ mol^{-1} depending on the type of site occupied and the orientation of the molecule to the surface. O_2 desorbs from the SWCNT in these experiments from 45- 80K, which is in excellent agreement with the desorption range we observe for the high energy peak of O_2. It is therefore highly unlikely that the high temperature desorption peaks we observed in our TPD profiles are due to the chemisorption of the species. This is further confirmed by the work of Vijayakrishnan *et al.* who used photoelectron spectroscopy to investigate the chemisorption of molecular oxygen to a C_{60} surface.[32] They concluded that the chemisorption of O_2 onto C_{60} does not occur at temperature below 200 K. As mentioned previously, the position of our high temperature peak for O_2 ranges from 60- 50 K; temperatures that are too low to coincide with chemisorption.

No studies have currently been conducted into the desorption of acrolein from the surface of a fullerene like structure. However, the detection of the "delayed" desorption peak at higher temperatures, similar to that of oxygen indicates the presence of higher energy binding sites for acrolein on the more amorphous surface than previously observed for graphite.

6.4: Astrophysical Implications

Analysis of the desorption spectra of a number of different species from our novel amorphous carbonaceous surfaces has demonstrated the presence of higher energy binding sites on the surface than has previously been observed on the standard dust grain analogue. The presence of the higher energy sites indicates for surfaces of a similar amorphous broken fullerene like structure, molecules will bind to the surfaces with high binding energies and longer residence times at higher temperatures.

The binding energies of molecular species to the dust grains in the interstellar medium is an important tool used by astronomers to estimate the stellar mass of young stars. The mass of a newly formed star is related to the efficiency with which it heats its surroundings.[33] Information is extracted about the temperature of the interstellar gas and dust in a particular region through examination of the "snow lines". A snow line is the radial distance from a heat source, at which the molecules will sublime from the surface of the grains into the gas-phase.[33] When a young star is formed, it heats up the gas and dust molecules closest to it through the emission of UV radiation. The efficiency of the heating process can be related to the timescale of the formation of the star, which in turn allows stellar mass to be estimated. The molecules closest to the star absorb the ultra-violet radiation and emit it in the IR. The infrared radiation from the molecules will act as a secondary heat source, heating the gas molecules and grains closest to them. The closer the particles are to the heat source, the more they will heat up. Likewise, particles that are further away from the source, will be cooler. As a result, the temperature of the dust grains and gas molecules are dependent upon this radial distance from the young star.[33] If the binding energy of a molecule to the surface of the dust grains is known, then the temperature of the interstellar environment at these snow lines can be estimated.

In our experiments we observe the presence of higher energy binding sites on the amorphous surfaces. If the structure of the dust grains are similar to our grain analogue in the regions surrounding these young stellar objects then the estimation of the astronomers about the environmental conditions they are observing could be in error. Higher energy binding sites mean

the molecules will remain on the surface at a certain temperature for longer residence times than previously observed for graphite therefore the snow line of that molecule will be a different distance away from the young stellar object than previously estimated.

6.5 Summary

In this chapter, the concept of using more amorphous carbonaceous dust grain analogues in laboratory experiments simulating interstellar reactions, was introduced. The surfaces of the interstellar dust grains are unlikely to be as uniform as graphite, which is the most commonly used dust grain analogue. Therefore, in this chapter, the desorption profiles of oxygen and acrolein from a novel amorphous carbonaceous dust grain analogue were examined and compared to the desorption of the same molecule from graphite. The amorphous carbonaceous surfaces used in this study were manufactured in collaboration with Dr Cornelia Jager in Jena, and they can be described as low hydrogen, amorphous carbonaceous surfaces that consist of broken fullerene like cages. The probability of surfaces with a similar structure to the ACSs being formed in the interstellar medium was reviewed.

Analysis of the desorption profiles of both acrolein and oxygen (as well as CO_2 to the extent that the quality of data allowed) showed the presence of high energy binding sites on the ACSs. This is consistent with the desorption characteristics observed for various gases including oxygen from SWCNT by Ulbricht *et al*. The presence of these higher energy sites indicates that molecules can remain physisorbed to a more amorphous surface up to higher temperatures than have previously been modelled for graphite. An adjustment to the binding energies means that astronomers may need to update their interstellar models to better understand the interstellar environment around young stars.

6.6 References

1 M. Minissale, E. Congiu and F. Dulieu, *Astron. Astrophys.*, 2016, **585**, A146.

2 M. P. Collings, M. A. Anderson, R. Chen, J. W. Dever, S. Viti, D. A. Williams and M. R. S. McCoustra, *Mon. Not. R. Astron. Soc.*, 2004, **354**, 1133–1140.

3 E. A. Bergin and M. Tafalla, *Astron. Astrophys. Rev.*, 2007, **45**, 339–396.

4 A. Potapov, C. Jäger, T. Henning, M. Jonusas and L. Krim, *Astrophys. J.*, 2017, **846**, 131.

5 E. Herbst, *Phys. Chem. Chem. Phys.*, 2014, **16**, 3344–59.

6 B. T. Draine, *Annu. Rev. Astron. Astrophys.* 2003, **41**, 241-89.

7 B. T. Draine, *Astrophys. J.*, 2016, **831**, 109.

8 C. Jäger, H. Mutschke, T. Henning and F. Huisken, *EAS Publ. Ser.*, 2011, **46**, 293–304.

9 D. Fulvio, S. Góbi, C. Jäger, Á. Kereszturi and T. Henning, *Astrophys. J. Suppl. Ser.*, 2017, **233**, 14.

10 C. Jäger, H. Mutschke, I. Llamas-Jansa, T. Henning and F. Huisken, *Proc. Int. Astron. Union*, 2008, **4**, 425–432.

11 A. Sakata, S. Wada, Y. Okutsu, H. Shintani and Y. Nakada, *Nature*, 1993, **301**, 493.

12 A. T. Tokunaga and S. Wada, *Adv. Space Res.*, 1997, **19**, 1009–17.

13 H. W. Kroto, J. R. Heath, S. C. O'Brien, R. F. Curl and R. E. Smalley, *Nature*, 1985, **318**, 612.

14 E. K. Campbell and J. P. Maier, *J. Chem. Phys.*, 2017, **146**, 160901.

15 A. C. Brieva, R. Gredel, C. Jäger, F. Huisken and T. Henning, *Astrophys. J.*, 2016, **826**, 122.

16 H. W. Kroto and M. Jura, *Astron. Astrophys.*, 1992, **263**, 275–280.

17 D. Strelnikov, B. Kern and M. M. Kappes, *Astron. Astrophys.*, 2015, **584**, A55.

18 L. Gan, D. Yang, Q. Zhang and H. Huang, *Adv. Mater.*, 2010, **22**, 1498–1507.

19 D. Fulvio, S. Góbi, C. Jäger, Á. Kereszturi and T. Henning, *Astrophys. J. Suppl. Ser.*, 2017, **233**, 14.

20 O. Berné, N. L. J. Cox, G. Mulas and C. Joblin, *Astron. Astrophys.,* 2017, **1**, 4–9.

21 E. K. Campbell, M. Holz and J. P. Maier, *Astrophys. J. Lett.*, 2016, **826**, L4..

22 O. Berné, N. L. J. Cox, G. Mulas and C. Joblin, *Astron. Astrophys.*, 2017, **1**, 4–9.

23 J. Lequeux, *Birth, Evolution and Death of Stars*, World Scientific Publishing Co. Pte. Ltd., London, 2013.

24 C. Jäger, H. Mutschke, T. Henning and F. Huisken, *Astrophys. J.*, 2008, **689**, 249–259.

25 A. W. Blain, F. Combes and B. T. Draine, *The Cold Universe: Saas-Free Advanced Course*, Springer-Verlag, Berlin, 2004.

26 S. A. Krasnokutski, M. Goulart, E. B. Gordon, A. Ritsch, C. Jäger, M. Rastogi, W. Salvenmoser, T. Henning and P. Scheier, *Astrophys. J.*, 2017, **847**, 89.

27 H. Ulbricht, R. Zacharia, N. Cindir and T. Hertel, *Carbon N. Y.*, 2006, **44**, 2931–2942.

28 C. Jäger, F. Huisken, H. Mutschke, I. L. Jansa and T. Henning, *Astrophys. J.*, 2009, **696**, 706–712.

29 J. A. Noble, E. Congiu, F. Dulieu and H. J. Fraser, *Mon. Not. R. Astron. Soc.*, 2012, **421**, 768–779.

30 L. Amiaud, F. Dulieu, J. H. Fillion, A. Momeni and J. L. Lemaire, *J. Chem. Phys.*, 2007, **127**, 144709.

31 H. Ulbricht, G. Moos and T. Hertel, *Phys. Rev. B.*, 2002, **66**, 075404-075411.

32 V. Vijiayakrishnan, A. K. Santra, T. Pradeep, R. Seshadri, R. Nagarajan and C. N. R. Rao, *J. Chem. Soc. Commun.*, 1992, 198–199.

33 D. A. Williams, W. A. Brown, S. D. Price, J. M. C. Rawlings and S. Viti, *Astron. Geophys.*, 2007, **48**, 25–34.

Chapter 7: The Interaction and Reaction of Propene with Atomic Oxygen on Different Dust Grain Analogues

7.1 Overview

In this chapter, previous studies into the interaction of propene with various surfaces will be reviewed and the relevance of propene in the interstellar medium will be discussed. The desorption characteristics of propene from a graphitic surface and the hybrid amorphous carbonaceous surface will be compared. The reaction of propene with atomic oxygen upon the amorphous surface will also be investigated and preliminary data will be discussed.

7.2 Introduction

As mentioned in previous Chapters, there is a rich chemistry taking place within the dense clouds of the interstellar medium. Within these regions, the dust grains and icy mantles that form upon them, are shielded from the high energy photons which permeate more diffuse clouds.[1,2] The opacity of these dense regions allows for the formation of complex organics molecules (COMs) as well as ensuring that the lifetimes of the molecules are extended.

The mechanisms through which the complex organic species form are of great interest, as they can help us to understand the conditions of interstellar space, as well the origins of our own solar system and the molecules therein. Over 200 molecules have been detected within the ISM to date. The observed molecular abundances for many of these cannot wholly be accounted for by considering formation route involving gas-phase chemistry.[3] Therefore, it is widely believed that surfaces play a vital role in the chemistry taking place within the interstellar medium, as previously discussed (Chapter 1), acting not just as molecular sinks upon which gas species can freeze out (in cold regions) but also helping to bring molecules and atoms together to react. Reactions of unsaturated complex molecules such as propene can help to account for the observed molecular complexity within the dense clouds of the ISM. In this chapter, the desorption characteristics of propene from astrochemically relevant surfaces will be examined as will the reaction between propene and atomic oxygen on surfaces.

Propene was first detected in the dark Taurus Molecular Cloud (TMC-1) in 2007 with an abundance of 4 x 10^{-9} relative to H_2.[4] It has since also been detected in additional dense clouds Lupus-1A, L1495B, L1521F and Serpens South with an average abundance of 2 x 10^{-9} relative to H_2. Gas phase routes are unable to account for the amount of propene observed, meaning the formation of propene must also take place on the surface of the interstellar dust grains.[5] Hickson *et al.* investigated the formation of methylacetylene and propene in cold dense clouds and concluded that the surface reactions likely proceed through the successive hydrogenation of C_3 molecules.[5] Qasim *et al.* also found propene to be the product of the successful surface reaction between propyne and atomic hydrogen under interstellar conditions. [6] This represents another viable synthetic route for the production of propene within the ISM, as propyne has also been detected in TMC-1 with a column density of 4-8 x 10^{13} cm^{-2}.[6]

The desorption characteristics of short chain unsaturated hydrocarbons from various surfaces have been thoroughly investigated. Specifically, the desorption of alkenes from metallic surfaces is of particular interest owing to their importance in industrial processes such as dehydrogenation, isomerisation and cracking reactions.[7,8] The desorption characteristics of propene have been widely studied; propene desorption has been investigated from Ag (111), Ag (110), Au (111), Au (100), Ni (100), TiO_2 (110) and Cu_2O (111 and 110) surfaces.[7–12] However, the experiments conducted in these previous studies all dose propene onto the surfaces at deposition temperatures >100 K to avoid condensation as highlighted by Kleyna *et al.*[9] The experiments on the transition metals aimed to investigate the chemisorption of propene to metallic surfaces, through the formation of weak π bonds. As mentioned in Chapter 1, the dust grains within the ISM are largely made of amorphous silicates and carbonaceous material. The molecular species are physisorbed onto the grains and so exhibit different desorption characteristics to those observed for their desorption from the metallic surfaces. Dinger *et al.* investigated the reactions of gaseous H atoms with propylene oxide on a Pt(111) surface covered with a thin layer of graphite.[13] The desorption profile of the molecules from this graphite covered surface should be in better agreement with the conditions of the ISM, as the layer of unreactive carbon shields the adsorbates from the influence of the metal ions.[13] In their study, Dinger *et al.* noted the desorption of propene from the C/Pt(111) surface, with a peak temperature of 110 K.[13] In their reactions upon a surface held at 10K, Qasim *et al.* noted the desorption of propene at a peak temperature of 86 K.[6] The desorption temperature noted by Qasim *et al*. is likely to be more accurate than that noted by Dinger *et al.*, who conducted their experiments at a surface temperature of 90 K and even noted that owing to this high deposition temperature, the vast majority of the propene product had likely desorbed. [6,13]

As mentioned in previous Chapters, oxygen is the third most abundant element in the ISM.[1] However, the abundance of oxygen observed in the gas phase in the ISM is lower than what is expected. The depletion of oxygen from the gas phase can be explained if oxygen condenses out onto the surfaces of the dust grains in the dark cores of the ISM and through the reaction of oxygen with other adsorbed species and the consequent incorporation of oxygen atom into other grain-bound molecules.[1,2] The reaction of propene and atomic oxygen on graphite has previously been investigated within our group and the thermal reaction on a surface was found to proceed with a lower reaction barrier than observed for the reaction between atomic oxygen and propene in the gas phase.[2] Additionally, the desorption energy of propene from graphite was modelled and found to be 21.45 ± 0.03 kJ mol^{-1}.[2] The main product of the reaction was found to be C_3H_6O, although the exact structure of the molecule could not be determined due to the large number of potential isomers. Based upon similar experiments between oxygen and ethene, Ward and Price tentatively assigned this product to be propylene oxide.[2] At the time of publishing this earlier work, propylene oxide had not yet been detected within the ISM but has since been detected in the Sagittarius B2 star-forming region, making it one of the few chiral molecules to be detected in the ISM. [14,15] In this chapter, the preliminary findings for the reaction of propene with atomic oxygen on a hybrid amorphous carbonaceous surface will be discussed.

7.3: Experimental

The experiments discussed in this Chapter were carried out using the Cosmic Dust apparatus as detailed in Chapter 2. Propene (99% purity) was plumbed into the source chamber and dosed, in separate experiments, onto graphite (2.08 x 10^{-3} ML s^{-1}) and a hybrid amorphous carbonaceous surface (HACS) (4.06 x 10^{-4} ML s^{-1}). Further experimentation was conducted on the HACS, where propene and atomic oxygen were co-dosed to investigate their reactivity on this novel surface. The atomic oxygen (0.44 x 10^{-3} ML s^{-1}) was generated by passing molecular oxygen through the microwave discharge cell, as outlined in Chapter 2. The dissociation efficiency was approximately 10%, meaning that molecular oxygen (3.98 x 10^{-3} ML s^{-1}) was also dosed onto the surface along with the atomic oxygen, as discussed in Chapter 4.

As mentioned in Chapter 6, conventional laboratory analogues for interstellar dust grains are unlikely to be accurate representations of the actual grains in the ISM. For example, graphite is commonly used to represent the carbonaceous dust grains, however it is unlikely that the

interstellar grains will have such ordered structures. As such, the desorption from a new hybrid amorphous carbonaceous surface (HACS) was investigated. The HACS is a diamond-like coating (DLC) deposited on a Cu (111) surface. It is a hybrid Dymon-iC™ coating that was manufactured by Teer Coatings using a closed field unbalanced magnetron sputter ion plating system with plasma enhanced CVD using a hydrocarbon gas precursor.[16] The coating consists of a 1 micron thick amorphous carbon layer on top of a thin chromium adhesion layer deposited onto the copper surface. Analysis of the carbonaceous layer shows that the layer is amorphous, metal free and hydrogenated, with a significant proportion of sp^3 bonding.[16] Both the graphite and the HACS substrates are pictured in Figure 7.1.

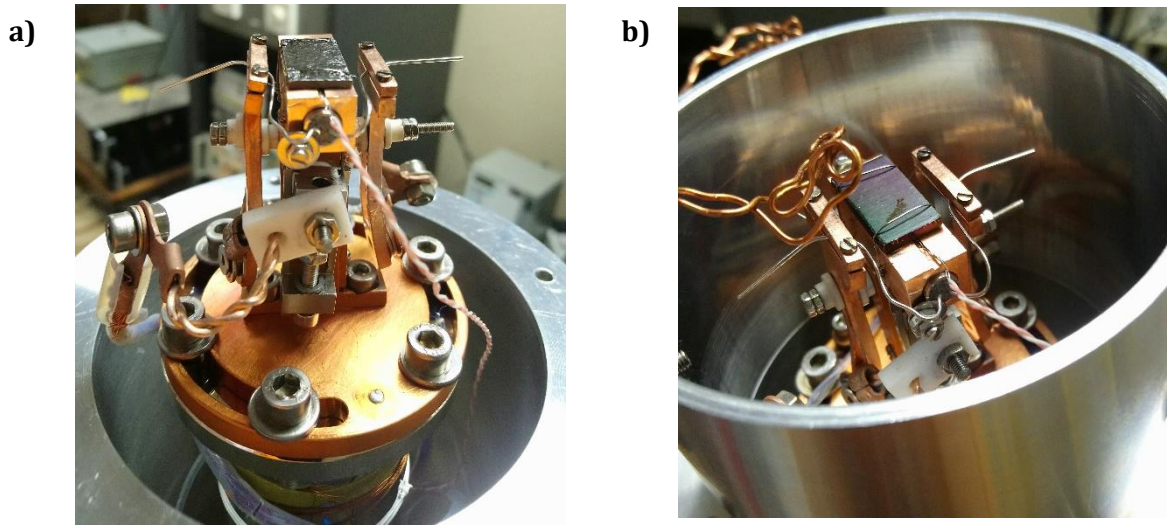

Figure 7.1: a) Image of the mounted graphitic surface, b) image of the mounted hybrid amorphous carbonaceous surface.

7.4: Results and discussion

In the following section the desorption characteristics of propene from a graphitic surface and the HACS will be compared. Additionally, the reaction between oxygen atoms and propene on the HACS will be investigated.

7.4.1: Desorption Characteristics of Propene from Graphite and the HACS

The TPD spectra for the desorption of propene from graphite are shown in Figures 7.2 & 7.3. Propene was dosed onto the surface for various lengths of time ranging from 2 minutes to 1 hour (0.25 ML – 7.50 ML). The temperature of the surface was held constant at 20 K during deposition. During the course of the TPD experiments, the surface was linearly heated causing the desorption

of the propene. The ions of mass 42, corresponding to the molecular ion peak of propene, were monitored throughout the experiments.

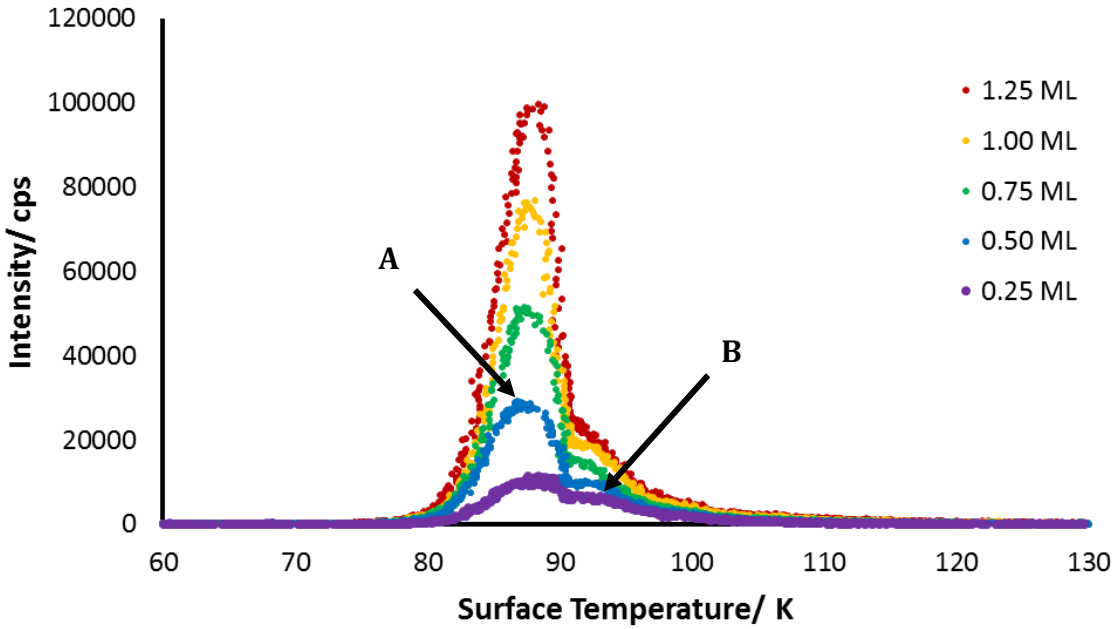

Figure 7.2: Desorption spectra of propene from the HOPG surface. The profiles of different doses, increasing from 2 mins to 10 mins (0.25 ML – 1.25 ML), are shown.

At the lowest dose for propene, a single peak is observed at 87 K (Peak A). This peak has a higher temperature shoulder at 91 K (Peak B). As the dose is increased both Peak A and Peak B increase, while the peak temperature remains constant. After an 8 minute dose (1ML), Peak A will shift to higher temperatures, while Peak B also increases in intensity but the peak temperature remains constant. Peak B dose not increase to the same extent as Peak A, but nor does it saturate. As can be seen from Figure 7.3, continued exposure of the surface to propene causes rapid growth of Peak B. At these longer exposures (30 minutes, 45 minutes and 60 minutes), Peak B will continue to increase in intensity and shift towards higher temperatures, while the growth of Peak A is stunted.

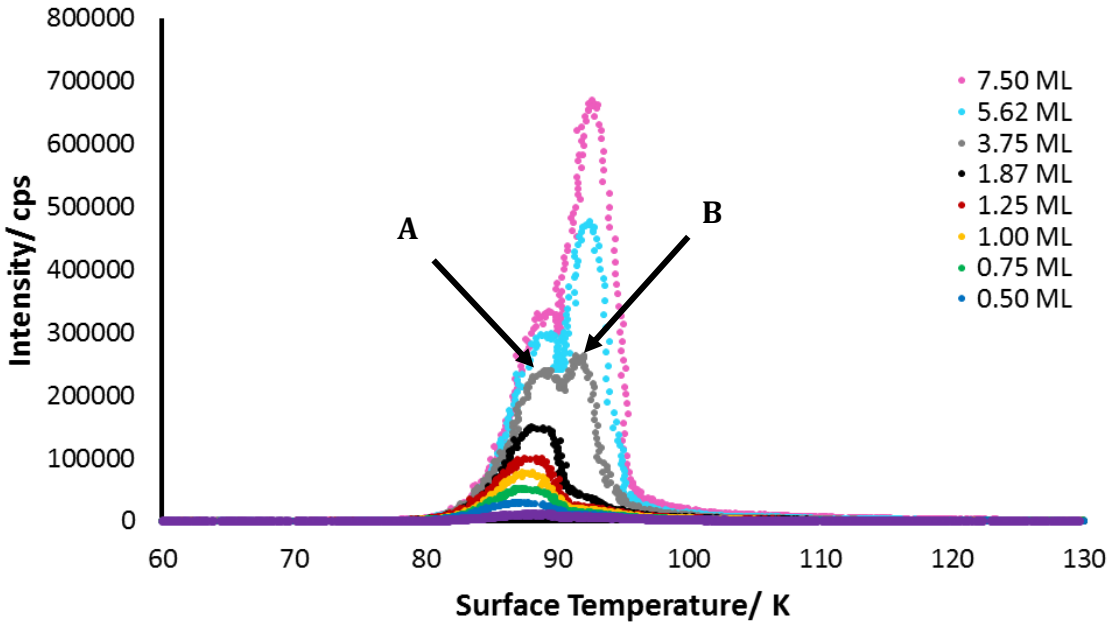

Figure 7.3: Desorption spectra of propene from the HOPG surface. The profiles of different doses, increasing from 2 mins to 60 mins (0.25 ML and 7.50 ML respectively), are shown. Peak B at 91 K increases dramatically with higher doses.

The initial peak at 87 K can be assigned to monolayer desorption of propene from graphite. This is in good agreement with the peak temperature noted by Qasim *et al.,* who observed that propene desorption occurred at 86 K. It is however, marginally lower than the peak observed for propene desorption from a carbonaceous surface by Dinger *et al.*, who stated that propene ices desorb at 110 K.[13] However, as noted in their study, their experiments are taking place at dosing temperatures of 90 K, so it is highly likely that the vast majority of the propene product had desorbed before detection. [13] With increasing exposure, peak A eventually saturates meaning the coverage of the first monolayer is complete and multilayer ices begin to grow, causing the peak to shift to higher temperatures. The multilayer nature of the desorbing ices is further confirmed as the peak cannot be saturated. Owing to the behaviour observed in both Figures 7.2 & 7.3, the high temperature shoulder is assigned to crystalline propene ice. The growth of both amorphous and crystalline ices simultaneously on the surface is not unheard of, as previously observed by Edridge *et al.* who noted the desorption order of low exposures of multilayer carbon dioxide ices was not zero order as expected, which they believed was likely caused by the transition of some of the ice from amorphous to crystalline.[17] There are repulsive interactions between the propene molecules in the ice, therefore a rearrangement can take place to better accommodate them.[7] The low intensity of Peak B during the initial doses may be because only small amounts of crystalline ice are produced, caused by rearrangement of the amorphous ice during the heating period of the TPD.[17] It is likely that crystalline propene ice preferentially forms on the surface at temperatures

over 90 K, hence accounting for the sudden increase in intensity of Peak B and the stunted growth of Peak A at longer exposures. Furthermore, at lower doses, the width of the peaks A and B stay the same, however the broadness of the peak increases with increasing dose above 90 K, suggesting the sudden desorption of a great deal more ice than observed lower doses.

Through analysis of the spectra in Figures 7.2 & 7.3, as described in Chapter 2, the desorption energy of propene from graphite was calculated. The value for the desorption energy was 20.58 ± 0.72 kJ mol^{-1}, which is in good agreement with the value obtained by Ward and Price (21.45 ± 0.03 kJ mol^{-1}).[2]

The desorption of propene from the HACS was also investigated. Analysis of the desorption spectra showed very similar desorption characteristics to the desorption of propene from graphite. The TPD profile for low doses of propene from graphite and from the HACS are compared in Figure 7.4, however due the difference in the flux of propene to the surfaces, the data for desorption from the HACS has been increased by a factor of 5 for comparison.

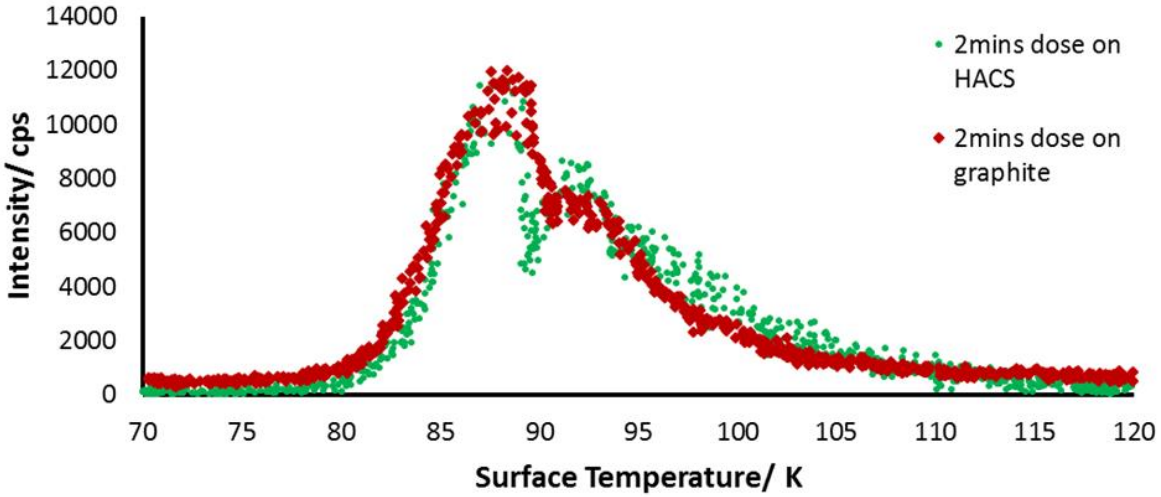

Figure 7.4: Desorption spectra of propene from the HOPG surface (red) and from the HACS (green) (x5). As can be seen from the data, the desorption profiles of propene from both surfaces are very similar.

7.4.2 The Reaction of Propene with Atomic Oxygen on the HACS

Owing to time constraints, only preliminary investigations were conducted on the hybrid amorphous carbonaceous surface. Propene and the atomic/molecular oxygen mix were co-dosed

onto the HACS at 20 K for 30 minutes. Additionally, a control experiment was also conducted, where propene and pure molecular oxygen were co-dosed onto the surface at the same temperature and same length of time. As there were no experiments conducted on this surface previously, it was unclear what the products of the reaction would be. As a result, for the first experiment, the full mass spectrum was scanned multiple times as the surface was heated. This allowed for the identification of possible product peaks and indicated which masses should be selectively observed when the experiment was repeated. Analysis of the intensity of the signals in the full spectrum mass spectra for the reaction between atomic oxygen and propene indicated that peaks could be observed at *m/z* 15, 26, 27, 28, 29, 30, 43, 44, 58, 75, 90. As with the reaction between atomic oxygen and acrolein discussed in Chapter 4, the co-dosing of atomic and molecular oxygen also leads to the formation of ozone on the surface of this dust grain analogue. In order to get a better understanding of the organic products formed, the peaks at *m/z* 16, 32, 48 and 42 (assigned to molecular oxygen, ozone and unreacted propene) will not be discussed further in this Chapter.

The desorption spectra for some of the *m/z* values listed above can be seen in Figures 7.5 & 7.6. The spectra for the dosing of propene with molecular oxygen (no O atoms) have also been included for reference. In Figure 7.5a and Figure 7.5c, a double peak at 88 K and 92 K is observed for both reactions. This peak corresponds to the mass 15 fragment ion and mass 43 ion of unreacted propene, arising from CH_3^+ ions and from the isotope ions of $C_3H_6^+$. Fragment peaks for propene were also observed at m/z 26, 27 and 28 (not shown).

Another fragment ion double peak is observed for m/z 15 at 149 K and 162 K (Figure 7.5a). These can also be seen at m/z 29, 43, 44, 75 and 90 (Figure 7.5 (b-c) & Figure 7.6 (a-c)). The detection of the peaks at m/z 90 is particularly interesting. Ward and Price previously conducted a similar study into the reaction between atomic oxygen and propene on a graphite surface. [2] In their investigation they found the main product of the reaction between propene and atomic oxygen to be a molecule with the general formula C_3H_6O. The exact structure of the product could not be assigned due to the large number of structural isomers, however it was thought to be propylene oxide.[2] Propylene oxide and its structural isomers are m/z 58. In the studies conducted on the HACS described here, there was only a small, low intensity, broad peak visible at mass 58 between 120 -180 K (not shown). Instead, the molecular ion peak for the chemical product appears to be at mass 90, corresponding to an ion with the general formula $C_3H_6O_3$. The presence of a peak with this mass, suggests that the ozone that is formed on the surface from the reaction of atomic oxygen and molecular oxygen (see Chapter 4 for more details) has added across the double bond instead of a single oxygen addition, as previously observed by Ward and Price.[2] The discrepancy between the results obtained by Ward and Price and the results obtained in this study could be due to the

change in the substrate, from graphite to HACS. As will be discussed later, the detection of CO_2 suggests that the oxygen atoms etch the HACS, while no etching is observed for the dosing of O atoms onto a graphite surface, suggesting that while the desorption characteristics are similar, the interaction of the adsorbates with this new amorphous surface and with graphite may be slightly different. Additionally, there have been several changes to the experimental setup, as discussed in Chapter 2. Ward and Price used the same apparatus in their experiments but as mentioned earlier, the heating unit has since been replaced, where the tantalum strip heater has been upgraded to a cartridge heater. Furthermore, when Ward and Price conducted their experiments, the surface was not heated linearly, instead the surface was warmed to approximately 200 K by applying a constant current to the tantalum strip heater. It is possible that heating via this method did not allow the adsorbed species to rearrange in the same way as they were able to during the linear heating carried out in the experiments outlined in this chapter. Moreover, with the previous experimental setup, the desorbing species were ionised before entering a TOFMS with either a pulsed electron gun (29kHz, 400 eV) or with a wavelength selected laser beam. As discussed in Chapter 3, the experiments highlighted in this thesis now use a QMS to ionise and analyse the desorbates. As previously mentioned, the results presented in this Chapter are just preliminary, and further work is needed in order to ascertain the exact reason why a different product was observed in these reactions than was previously observed by Ward and Price. In particular, the experiments should be repeated on graphite with the current experimental setup to allow for the direct comparison between the experimental results with those obtained by Ward and Price, ruling out any differences caused by change of substrate.

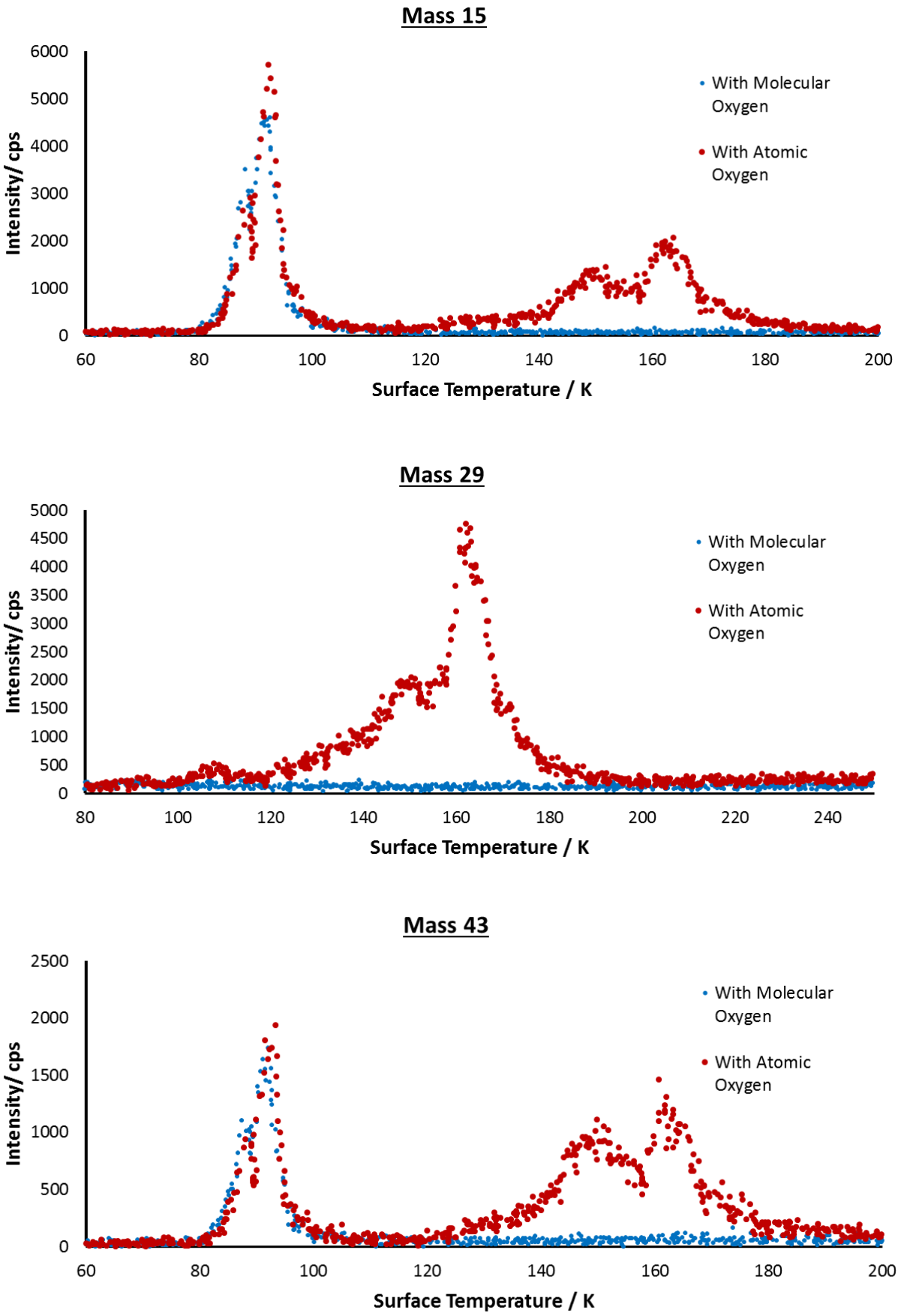

Figure 7.5: Desorption spectra showing the product peaks for the reaction between propene and atomic oxygen. The product peaks at m/z (a) 15, (b) 29 and (c) 43 are shown in red. The product peaks for the reaction between molecular oxygen and propene are also shown in blue.

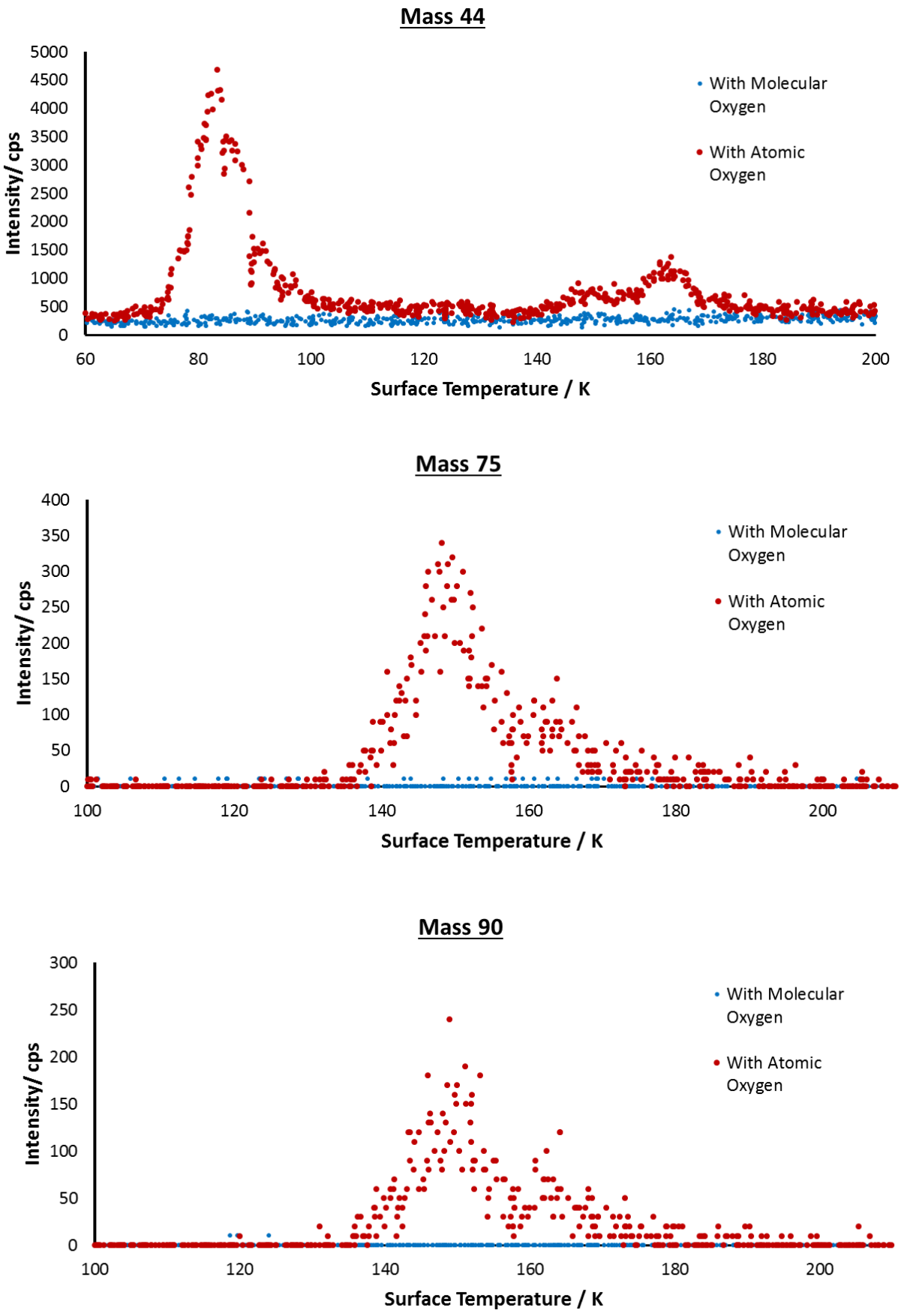

Figure 7.6: Desorption spectra showing the product peaks for the reaction between propene and atomic oxygen. The product peaks at m/z (a) 44, (b) 75 and (c) 90 are shown in red. The product peaks for the reaction between molecular oxygen and propene are also shown in blue.

The reaction between ozone and propene is a well-known process that takes place in the gas phase and in solution. The reaction proceeds via the Criegee mechanism (Figure 7.7) and in most cases leads to the production of aldehydes and ketones.[18–20]

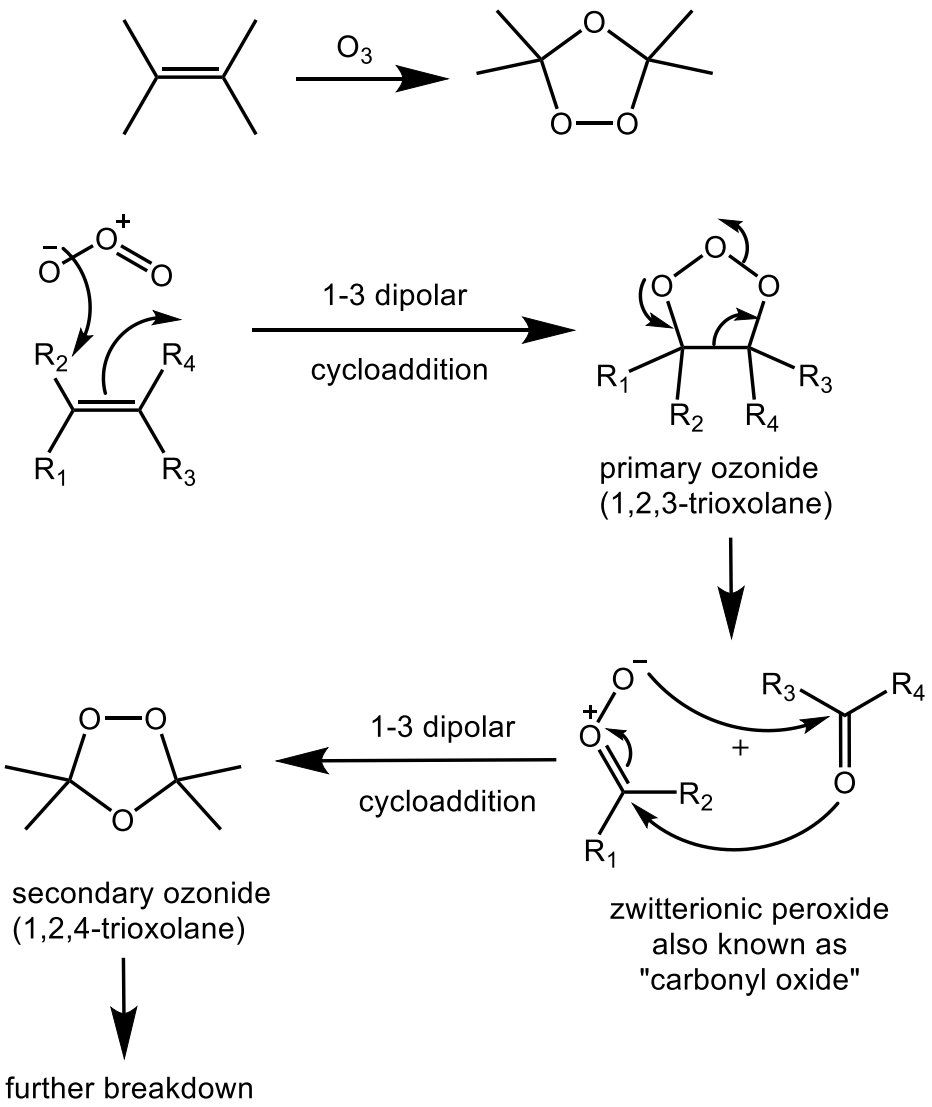

Figure 7.7: Schematic showing the ozonolysis of an alkene via the Criegee mechanism. The final secondary ozonide is quickly broken down into various other oxygen-containing organic molecules.

Based on the ion peak observed at *m/z* 90 (Figure 7.6 c) and the fragment ions observed at *m/z* 75, 44, 43, 30 (not shown), 29 and 15 we can assume that a similar mechanism must be taking place upon the HACS. As mentioned previously in Chapter 4, the reaction between atomic oxygen and molecular oxygen to form ozone is a barrierless reaction that will proceed in direct competition with the reaction between propene and O atoms.[1] According to the mechanism described in Figure 7.7, these ozone molecules can add across the double bond in the alkene to form an ozonide.[20] The ozonide is unstable, due to ring strain and so breaks down into a

zwitterionic peroxide and a carbonyl, which in turn can react together to form the secondary ozonide, the structure of which is similarly strained. Herron *et al.* investigated the ozonolysis of propene in the gas phase and detected the presence of CH_2O, CH_3CHO, HCOOH, CH_3COOH, CH_3OH, CO_2, H_2O and CO.[19] With this in mind, some possible structures for the m/z 90 ion and its fragment ions are shown below (Figure 7.8).

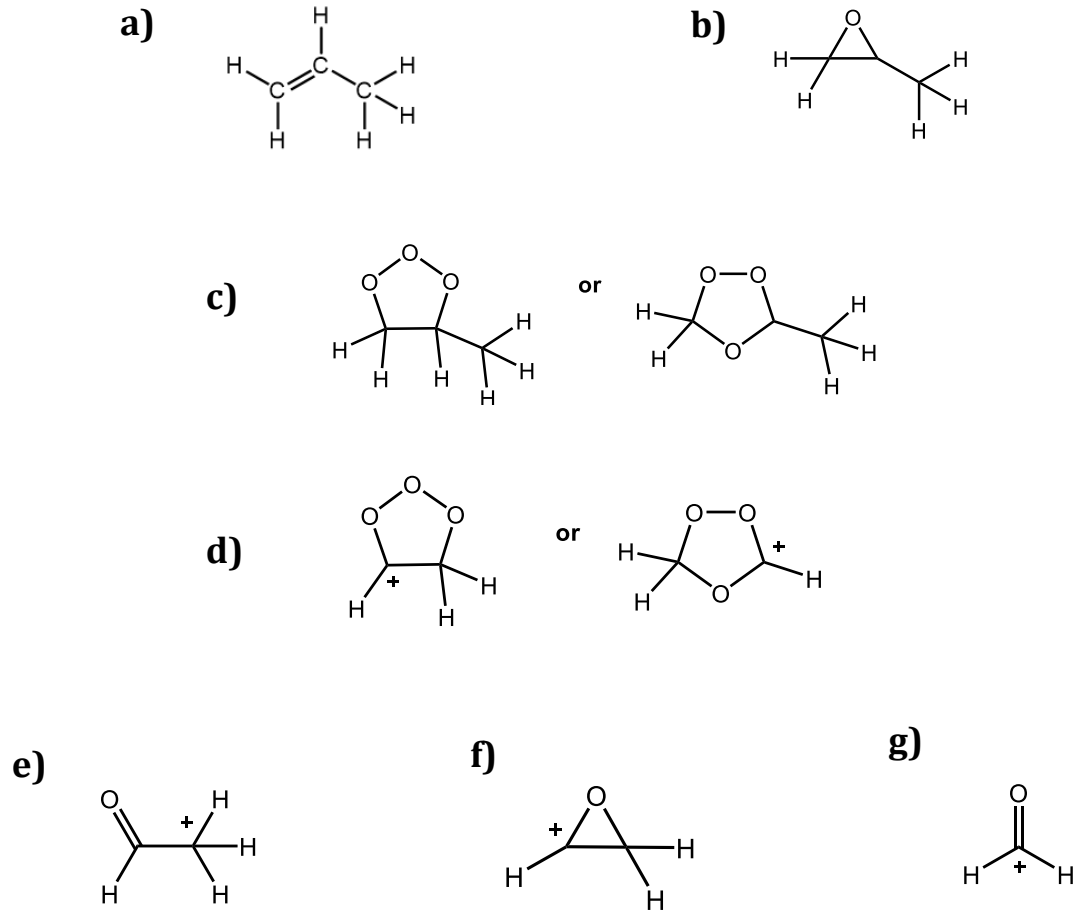

Figure 7.8: Schematic illustrating possible structures for the ions causing the peaks observed in the TPD profiles for the products of the reaction between atomic oxygen and propene, a) the structure of propene, b) the structure of propylene oxide, the supposed product from previous studies of the reaction, c) the new proposed product at m/z 90, d) a possible structure of the fragment ion at m/z 75, e) a possible structure of the fragment ion at m/z 44, f) a possible structure of the fragment ion at m/z 43 and g) a possible structure of the fragment ion at m/z 30.

Other peaks in the mass spectra can also be assigned. The peaks at 149 K and 162 K at *m/z* 29 in Figure 7.5b are likely caused by a COH fragment ion. Additionally, the peaks at 149 K and 162 K in Figure 7.6a, for *m/z* 44, can be assigned to CO_2 (the additional lower temperature peak at *m/z* 44 will be discussed in more detail below). The formation of various different oxygen containing COMs is of great importance to interstellar chemistry, because within the dense regions of the

interstellar medium, these molecules have longer lifetimes and react together to form even more complex species. The reaction between propene and ozone could provide a suitable route through which these complex molecules are formed.

Additionally, although a product fragment peak is observed for CO_2, another peak is observed at 83 K (Figure 7.6a). As can be seen in Figure 7.6a, the reaction between molecular oxygen and propene does not produce carbon dioxide as a product. Therefore, the presence of the CO_2 must be a direct result of the presence of the O atoms on the surface. This indicates that atomic oxygen reacts with the amorphous carbonaceous surface to produce CO_2, which is of vital interest in the ISM as CO_2 is an important interstellar molecule (as discussed in Chapter 5). The presence of carbon dioxide as a product of the reaction between O atoms and the substrate could indicate that the more amorphous surfaces provide a suitable pathway through which CO_2 is formed in the interstellar medium, and that the interstellar dust grains may be etched by O atom adsorbates.

7.5 Summary

In this chapter the desorption characteristics of propene from graphite were investigated. The desorption energy of propene from graphite was calculated to be 20.58 ± 0.72 kJ mol^{-1}, in good agreement with the value modelled by Ward and Price. [2] The desorption profile of propene from the graphitic surface was then compared to the desorption profile of propene from the hybrid amorphous carbonaceous surface and found to be the same.

The reaction of propene and atomic oxygen on the hybrid amorphous carbonaceous surface was also investigated. The preliminary results indicate that the ozone, formed from the side reaction of atomic oxygen and molecular oxygen, will react with the propene to form a product with m/z 90 which we can assign to $C_3H_6O_3$. The breakdown of this product may proceed through the Criegee mechanism as observed for the ozonolysis of propene on Earth. Ozonolysis reactions with alkenes in the ISM could help to account for the variety of molecules observed in the cold, dark clouds of the ISM.

Furthermore, CO_2 desorption was also observed when O atoms were dosed onto the amorphous carbonaceous surface but have not been observed with dosing of O atoms on graphite. This indicates that the reaction of O atoms with amorphous surfaces in the ISM could be a viable pathway for the production of CO_2. The production of CO_2 indicates that amorphous dust grains, with structures similar to the HACS, many be etched by adsorption of oxygen atoms.

7.6 References

1 H. J. Kimber, C. P. Ennis and S. D. Price, *Faraday Discuss.*, 2014, **168**, 167–184.

2 M. D. Ward and S. D. Price, *Astrophys. J.*, 2011, **741**, 121.

3 H. Linnartz, S. Ioppolo and G. Fedoseev, *Int. Rev. Phys. Chem.*, 2015, **34**, 205–237.

4 N. Marcelino, J. Cernicharo, M. Agúndez, E. Roueff, M. Gerin, J. Martin-Pintado, R. Mauersberger and C. Thum, *Astrophys. J.*, 2007, **665**, L127–L130.

5 K. M. Hickson, V. Wakelam and J. C. Loison, *Mol. Astrophys.*, 2016, **3–4**, 1–9.

6 D. Qasim, G. Fedoseev, T. Lamberts, K. J. Chuang, J. He, S. Ioppolo, J. Kästner and H. Linnartz, *ACS Earth Sp. Chem.*, 2019, **3**, 986–999.

7 W. X. Huang and J. M. White, *Surf. Sci.*, 2002, **513**, 399–404.

8 R. Kleyna, D. Borgmann and G. Wedler, *Surf. Sci.*, 1998, **402–404**, 131–134.

9 R. Kleyna, D. Borgmann and G. Wedler, *Surf. Sci.*, 1999, **433**, 205–209.

10 R. Kleyna, S. Fickert, D. Borgmann and G. Wedler, *Langmuir*, 1998, **14**, 5464–5468.

11 H. M. Ajo, V. A. Bondzie and C. T. Campbell, *Catal. Letters*, 2002, **78**, 359–368.

12 K. H. Schulz and D. F. Cox, *Surf. Sci.*, 1992, **262**, 318–334.

13 A. Dinger, C. Lutterloh, J. Biener and J. Küppers, *Surf. Sci.*, 1999, **421**, 44–52.

14 Y. Ellinger, F. Pauzat, A. Markovits, A. Allaire and J.-C. Guillemin, *Astron. Astrophys.*, 2020, **633**, A49.

15 B. A. McGuire, P. Brandon Carroll, R. A. Loomis, I. A. Finneran, P. R. Jewell, A. J. Remijan and G. A. Blake, *Science (80-.).*, 2016, **352**, 1449–1452.

16 S. K. Field, M. Jarratt and D. G. Teer, *Tribol. Int.*, 2004, **37**, 949–956.

17 J. L. Edridge, K. Freimann, D. J. Burke and W. A. Brown, *Philos. Trans. R. Soc. A Math. Phys. Eng. Sci.*, 2013, **371**, 20110578–20110578.

18 B. Qi, B. Yang, Z. Wang, H. Yang and L. Liu, *Sci. China, Ser. B Chem.*, 2009, **52**, 356–361.

19 J. T. Herron and R. E. Huie, *Int. J. Chem. Kinet.*, 1978, **10**, 1019–1041.

20 J. J. Li, *Name Reactions: A Collection of Detailed Reaction Mechanisms*, Springer-Velag Berlin Heidelberg, Germany, 2003..

Chapter 8: Conclusion and Further Work

8.1 Conclusion

In this thesis the interactions and reactions of small molecules on astrochemically relevant surfaces were investigated.

8.1.1 Desorption of Small Molecules from Graphite

Studies into the desorption characteristics of small molecules were conducted using the Cosmic Dust apparatus. Various doses of methanol were dosed onto the graphitic surface at 18 K and the desorption profiles were recorded. Through analysis of the TPD spectra using the Polanyi Wigner equation, the desorption energy of multilayer ices of methanol was found to be 42.7 ± 1.1 kJ mol^{-1}. This is in relatively good agreement with the values obtained in previous studies (31 - 40 kJ mol^{-1}).[1] Similarly, the desorption characteristics and energies of ammonia (25.13 ± 0.59 kJ mol^{-1}) and carbon dioxide (21.6 kJ mol^{-1}) were found the be in good agreement with the literature values.[2–4] The agreement between our results and the values observed in previous studies, highlights that the experimental techniques and analytical methods we employ during our investigations are valid for modelling the desorption behaviour and reactions of small molecules under interstellar conditions.

8.1.2 The Reaction of Small molecules with Atomic Oxygen on Astrochemically Relevant Surfaces

The reaction of atomic oxygen with an unsaturated organic molecule was investigated on two different surfaces. The first reaction involved the interaction between acrolein and atomic oxygen on graphite, which is the standard carbonaceous dust grain analogue used in laboratory experiments. Atomic oxygen was generated by passing molecular oxygen through a microwave discharge cell, as described in detail in Chapter 2. As the dissociation efficiency of molecular oxygen into atomic oxygen was calculated to be approximately 10%, any dosing of atomic oxygen also involved the dosing of molecular oxygen onto the surface of the cold substrate. The reaction between acrolein and oxygen atoms was shown to have a temperature dependence, only occurring at temperatures above 40 K. This was due to the dominance of the side reaction between atomic and molecular oxygen on the surface at lower temperatures, forming ozone. At higher temperatures the molecular oxygen had desorbed from the surface, allowing for the interaction between atomic oxygen and acrolein. For this reaction, a product with *m/z* 72 was observed and assigned to the single addition of oxygen across the double bond of the acrolein forming $C_3H_4O_2$. The exact structure of the product could not be elucidated due to the large

number of possible isomers. The reaction between atomic oxygen and acrolein on graphite was then modelled using a simple kinetic model. The experimental yield of the products was compared to the modelled data. Good agreement was observed for the yield of ozone, the product of the O + O_2 side reaction, while relatively good agreement was achieved for the yield of $C_3H_4O_2$. The yield of the organic product was slightly lower than the yield observed experimentally, but this is believed to be due to overestimation of the absolute yield. Modelling of the surface reactions indicated that the low temperature formation of ozone was largely proceeding through an ER mechanism. Low surface temperatures hinder the diffusion of O atoms across the surface so the LH mechanism cannot take place. As the temperature increases, the O atoms gain enough energy to overcome the diffusion barrier and reactions can proceed through LH mechanisms. Concurrently, the O atom addition reaction to acrolein proceeds via processes, until temperatures of approximately 60 K, at which point O atoms will no longer adsorb to the surface for residence times that allow for diffusion to occur. From this point the addition reaction proceeds solely through the ER mechanism. This highlights the mechanisms through which reactions would occur in the interstellar medium as well as providing insight into the temperature dependence of surface reaction mechanisms.

As the structure of the interstellar dust grains are unlikely to be as ordered as graphite, an amorphous carbonaceous surface was introduced into the Cosmic Dust apparatus. The amorphous surface is largely composed of sp^3 hybridised carbon showing no long-range order. The second reaction of atomic oxygen with an unsaturated organic molecule was conducted on this surface. In particular, the reaction between atomic oxygen and propene was investigated. This reaction was chosen because the oxidation of propene with atomic oxygen had previously been studied using the Cosmic Dust apparatus, allowing the easy comparison between the surface chemistry observed on the new surface versus the chemistry on graphite.[5] Prior to the co-dosing experiments, the desorption profile of propene from the amorphous surface was recorded and observed to be similar to the profile for the desorption of propene from graphite. The desorption energy of propene from the amorphous surface was calculated (20.58 ± 0.72 kJ mol^{-1}) and found to agree with the desorption energy previously determined by Ward and Price from a graphitic surface (21.45 ± 0.03 kJ mol^{-1}).[5] According to the studies by Ward and Price, the product of the reaction between atomic oxygen with propene is single addition product , C_3H_6O. However, this product was not observed for the reaction carried out on the amorphous surface. Instead a product with *m/z* 90 was observed, corresponding to the addition of ozone across the double bond of propene, $C_3H_6O_3$. The interaction between ozone and propene was confirmed by repeating the experiment at temperatures of 50 K, where all molecular oxygen had desorbed. With no molecular oxygen, at high temperatures there is no formation of ozone. Similarly, the

signal at *m/z* 90 was no longer observed. The product of the ozonolysis of propene is known to undergo a rearrangement in the gas and solution phase. The ozonide formed from this rearrangement is inherently unstable and quickly breaks down into smaller molecules such as aldehydes, ketone, carboxylic acids, carbon dioxide and alcohols. It is possible that the reaction on the amorphous surface proceeds the same way, and as such the ozonolysis of propene and the subsequent breakdown of the final product could help account for the depletion of oxygen (as it is incorporated into organic species) as well as the rich variety of species observed in interstellar space. Furthermore, CO_2 production was noted when oxygen atoms were dosed onto the surface. This suggests that this type of amorphous surface is etched by the O atoms. Surfaces of similar structures within the ISM could also be subject to this destructive etching.

8.1.3 Desorption of Small Molecules from Amorphous Fullerene-like Surfaces

In addition to the amorphous surface discussed above, another amorphous carbonaceous surface was manufactured in collaboration with Dr Cornelia Jäger in Jena. The surfaces are composed of amorphous carbon arranged in broken fullerene-like cages. The cage structures are held together by Van der Waals forces or by aliphatic linkers. The desorption characteristics of acrolein and oxygen from one of the amorphous surfaces were examined in detail. The TPD profile showed areas similar to the desorption of the molecules from graphite, however an additional desorption feature was observed at high temperatures. This high temperature feature was a broad peak, consistent with the observations of the desorption of molecules from a Single Walled Carbon Nanotube (SWCNT), as reviewed by Ulbricht et al.[3] The broad feature at higher temperatures is assigned to desorption of the molecules from higher energy binding sites on the porous amorphous carbonaceous surface. These higher energy sites are not available on graphite. Owing to the presence of the higher energy binding sites, acrolein, oxygen and carbon dioxide were observed to remain on the surface of these amorphous grain analogues until temperatures much higher than those previously observed for desorption from graphite. Therefore, it may be necessary for astronomers who are studying areas where dust grains with similar structures can form, to adjust their models to account for the enhanced binding of the molecules to the surface.

8.2 Further work

The studies presented in this thesis show a fraction of the chemistry that could be taking place in the interstellar medium. Through further experiments under astrochemically relevant conditions, it is possible to gain a better understanding of these reactions, especially with regards to the chemistry taking place on the surface of the interstellar dust grains.

A particularly interesting observation from the experiments examined in this thesis, is the different desorption characteristics observed for various small molecules from the fullerene-like amorphous surfaces. Examination of the enhanced binding characteristics can be extended to include other molecules, for example methanol, ammonia and water. Water would be particularly interesting because it did not show enhanced binding to the surface of the SWCNTs studied by Ulbricht et al.[3] Additionally, the reaction between small molecules and atomic oxygen or atomic hydrogen could be conducted and modelled on these surfaces, in order to examine the extent to which the higher energy binding sights effect the yield of product as well as the surface mechanisms occurring. Other amorphous carbonaceous surfaces were also made at Jena. These surfaces were also manufactured by laser ablation of ^{13}C, although in quenching gases containing more hydrogen than was used for the manufacturing of the ACSs. SEM images of these additional surfaces showed the structure of the grain analogue was more aliphatic than the ACS structure, and no fullerene cages were observed. A more comprehensive study comparing the desorption characteristics of various astrochemically relevant molecules from graphite, the ACSs and the aliphatic amorphous surfaces could be conducted.

The reaction of propene and atomic oxygen on the HACS made by Teer Coatings could also be investigated further, as only preliminary results are reported in this thesis. Initially, the reaction should be repeated on graphite to confirm whether or not the product at m/z 90 is detected. This will clarify whether or not the formation of the ozonide is exclusive to the amorphous carbonaceous surface. Additionally, the kinetic model could be updated to model this reaction so some insight into the surface mechanisms can be gleaned. Furthermore, as mentioned, the HACS is a new hybrid surface specifically manufactured for our experiments. Therefore, further characterisation of the surface needs to be undertaken in order to gain more information about the actual structure of the amorphous substrate. In particular, IR spectra, SEM and HRTEM imaging of the surface would help to clarify the structure and enable a more concrete comparison between the HACS and graphite as well as the new ACSs discussed.

The reaction of acrolein with atomic oxygen was also investigated in this thesis. This is of particular interest because of the significance of acrolein as a prebiotic molecule. As mentioned,

acrolein is formed during the decomposition of sugars and is involved in the synthesis of amino acids, which are the building blocks of life. Therefore, knowledge of its reactivity within the interstellar medium may provide insight into the origins of life here on Earth. As a result of this, it would be interesting to carry out further experiments involving acrolein. In particular, investigations could be conducted into the reaction of acrolein with nitrogen atoms, or with both nitrogen and oxygen atoms. These reactions could result in the generation of more complex organic molecules, which could be precursors to some amino acids. Prior to the undertaking of these experiments, however, adjustments would need to be made to the microwave discharge source to allow for the efficient dissociation of molecular nitrogen into atomic nitrogen. The current dissociation efficiency of molecular oxygen is approximately 10%, meaning a large amount of molecular oxygen is co-dosed with the atomic oxygen, leading to the generation of ozone at low surface temperatures. As molecular nitrogen contains a triple bond as opposed to the double bond in O_2, one would expect the dissociation efficiency of molecular nitrogen to be lower than that of oxygen. Therefore, molecular and atomic nitrogen would also be co-dosed during any experiment, which could result in a number of side reactions, thereby making the kinetics of the possible reaction between nitrogen and acrolein difficult to extract.

8.3 Summary

In this chapter, the main conclusions for the experiments reported in this thesis were drawn together and summarised. The next steps that could be taken experimentally were also outlined. In particular, desorption of small molecules from amorphous surfaces as opposed to the standard dust grain analogue, graphite, have shown interesting results and a more comprehensive study into the interactions and reactions of adsorbates on these surfaces could provide interesting information about how molecules interact with more amorphous dust grains in the ISM. This could eventually improve the accuracy of interstellar models, which have in the past, only included data derived from experiments on graphitic surfaces.

8.4 References

1 A. S. Bolina, A. J. Wolff and W. A. Brown, *J. Chem. Phys.*, 2005, **122**, 4

2 A. S. Bolina and W. A. Brown, *Surf. Sci.*, 2005, **598**, 45–56.

3 H. Ulbricht, R. Zacharia, N. Cindir and T. Hertel, *Carbon N. Y.*, 2006, **44**, 2931–2942.

4 J. L. Edridge, K. Freimann, D. J. Burke and W. A. Brown, *Philos. Trans. R. Soc. A Math. Phys. Eng. Sci.*, 2013, **371**, 20110578–20110578.

5 M. D. Ward and S. D. Price, *Astrophys. J.,* 2011, **741**, 121.